---

# Master Thesis

## *Optimization of Integrated Capacitive Displacement Sensors for Contractility Assays in an Engineered Heart Tissue Platform*

---

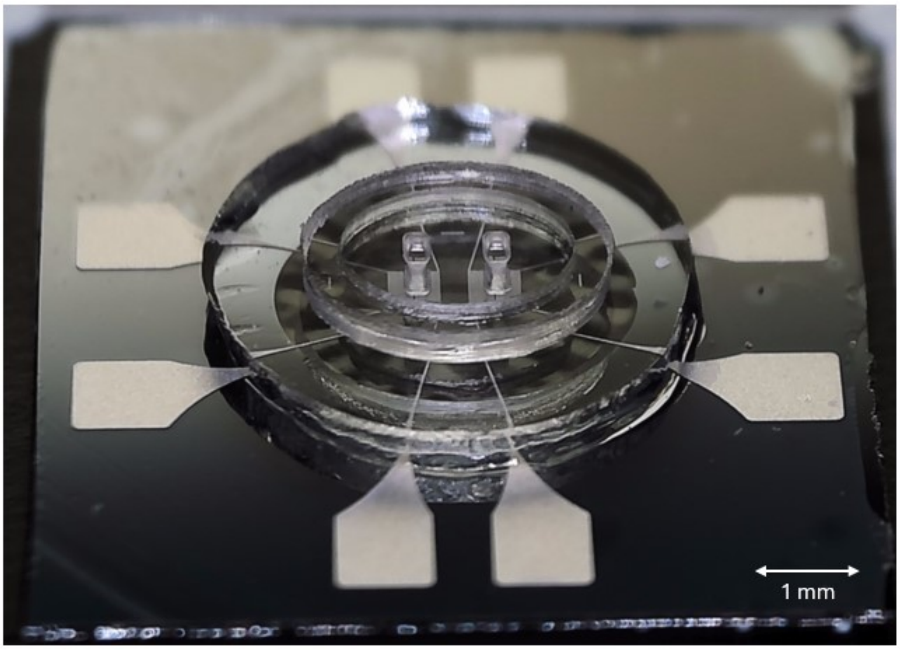

Thomas Bouman
MSc Biomedical Engineering

DELFT UNIVERSITY OF TECHNOLOGY

SECTION OF ELECTRONIC COMPONENTS,
TECHNOLOGY & MATERIALS,

DEPARTMENT OF MICROELECTRONICS

December 1, 2024

# Abstract

Heart diseases are the leading cause of death worldwide, which is why heart diseases have become an important focus for the development of new effective treatments [1]. However, the current drug development pipeline is fraught with inefficiencies, ethical concerns, and financial burdens, largely due to the reliance on animal models and static cell cultures that fail to accurately predict human physiological responses [2]. Building on previous work from Dr. Dostanic [3], this master's thesis advances the development of a novel Engineered Heart Tissue (EHT) platform, which holds promise as a more accurate and ethical research model for studying biological processes, drug discovery, and heart disease mechanisms. The EHT platform is a small PDMS-based construction and consists of two micropillars surrounded by an elliptic well. It also features co-planar capacitive displacement sensors, specifically designed to measure the contraction force of EHTs.

This master thesis work focuses on optimizing sensor sensitivity and enhancing platform rigidity to prevent sensor damage during assembly of the platform. Using COMSOL Multiphysics simulations, ideal sensor geometries and substrate configurations were identified, leading to the design and fabrication of multiple sensor prototypes. The sensors were fabricated using microfabrication techniques and electrically characterized under static and dynamic conditions. While static capacitance measurements aligned with simulations, dynamic tests revealed discrepancies between predicted and observed capacitance changes, indicating the need for further investigation into simulation accuracy and fabrication processes.

Despite these challenges, the sensors showed promise by successfully measuring platform displacement in response to applied forces. However, the platform's sensitivity must be improved in order to detect EHT contraction.

With continued advancements, this platform could contribute to the development of more precise and ethical research models, ultimately accelerating the development of new treatments and providing an alternative for the use of animals in research.

# Contents

# 1 Introduction

## 1.1 Background and motivation

Approximately 100 years ago, infectious diseases were the leading cause of death in western society [4]. Thanks to improvements in sanitation, public health (vaccination development and delivery), and medical treatments, such as antibiotics, the number of deaths from infectious diseases has declined dramatically. Nowadays, heart diseases such as myocardial infarction, hypertrophy, and atherosclerosis have become the new leading cause of death worldwide [1]. Unsurprisingly, heart diseases have become an important focus for the development of new treatments.

Regardless of the benefits that new treatments have on our quality of life, they come with complications that need to be taken in consideration. The development of new treatments has become a long and costly process. It is estimated that nearly 200 million animals are harmed and killed every year for scientific purposes [5]. In addition to the direct suffering that is involved, it takes about 10 years with an average cost of 1–2 billion dollar for each new drug to be approved for clinical use [6], making the search for new treatments a tremendous drain of lives, time and resources.

Figure 1.1: Rabbit in animal testing facility. Figure adopted from [7].

One of the main reasons that makes this process long and costly is the lack of good research models. About 90% of all drug candidates that pass pre-clinical testing still fail during phase I, II, III clinical trials and drug approval [2]. This means that even when a drug appears to be effective in the pre-clinical stage, where animal models and static cell cultures are often used, still 90% of the time the drug shows to be ineffective or toxic for the human body. This not only puts researchers on a dead end, but also misguides them along the way, resulting in large investments that bring more harm than good. It is therefore important to not only invest in the development of new treatments, but also in the development of more accurate, efficient and ethical research models. There is a need for models that can accurately represent the complexity of human physiology.

One of the recent developments in this field is Organ-on-Chip. Organ-on-chip technology combines advances in tissue engineering and microfabrication, which allows for the fabrication of 3D miniature tissues in 3D micro-environments, often with integrated microfluidic channels, sensors, and/or actuators. [8] The main goal is to mimic the small structural units and function of human organs in-vitro, enabling researchers to simulate biological processes and study the effects of drugs or model diseases in a controlled setting [9]. These research models have the potential to revolutionize drug discovery and improve our understanding of many diseases and biological processes. This will ultimately benefit patients with more effective treatments, while at the same time alleviating the exploitation of animals in research.

Organs-on-chips can be bundled into multi-organ-on-chip platforms, but most often they focus on mimicking one specific function of one organ at a time. For example, when the target organ is the heart, the purpose is to create a realistic in-vitro model the of human heart, and it is then called a heart-on-a-chip.

An Engineered Heart Tissue platform (EHT platform) is a specific type of heart-on-a-chip where cells are cultured to form 3D tissues between two anchoring points. These platforms are usually used for heart tissue contractility assays [10]. The development of an EHT platform is also the focus of this master thesis work. More specifically, this master thesis work focuses on the integration of capacitive displacement sensors into an EHT platform. But before the technical details will be further explained, we must first understand what an EHT platform exactly is, what it looks like, and how it works. This will be explained in the following section.

## 1.2 What is an EHT platform?

EHT platforms aim to recapitulate the physiology of the human heart. The level and aspect of recapitulation depend on the specific targeted application. One of these applications is the investigation physiological processes, for instance, observing how electrical stimulation affects cardiomyocyte maturation. They are also used in disease modeling, for instance, studies on myocardial damage resulting from hypoxia, and also in drug screening applications [11]. Despite all being categorized under the umbrella term "EHT platform," each model's structure and functionality are distinctly unique, depending on the research question at hand. Therefore, a universal description of an EHT platform does not really exist. However, the latest EHT platforms typically share four key components: microtissues, microactuators, microsensors, and the platform (Figure 1.2). Each of these components play a critical role in simulating the physiological environment of the heart, enabling researchers to study heart function, disease, and drug responses in a controlled manner. The structure and function of an EHT platform can therefore best be explained by elaborating on these four key components.

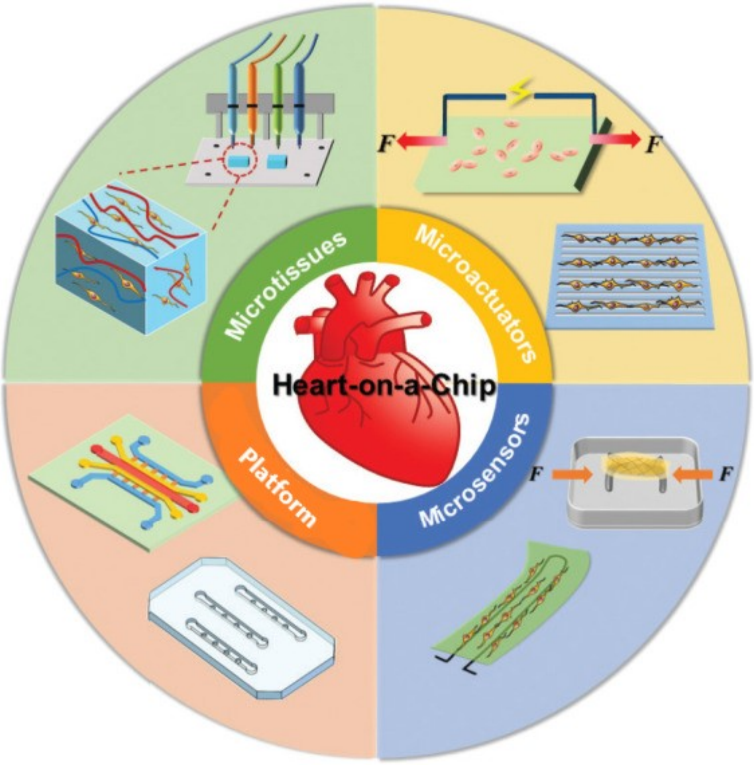

Figure 1.2: 4 components of an EHT platform. Figure adapted from [11].

**Heart microtissues** are engineered tissues composed of different cardiac cell types cultured in a 3D matrix to mimic the complex structure of real heart tissue. Microtissues for organ-on-a-chip applications are usually grown from stem cells. The most common stem cell types that are used for this purpose include adult stem cells (ASCs), induced pluripotent stem cells (iPSCs), and embryonic stem cells (ESCs) [8]. ASCs are stem cells found in various tissues of the adult human body. The most common human ASCs that are used for tissue engineering are mesenchymal stem cells (MSCs), which are stem cells that can easily be extracted from adult tissue, for example by taking biopsies. In the right environment, these cells can then grow into various cell types. This is generally achieved under the influence of specific biological signals generated by growth factors, and/or mechanical or magneto-electrical stimulation. A different type of stem cells that is sometimes used are embryonic stem cells (ESCs), which are stem cells derived from the inner cell mass of a developing embryo at the blastocyst stage, which is typically around five to six days after fertilization. These cells are obtained from surplus embryos donated for research purposes with the informed consent of the donors. Just like ASCs and hiPSCs, ESCs have the ability to differentiate into a wide range of cell types found in the human body. However, their availability is limited due to ethical concerns of some individuals and groups. Finally, hiPSCs are a type of stem cells that is generated in the laboratory by reprogramming adult cells, typically skin cells or blood cells, into a pluripotent state. Adult cells are more readily available than stem cells, which makes hiPSCs a valuable tool for tissue engineering, enabling greater scalability. However, the use hiPSCs (and other stem cells) has a significant drawback: the formed tissues are often functionally immature. For example, hiPSCs-derived cardiomyocytes typically resemble fetal or neonatal cardiomyocytes in terms of cell size and morphology, gene expression, myofibril contractility, and metabolic activity, which is a barrier to modeling and studying the heart in vitro [12]. Improving the maturitiy hiPSCs-derived cardiomyocytes (and other cell types) is therefore a topic of significant interest. Some recent studies report several methods to achieve this aim, such as prolonged culture [13], 3D microtissues composed of multiple types of cells [14], culturing on nanopatterned surfaces [15], and electromechanical EHT stimulation by incorporating microactuators [16].

**Microactuators** are used to mimic the mechanical and electrical conditions present in the heart. In native tissues, cells are exposed to a variety of electrical and mechanical signals that significantly affect cell behaviors and maturity. By mimicking these environmental cues, the microactuators help to recreate the environment of the heart *in-vitro*. The interaction between heart tissue and environmental factors is also a critical aspect of disease progression. For instance, factors that promote hypertrophy, such as energy depletion and increased workload resulting from prolonged hypertension, can hasten the progression of cardiac hypertrophy, leading to ventricular dysfunction and heart failure [17]. Microactuators can therefore also be used to engineer diseased cardiac tissues by modulating electrical and mechanical conditions.

**Microsensors** are used to monitor the physiological responses of engineered heart tissues, such as oxygen consumption, electrical activity, and contractility. Many types of sensors have already been used in EHT platforms, such as optical sensors [18], piezoelectric sensors [19], magnetic sensors [20], and electrochemical sensors [21].

Finally, the **platform** provides a microenvironment for the engineered heart tissues and allows for the integration of the other (optional) elements. To date, several platform types have been proposed for EHT platforms. Two recent examples include two-pillar engineerd heart tissue platforms, and biowires:

*Two-pillar engineered heart tissue platforms* are widely used for contractility assays. Heart tissue is grown around flexible anchors, and pillar deflection is measured as the heart tissue contracts. By measuring the contraction force, researchers can learn information about the functionality of the tissue. Several methods for measuring pillar deflection have been investigated, such as optical [18], piezo-electric [19] and magnetic sensing methods [20]. One of the most recent examples is a publication from Martins et al. They demonstrated a low-cost, adaptable, high-throughput device to quantify microtissue contraction utilizing video analysis in a 96-well plate design (Figure 1.3) [22]. Starting their experiment, cells were seeded into these wells in a collagen hydrogel. As the tissues formed, the tissues warped around the flexible pillars in the center of the wells. Once the tissues began to contract, the resulting pillar deflection could be monitored. Monitoring was performed optically utilizing a digital camera with pixel-based video analysis. Subsequently, the contraction force was determined as a function of the deflection of the pillars.

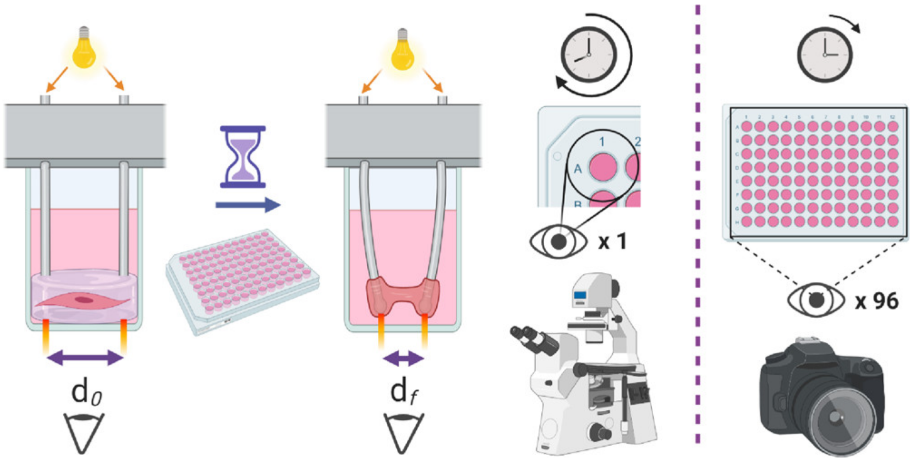

Figure 1.3: 2-pillar engineered heart tissue platform. The figure illustrates how tissues are grown around flexible pillars a 96-well plate design , after which pillar deflection is monitored using video analysis. Figure adopted from [22].

*Biowire platforms* are another type of platform that can be used for monitoring cardiac tissue contraction. Biowires enable growth of thin, cylindrical tissues, suspended between two parallel wires which allow optical quantification of displacement. Additionally, biowires can conduct electrical signals to electrically actuate the cells and promote cell differentiation and maturation, which can be particularly useful to replicate the native physiologic environment. Recently, Zhao et al. used the biowire platform to culture distinct atrial and ventricular tissue into a single chip (Figure 1.4) [23]. They exposed the tissues to several drugs and were able to show that the atrial and ventricular tissues had correct, and indeed different drug responses. To monitor tissue contraction, they used a combination of video analysis and calcium imaging.

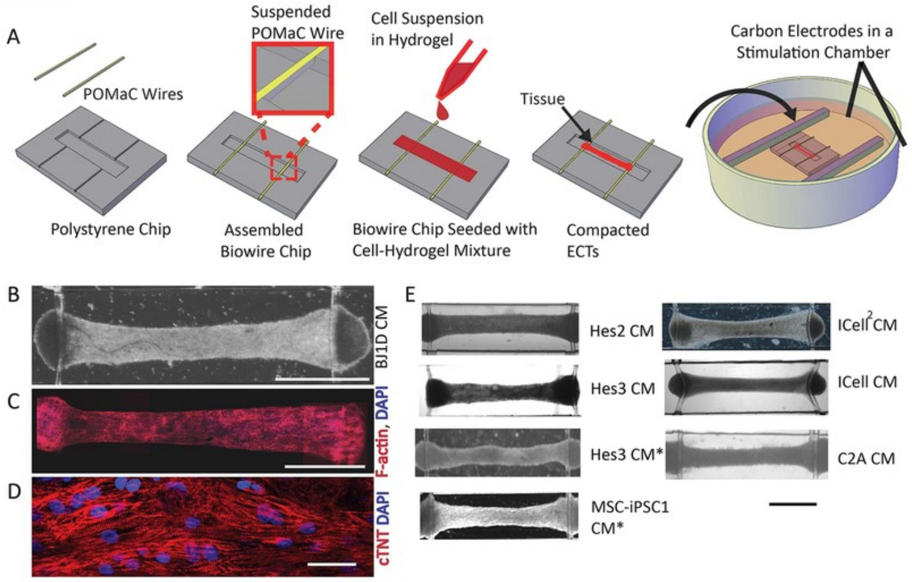

Figure 1.4: Biowire heart tissue platform. a) The figure illustrates how tissues are formed between two conductive wires. b-e) Results are presented from calcium imaging experiments conducted on the platform. Figure adopted from [23].

Although the recent developments in EHT platforms represent a major advance in our ability to study heart function and disease in-vitro, the development of EHT platforms poses several challenges. Major challenges related to tissue engineering include how to overcome the limited or non-existing proliferation capacity of mature cardiomyocytes, how to mimic the alignment and orientation of these cells when present in native heart tissue, and how to achieve a high level of tissue maturation [24]. More practical challenges for EHT platforms include the possibility of multiplexing and achieving high reproducibility. Lastly, other challenges that lay a bit further in the future include challenges such as multi-tissue engineering, and the design of multi-organ-on-a-chip platforms, to more accurately recapitulate the complex environment of the human body [25] [26].

## 1.3 EHT platform design by TU Delft and LUMC

To address the challenges in the field of EHT platforms, the TU Delft and Leiden University Medical Center (LUMC) started working on a new design of an EHT platform. Milica Dostanic, as main contributor to this project, was recently promoted for her research on this topic. In her PhD thesis, a comprehensive investigation was conducted to design and fabricate an advanced EHT platform.

The system called Heart-Dyno, developed by the research group from QIMR Berghofer Medical Research Institute, was used as starting point (Figure 1.5) [27]. The Heart-Dyno consists of two rectangular micropillars surrounded by an elliptic well of the same height as the micropillars, and can be used for contractility assays. The Heart-Dyno system was selected as starting point for the design due to its small PDMS-based construction, making it potentially suitable for cleanroom fabrication and sensor integration. Moreover, this platform is compatible with a standard, stand-alone 96-well plate, enabling easy adoption by pharmaceutical companies in their existing robotic pipelines, as well as by research laboratories in academia. However, the Heart-Dyno system does have a few drawbacks. Firstly, its current manufacturing methods rely on manual PDMS moulding, which may limit scalability. Secondly, since the device is still quite big, it utilizes relatively high cell numbers per tissue, which can be challenging from a tissue engineering perspective. Thirdly, there are neither electrical nor mechanical actuators integrated in the design. And lastly, it relies solely on optical readout, which restricts the range of data that can be obtained from the system.

Milica Dostanic therefore started by downscaling this original device, using wafer-level microfabrication techniques, and gradually enhanced the platform by incorporating electrical stimulation and readout capabilities. This downscaled platform was fabricated using PDMS moulding into deep reactive ion-etched cavities on a silicon wafer. Furthermore, the micropillars were redesigned in a novel tapered shape, ensuring tissue confinement within the central region of the pillars (Figure 1.6a).

As next step to further enhance the EHT platform, co-planar capacitive force sensors were integrated into the platform, with the aim to allow real-time measurements of tissue contraction force (Figure 1.6b). The working principle of the sensors is based on detecting the small compression and tension occurring in the substrate below PDMS pillars, upon

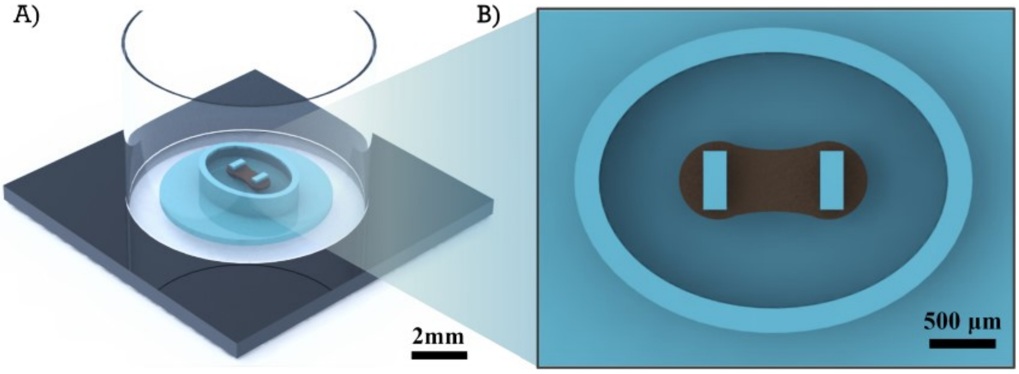

Figure 1.5: A) 3D model of the heart-dyno platform; PDMS structure (in blue) at the bottom of a single well of a 96-well plate, with the tissue (brown) formed around two micropillars, surrounded by an elliptic microwell. B) Close-up image of the tissue within elliptic microwell. Figure adopted from [3].

tissue contraction and subsequent pillar displacement. The sensors were successfully fabricated and demonstrated promising results; however, challenges regarding assembly processes need further attention.

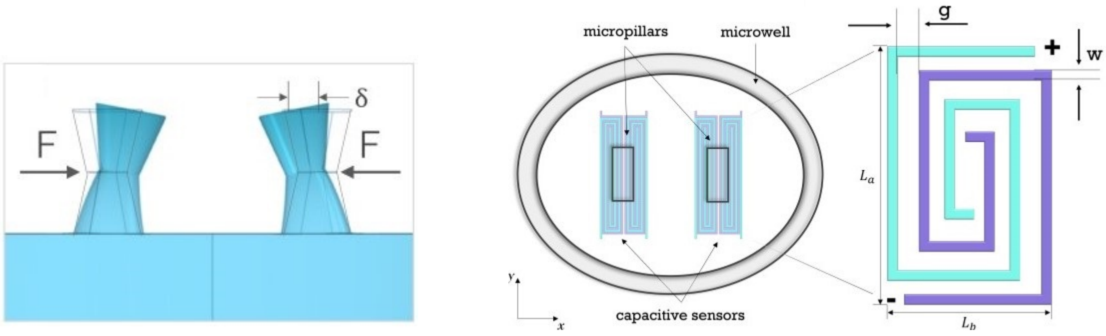

(a) (b)

Figure 1.6: a) Side-view of the platform: illustrating the re-designed tapered pillar geometry and the expected deformation due to tissue contraction. b) Top-view of the platform: llustrating the capacitive sensors underneath the pillars.

In parallel with sensor development, electrical stimulation was introduced to enhance the maturation of cells within the platform. Microelectrodes were integrated into the platform, in between the pillars, to provide uniform electric field stimulation to the tissue. A circuitry system was also designed for biphasic rectangular pulse generation.

The final step in this thesis was upscaling and integration of the device into a multi-well plate-like system for high-throughput experiments. A 32 chip, multi-well system was developed with pacing electrodes that enabled electrical stimulation of individual wells. Control of the pacing signal and individual well selection was realized via the user interface of a developed Matlab-based application. However, improvements to the assembly process are required in terms of automating the assembly steps and preventing leakage. Figure 1.7 represents an illustration of the final design, as future outlook.

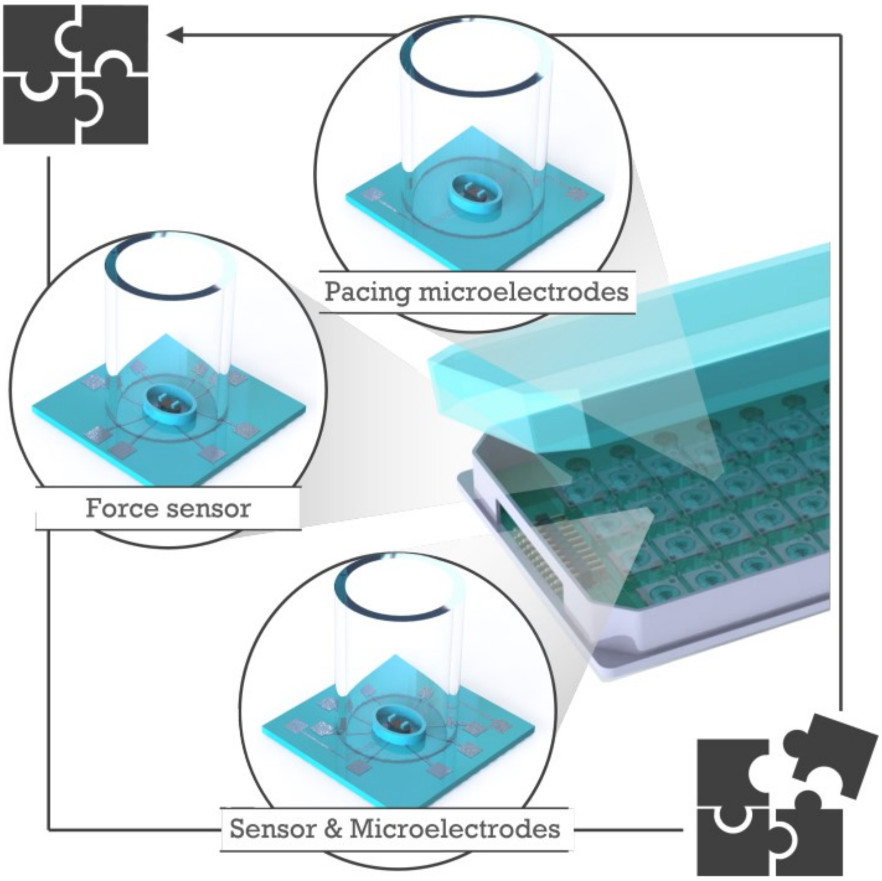

Figure 1.7: Illustration of the final design integrated in a multi-well plate, as future outlook. Figure adopted from [3].

## 1.4 Main challenges

The EHT platform developed by TU Delft and LUMC still encounters several challenges. While some of these have been mentioned in previous sections, this part will detail the issues underlying the challenges related specifically to the capacitive sensors.

**Challenge 1: Sensitivity optimization for the capacitive sensors.**

First and foremost, it is important to mention that the initial platform was equipped with integrated capacitive sensors tailored specifically for straight pillars. However, since platform redesign features tapered pillars, it is necessary to modify the capacitive sensors to maintain optimal performance. Therefore, the challenge at hand involves redesigning the capacitive sensors to be optimized for tapered pillars, while simultaneously focusing on enhancing sensitivity.

**Challenge 2: Alignment of the capacitive sensors.**

Another problem that reduced performance of the capacitive sensors was misalignment between the capacitive sensors and the micropillars. To understand this issue, it is essential to have some insight into the sensor fabrication process. Briefly, the platform comprises two separate PDMS substrates: one containing the pillars and microwell, and the other containing the sensors. These two substrates are subsequently bonded together using PDMS as glue. The alignment and bonding of these substrates is performed manually, making the process prone to alignment errors, as illustrated in Figure 1.8. Such misalignment can adversely affect sensor performance.

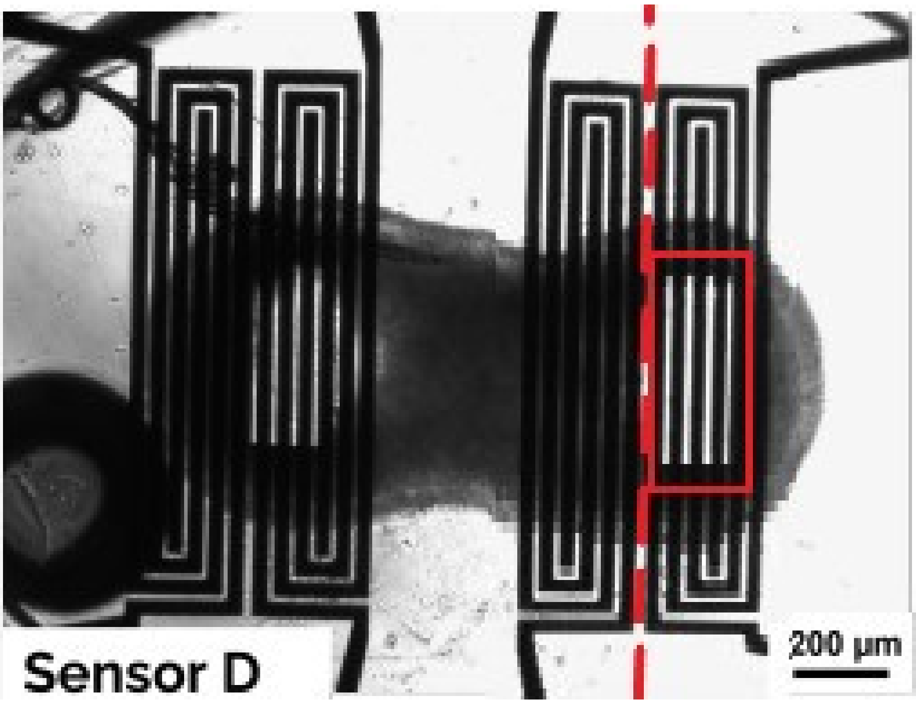

Figure 1.8: Examples of alignment issue of the capacitive sensors with the micropillars. Figure adopted from [3].

**Challenge 3: Mechanical strengthening of the electrical connections of the capacitive sensor.**

In two assembly steps of the EHT platform with integrated capacitive sensors, the electrical connections demonstrated to be susceptible for cracking. This happened when the sensors were transferred to the PCB, and during wirebonding. Figure 1.9 shows pictures of the cracks at several locations.

Due to the difference in stiffness between patterned aluminum tracks and PDMS, upon bending and out-of-plane deformation, the thin metal interconnects were subjected to stress resulting in metal disruption (Figure 1.9A,C). The point where contact pads for wirebonding and the interconnects merge is particularly susceptible to disruption due to the abrupt transition from a large contact pad area to a thin metal line (Figure 1.9B). Finally, during wirebonding, the pressure of the bonding needle causes cracks in the contact pad, disrupting the metal connection (Figure 1.9D).

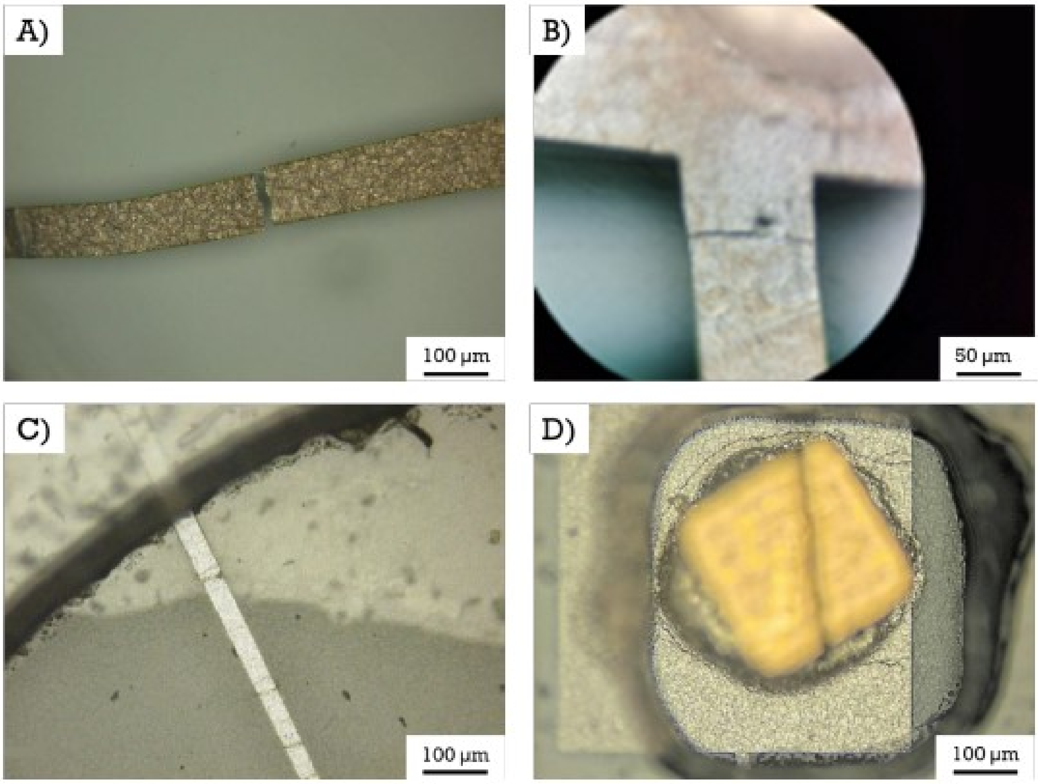

Figure 1.9: Examples of metal connection disruptions during the assembly process. A) broken interconnect during pillar bonding; B) broken connection at the contact pad; C) bent interconnects due to the transfer process; D) crack at the contact pad after golden shim gluing. Figure adopted from [28].

## 1.5 Project plan

The EHT platform developed by TU Delft represents a commendable effort in tackling some of the main challenges in EHT platforms, as described in 1.2. The downsized version of the HeartDyno platform enables a precise and scalable fabrication process within a cleanroom environment. The inclusion of integrated electrodes enables active stimulation of cardiac tissues to enhance cell maturation and the possibility to pace the tissues for synchronous beating. Additionally, the capacitive sensors enable to possibility to measure cardiac contractility in real-time without the need for bulky optical microscopes. Given the promising nature of this design, the objective of this thesis is to build upon it. In pursuit of this goal, the following main objective, project boundaries, and activities have been formulated:

### Main objective

The main objective is to make a re-design of the EHT platform with the following requirements: the design is optimized for higher performance of the capacitive sensors, and the design is less prone to mechanical failure.

### Thesis structure

Chapter 1 offers a brief introduction to organ-on-chip technology, the prior advancements in developing a new EHT platform, and the key challenges faced by the new design.

Chapter 2 summarizes the literature review conducted to gather insights on sensor optimization and the fabrication of metal structures on PDMS substrates.

Chapter 3 focuses on numerical simulations performed to identify the optimal sensor design for enhanced sensitivity.

Chapter 4 outlines the design updates, incorporating findings from the literature review and numerical simulations.

Chapter 5 details the fabrication process of the updated design.

Chapter 6 presents the electrical characterization of the design, aiming to assess the feasibility of using these sensors for tissue contractility assays, the ultimate goal of this research.

# 2 Literature review

This chapter provides a summary of the main findings of the literature study that has been conducted. By focusing on recent articles, the aim was to provide an up-to-date understanding of the current state of knowledge and advancements in the field of capacitive sensors and microfabrication. The primary objective of this literature research was to gather recent and pertinent information on the previously formulated research questions:

1. *How can the performance of the capacitive sensors be optimized?*
2. *How can the fabrication process be improved in order to minimize mechanical failure without compromising on sensor performance?*

## 2.1 Sensor optimization

The design of the previous capacitive sensor was based on a study from Mahdieh Shojaei Baghini [29]. In this study, several force assessment strategies were investigated to determine the most suitable sensing strategy for the specific purpose of force assessment on the EHT platform. A comparative analysis was done between capacitive, piezo-electric and piezo-resistive transduction mechanisms, and several designs for these sensors were compared. Ultimately a co-planar spiral capacitive sensor was chosen as final design.

Capacitive sensors operate on the principle of capacitance, which is the ability of two conductive plates separated by an insulating material (the dielectric) to store an electric charge [30]. Generally, when a potential is applied between two adjacent plates, separated by a dielectric, an amount of charge builds up on both plates. As result of this stored charge, an electric field is produced. Conventionally, capacitors typically adopt a parallel-plate configuration, where the driving and sensing electrodes are positioned facing each other in close proximity. This arrangement establishes a uniform electric field between the electrodes. When the electrodes gradually open up, the electric field is no longer confined within a small region between the electrodes, but expanded into a wider space and forms a fringe field. When the electrodes are in co-planar position, the fringe field takes on a more prominent role between the driving and sensing electrodes. The transition from a parallel-plate capacitive sensor to a co-planar capacitive sensor is illustrated in Figure 2.1. Mechanical deformation of the capacitor plates, or the dielectric in between them, will result in a change in the distribution of the electric field, which can be measured as a change in capacitance across the plates. The change in capacitance can be correlated to the mechanical displacement, which in turn is a function of tissue contraction force. The envisioned capacitive tissue contractility assay on the EHT platform is based on this principle. In the previous study from Baghini, a co-planar capacitive sensor with spiral geometry was chosen as final design. Compared to parallel plate capacitive sensors, co-planar capacitive sensors are less difficult to fabricate using layer-by-layer microfabrication techniques, and can be made very thin [31].

In co-planar spiral capacitive sensors, the two oppositely charged plates are organized in a spiral geometry. Each metal plate interacts via fringe fields with the neighboring plate. In the final design from Dostanic, two spiral capacitors are positioned below each

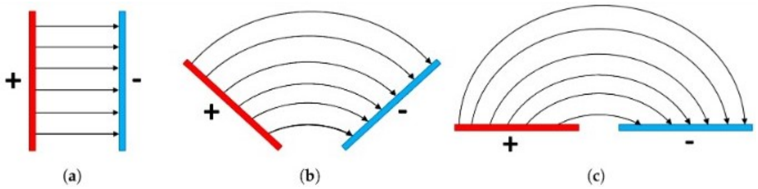

Figure 2.1: Illustration of electric field produced by oppositely charged plates. a) in planar configuration b) electrodes open up c) in co-planar configuration. Figure adopted from [32]

pillar, as was depicted in Figure 1.6b. The expected displacement distribution of the substrate, as result of tissue contraction, is illustrated in Figure 2.2.

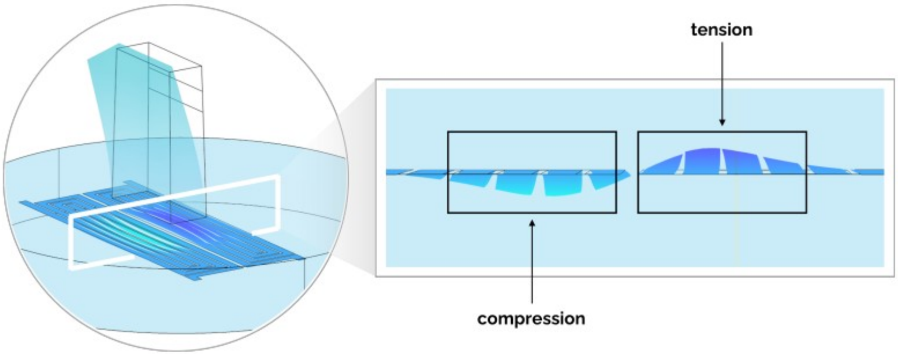

Figure 2.2: Illustration of the sensor plates displacement, in two co-planar capacitors, due to the compression and tension occurring in the elastic substrate upon pillar bending. Figure adopted from [3].

The capacitive sensors will be used to measure this placement, and their performance in doing this can be evaluated by their sensitivity, dynamic range, response time, relaxation time, penetration depth, signal strength, and detection limit [30] [33]. Sensitivity is defined as the ratio of changes in the sensors capacitance to changes in force applied upon the pillars, according to Formula (1).

$$S = \frac{\Delta C}{\Delta F} \tag{1}$$

Where S represents the sensitivity, ΔC is the relative change of capacitance, and ΔF is the change in tissue contraction force. The improvement in sensitivity is mainly realized by increasing the change in capacitance within a certain force range. The dynamic range is the range of forces in which the signal response is detectable. A sensor may possess multiple linear regimes within the dynamic range, each with a corresponding sensitivity value [33]. Response and relaxation times are critical parameters in determining the speed at which the sensor can be probed, which can be important for applications like pulse waveform evaluation, where the sensor must be able to respond quickly enough to accurately detect each (heart)beat. Response time is defined as the time it takes for a sensor to reach its final signal amplitude for an applied pressure, and relaxation time is defined as the time it takes for the sensor to return back to its original signal once the applied pressure is removed [33]. Penetration depth refers to the distance from the surface of the sensor at which it is sensitive to changes in the electric field. Since the sensor will be used to detect changes only in very close proximity to the sensor, the penetration depth should be kept small to avoid influence from events outside of the sensing area. Signal strength refers to the magnitude of the electrical signal generated by the capacitive sensor. With a strong signal, the capacitive sensing system can more reliably differentiate between different situations. Finally, the detection limit is the minimum force that can be sensed, and is used to evaluate if a sensor is capable of detecting forces for a given application.

Several techniques have been extensively researched that could help optimizing the capacitive sensor performance. The most important ones include optimizations in sensor geometry, the dielectric layer, the electrode layer, and shielding and guarding. Among these, sensor geometry was found to be the most important parameter for optimizing sensor sensitivity. It was shown that different geometries produce electric fields with different sensitivity distributions. Important parameters included the shape and orientation of the electrodes, the number of electrodes, the width of the electrodes and the spacing between them. The optimal geometry was also found to be dependent on the direction of the load. For optimal sensitivity, the geometry should aim to maximize the effective length, and maximize capacitance change upon deformation. However, trade-offs with signal strength and penetration depth are inevitable.

The di-electric layer equally influences sensor performance. Main sensor characteristics that can be optimized by the di-electric layer are the sensitivity, signal strength, response and relaxation times. In recent literature, optimizations of the di-electric layer have mainly been focused on optimizing the sensitivity. These approaches seek to amplify capacitance change for a given input, either by increasing signal strength or increasing compressibility. This was achieved by utilizing innovative PDMS composites, adding conductive layers, or with micro-structured di-electric layers. However, these enhancements introduce trade-offs involving mechanical properties, non-linearity, and dynamic range.

Micro patterning of the electrodes was also centered around the idea to increase sensitivity by increasing compressibility, and by increasing the electrode surface area. Increasing the electrode surface allows for more charge to be stored on the electrode surfaces, which increases the ability of the capacitor to hold charge.

Lastly, shielding and guarding was shown to be beneficial for limiting stray capacitance and for shaping the electric field, with trade-offs in sensitivity and signal strength. Furthermore, in flexible systems it is difficult to account for the additional capacitance that exists between the shield and the sensing electrodes, as this can fluctuate under the influence of applied forces.

## 2.2 Metal structures in PDMS substrates

Polydimethylsiloxane (PDMS) possesses a wide range of advantageous characteristics for its application in the EHT platform. It is bio-compatible, commercially available, low cost, stretchable, and compatible with microfabrication processes [34]. Another very important factor is that its Young's modulus can be tuned, making it closely resemble muscle tissue [35]. However, the successful patterning of metal structures on top of PDMS substrates encounters challenges primarily attributed to the mechanical mismatch between the two materials [36]. The mismatching mechanical properties of PDMS and metals, such as stiffness and thermal expansion coefficients, lead to issues like delamination, cracking, and deformation during fabrication and usage.

The standard method for fabricating metal structures on soft PDMS substrates involves a combination of soft lithography and photolithography techniques [37]. The substrate is fabricated independently from the metal structures. Then, depending on the material used, a strategy is chosen to integrate the metal structures within this substrate. For the deposition of metals on the PDMS surface, different methods can be utilized, depending on the material and the desired film thickness. Commonly-used methods to deposit metals on PDMS include evaporation [38], sputtering [39], and electroplating [40]. The challenges encountered during the deposition of metal structures on PDMS stem from various factors. Notably, the presence of unreacted oligomers after the preparation of PDMS easily diffuse and dominate the surface properties, preventing an efficient metalization process [41]. Furthermore, PDMS has a low surface energy and, consequently, has poor adhesion to metals. Lastly, the mismatch in thermal expansion coefficient between the metal and PDMS can lead to cracks in the metal lines and even the PDMS surface beneath the metal lines [42].

In order to improve the resistance to cracking of metal-PDMS devices, some alternative methods for the metalization of PDMS have also been developed. These methods include spin-coating of flexible polymer composites with conductive nanoparticles [43], spin-coating inherently-conductive polymers [44], screen printing [45], and inkjet printing [46] with conductive inks. While these methods can produce impressive flexible microstructures, the conductivity of polymer-based conductors is generally lower than that of metals. Furthermore, printing is also more limited in resolution than photolithography [37]. Therefore, to achieve highly-conductive flexible electronics, the development of reliable processes for the metalization of polymers remains an important area of research.

Another different method for reducing stress in the metal layer is the use of an extra intermediate layer between the metal and the PDMS [47] [48]. A commonly used material for this intermediate layer is polyimide. Polyimide has a Young's modulus between the PDMS and the metal (approximately 3.2 GPa), which makes the transition less steep and reduces the accumulation of strain in the metal interconnects [48]. Furthermore, polyimide has remarkable adhesion to metals and is high temperature resistant, which overcomes the difficulties with metalization of the PDMS, as explained in Section 2.2. Embedding within this intermediate layer can be performed single-sided or double-sided, of which double-sided demonstrated the highest increase in stiffness [48]. Intuitively, increasing the layer thickness also increases stiffness. However, adding stiffness potentially reduces the sensitivity of the capacitive sensors as well, as they are reliant on deformation. In order to circumvent this issue, Chou et al. [49] also investigated PDMS filling with parylene, which has similar mechanical properties as polyimide. Instead of depositing a whole parylene intermediate layer, only nano-scale pores on PDMS surfacewere filled with parylene. While this technique resulted in mechanical properties more closely resembling those of pure PDMS, it proved to be less effective in mitigating the formation of cracks.

To improve adhesion with metals, surface modification of the PDMS is often used. A treatment that is commonly used is oxygen plasma treatment [41]. Oxygen plasma treatment increases the surface energy of the PDMS by introducing polar OH- groups that make the surface hydrophilic. This makes the surface more capable of forming stronger bonds with other materials such as metals [50].

For any fabrication method, the use of PDMS as substrate for the fabrication of metal sensors leads to an incompatibility issue: On one hand, the flexibility of the polymer shouldn't hinder the fabrication process, such as the risk of bonding issues. And on the other hand, some applications will require a certain flexibility, e.g. to mimic the physiological environment of heart tissue, or to optimize sensor performance. In other words, a compromise is necessary between higher stiffness that would be beneficial for processing, and higher flexibility that could be beneficial for optimizing sensor sensitivity.

## 2.3 Conclusion

This chapter presented a summary of the fundamental factors influencing sensor performance and the fabrication techniques used to create metal structures on PDMS substrates. While these two aspects may seem distinct, this chapter highlights their interconnectedness. Most ideas that aim to optimize the adhesion and minimize cracking are centered around the idea to increase stiffness of the substrate. However, the most important trade-off is that by increasing the substrate stiffness, the sensor sensitivity will also be reduced.

The main challenge is therefore to address the fabrication issues related to patterning thin metal structures on soft substrates and make the process as robust as possible, while trying not to adversely affect sensor sensitivity. Therefore, setting up a detailed simulation environment is a good first step for the re-design of the capacitive sensors. The setup of this simulation environment is what will be discussed in the following chapter.

# 3 Numerical simulations and analysis

The new design of the capacitive displacement sensors was developed by using numerical simulations to investigate the substrate deformation, and determine the best sensor position and geometry. This chapter describes how the simulations have been executed, and which conclusions were drawn from them. The chapter starts with an analytical model to calculate the base capacitance of the sensors within the EHT platform. The analytical model served as a benchmark for subsequent simulations. Following the analytical model, a numerical model was constructed, yielding capacitance values in alignment with the analytical model. The investigation then deepened into the substrate's deformation to identify the optimal sensor position and geometry.

## 3.1 Analytical model

An analytical framework for determining the base capacitance of a co-planar capacitive sensor was already developed in previous work from Mahdieh Shojaei Baghini [29]. However, this model did not yet account for the presence of cell culture medium atop the PDMS substrate. Given that cell culture medium has a relatively high permittivity, its presence could significantly increase the parasitic capacitance. Parasitic capacitance is increased due to the medium's ability to store additional electric charge, which interferes with the sensor's intended measurements. In order to understand the contribution of the cell culture medium to the parasitic capacitance, a revised analytical model was developed to serve as a benchmark for future simulations. This updated model calculates the capacitance in a multi-layered dielectric environment, utilizing principles derived from co-planar waveguide theory [51].

In this theoretical framework, the capacitive sensor is simplified to three oppositely charged metal lines, arranged adjacently, as depicted in Figure 3.1. The metal lines are encapsulated with different stacked dielectric layers, with their respective permittivities ($\varepsilon$). By calculating the effective permittivity of the whole system ($\varepsilon_{\mathrm{eff}}$), the base capacitance per unit of length for the sensor can be calculated. Then, the capacitance for the whole sensor was calculated by multiplying this base capacitance by the sensor's average path length. The analytical model assumes that the capacitive sensor is surrounded by air, which has a relative electrical permittivity of 1.

According to the co-planar waveguide theory, the capacitance for the whole system can be calculated using the following formula:

$$C_{tot} = C_0 \cdot \epsilon_{eff} \cdot l_{av} \tag{2}$$

Where $\varepsilon_{\mathrm{eff}}$ is the effective permittivity of the whole system, which is composed of multiple di-electric layers, each with their own permittivity ($\varepsilon$). $\mathrm{C}_0$ is the capacitance in absence of any di-electric layer, and $\mathrm{l}_{\mathrm{av}}$ is the average path length of the sensor.

The capacitance in absence of all dielectric layers ($\mathrm{C}_0$) is given by:

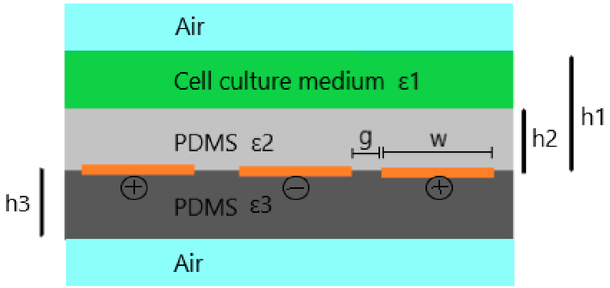

Figure 3.1: Schematic of a multilayered dielectric substrate. Capacitor plates are depicted in orange.

$$C_0 = 4\epsilon_0 \frac{K(k')}{K(k)} \tag{3}$$

Where K is the complete elliptical integral of the first kind. The arguments k and k' are dependent on the geometry of the sensor and are given by:

$$k = \frac{c}{b}\sqrt{\frac{b^2 - a^2}{c^2 - a^2}} \tag{4}$$

$$k' = \sqrt{1 - k^2} \tag{5}$$

a, b and c are geometrical constants that depend on the width (w) of the sensor lines and the gap (g) between them:

$$a = \frac{w}{2} \tag{6}$$

$$b = \frac{w + 2g}{2} \tag{7}$$

$$c = \frac{3w + 2g}{2} \tag{8}$$

The effective permittivity can be calculated using:

$$\epsilon_{eff} = \frac{C}{C_0} \tag{9}$$

Where C is a summation of all partial capacitances from each dielectric layer:

$$C_1 = 2\epsilon_0(\epsilon_1 - 1)\frac{k(k_1')}{K(k_1)} \tag{10}$$

$$C_2 = 2\epsilon_0(\epsilon_2 - \epsilon_1)\frac{k(k_2')}{K(k_2)} \tag{11}$$

$$C_3 = 2\epsilon_0(\epsilon_3 - 1)\frac{k(k_3')}{K(k_3)} \tag{12}$$

$k_i$ and $K_i$ can be calculated using:

$$k_i = \frac{sinh(\frac{\pi c}{2h_i})}{sinh(\frac{\pi b}{2h_i})}\sqrt{\frac{sinh^2(\frac{\pi b}{2h_i}) - sinh^2(\frac{\pi a}{2h_i})}{sinh^2(\frac{\pi c}{2h_i}) - sinh^2(\frac{\pi a}{2h_i})}} \tag{13}$$

and

$$k_i' = \sqrt{1 - k_i^2} \tag{14}$$

By combining formulas 3, 10, 11, and 12, the effective permittivity can be expressed as:

$$\epsilon_{eff} = 1 + \frac{1}{2}(\epsilon_1 - 1)\frac{K(k)}{K(k')}\frac{K(k_1')}{K(k_1)} + \frac{1}{2}(\epsilon_2 - \epsilon_1)\frac{K(k)}{K(k')}\frac{K(k_2')}{K(k_2)} + \frac{1}{2}(\epsilon_3 - 1)\frac{K(k)}{K(k')}\frac{K(k_3')}{K(k_3)} \tag{15}$$

After finding $C_0$ and $\varepsilon_{\text{eff}}$ , the capacitance of whole system can be calculated using equation 2. With this analytical framework, the base capacitance of four different sensor designs was calculated and compared to numerically found values. These results are given in the following subsection.

## 3.2 Numerical model

### 3.2.1 Simulation set-up

The numerical model was built to include the tapered pillar geometry and the effect of cell culture medium into the analysis. Figure 3.2 provides a visual representation of the simulation setup and includes the settings used for the simulation. The sensor is embedded in a PDMS substrate (blue), with a cell culture medium atop (light grey). A force is applied in the center of the pillar (green). This setup enabled the detailed examination of the resultant deformation and the corresponding changes in capacitance. Furthermore, two scenarios were examined: one in which the substrate is supported from beneath, and another where it is suspended. These distinct scenarios are defined by their fixed constraints. A fixed constraint specifies a surface that remains immobile throughout the simulation. For a supported substrate, the constraint is on the bottom surface, preventing any downward movement. Conversely, in a suspended substrate scenario, the substrate is free to move vertically, but its outer edges are immobilized, indicating that it is held in place at these points.

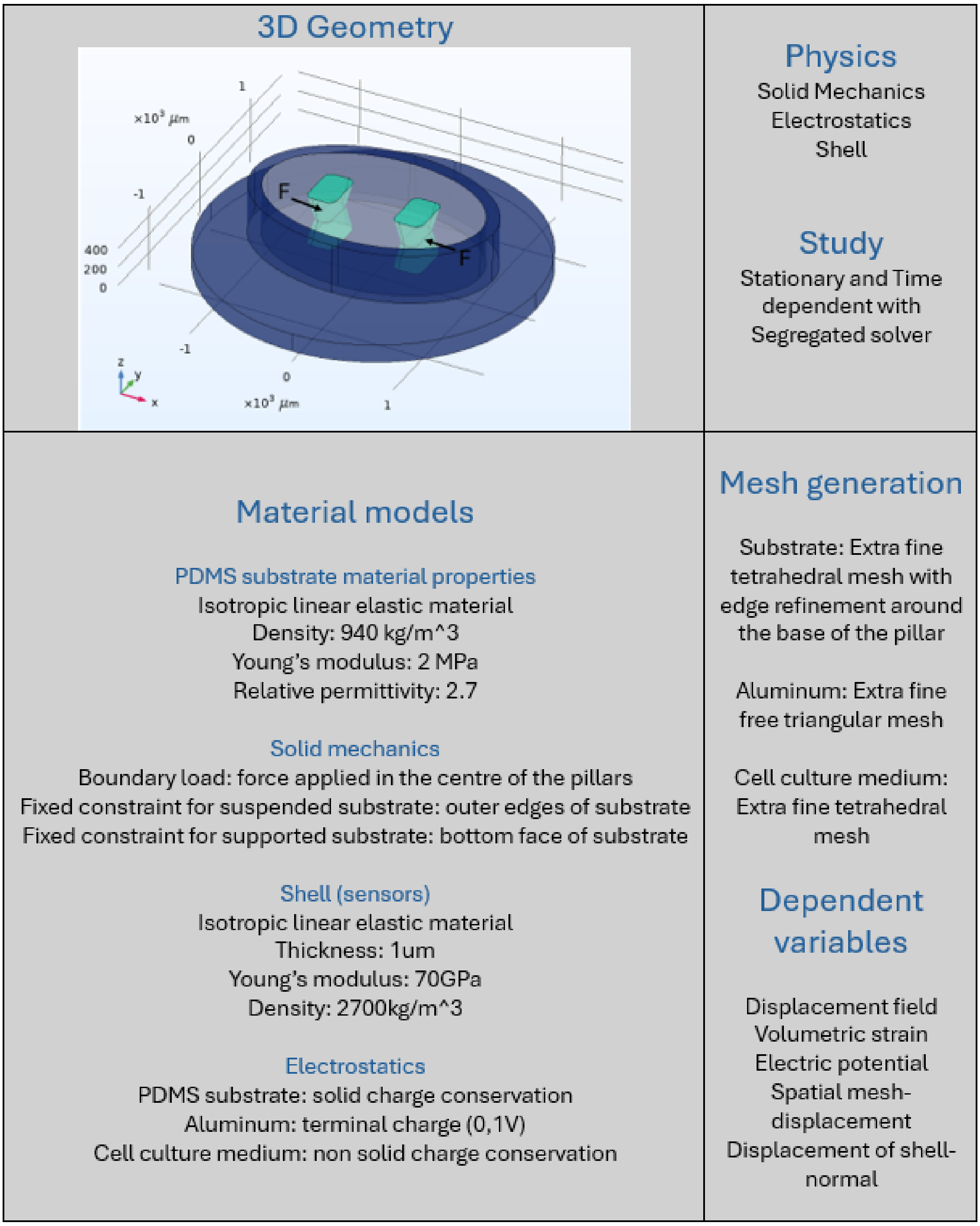

3D Geometry

Physics
Solid Mechanics
Electrostatics
Shell

Study
Stationary and Time dependent with Segregated solver

Material models

PDMS substrate material properties
Isotropic linear elastic material
Density: 940 kg/m^3
Young's modulus: 2 MPa
Relative permittivity: 2.7

Solid mechanics
Boundary load: force applied in the centre of the pillars
Fixed constraint for suspended substrate: outer edges of substrate
Fixed constraint for supported substrate: bottom face of substrate

Shell (sensors)
Isotropic linear elastic material
Thickness: 1um
Young's modulus: 70GPa
Density: 2700kg/m^3

Electrostatics
PDMS substrate: solid charge conservation
Aluminum: terminal charge (0,1V)
Cell culture medium: non solid charge conservation

Mesh generation

Substrate: Extra fine tetrahedral mesh with edge refinement around the base of the pillar

Aluminum: Extra fine free triangular mesh

Cell culture medium: Extra fine tetrahedral mesh

Dependent variables

Displacement field
Volumetric strain
Electric potential
Spatial mesh-displacement
Displacement of shell-normal

Figure 3.2: Simulation set-up.

In order to verify the results from the simulations, the base capacitance of four previously developed spiral sensor designs was determined through both analytical and numerical methods. The outcomes of these calculations were then compared. The relevant geometrical properties of the spiral sensors are listed in Table 1. Table 2 presents a comparison of the analytical and numerical values obtained.

| | Sensor A | Sensor B | Sensor C | Sensor D |
|---|---|---|---|---|
| Gap width (w) | 5 µm | 10 µm | 5 µm | 10 µm |
| Line width (g) | 20 µm | 10 µm | 5 µm | 40 µm |
| Average length (l) | 6310 µm | 7554 µm | 13521 µm | 3995 µm |

Table 1: Geometrical properties of original spiral sensors. Dimensions are as indicated in Figure 1.6b.

| | Sensor A | Sensor B | Sensor C | Sensor D |
|---|---|---|---|---|
| Base capacitance analytical (F) | 5.43e-13 | 4.03e-13 | 7.21e-13 | 2.97e-13 |
| Base capacitance numerical (F) | 5.39e-13 | 3.96e-13 | 8.15e-13 | 3.02e-13 |

Table 2: Comparison base capacitance analytical vs numerical.

### 3.2.2 Effect of cell culture medium

To assess the impact of the added cell culture layer on the sensor's total capacitance, the sensor's base capacitance was calculated at varying depths, as shown in Figure 3.3. The presence of a cell culture medium with high permittivity on top of the PDMS substrate leads to a notable increase in capacitance. This increase plateaus after a certain depth, depending on the sensor design. Indicating that beyond this depth, the electric field predominantly remains within the PDMS substrate and does not significantly interact with the cell culture medium above the PDMS substrate. The distance to which the electric field extends was also described as the "penetration depth" in the literature review. Factors such as gap width and line width influence the penetration depth of the sensor [52]. This effect is also visible in Figure 3.3: sensors with a narrower gap and line width, and thus a smaller penetration depth, demonstrate a smaller change in capacitance by the addition of the cell culture medium.

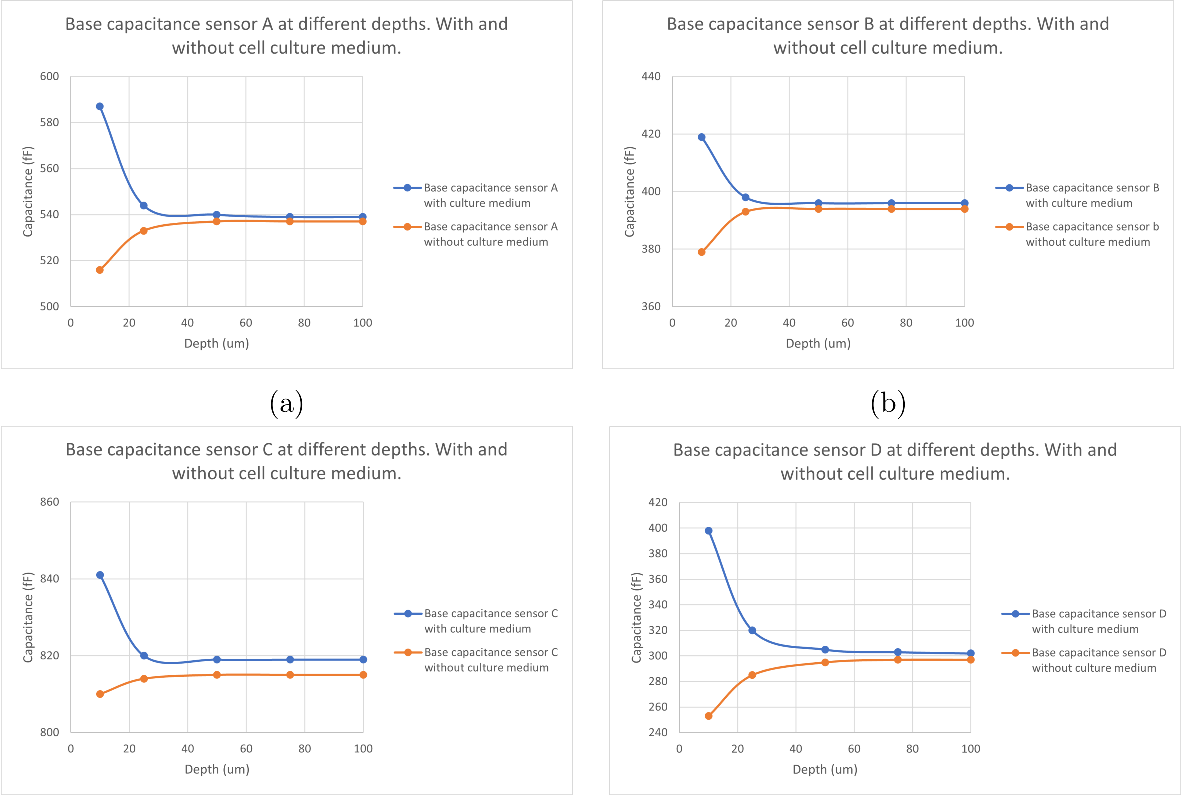

(a) (b)

(c) (d)

Figure 3.3: Analysis of the base capacitance with and without culture medium for different sensor designs.

## 3.3 Supported substrate

### 3.3.1 Sensor position

In order to determine the optimal position of the sensor when the substrate is supported, the substrate deformation as result of the tissue contraction was investigated using the previously described numerical model in Comsol. A force of 50 µN (assumed minimal force of engineered heart tissue) was applied in the middle of the pillars, as indicated in Figure 3.4a. Figure 3.4b also shows a visual representation of the expected deformation of the substrate due to the applied force.

Since the deformation of the substrate beneath both pillars is symmetrical, the two-pillar model was simplified to a single-pillar model in subsequent simulations, which helped with reducing the computational load. In order to investigate the displacement of the substrate, the displacement of the substrate was evaluated along x, y, and z directions from the base of the pillar. The displacement measurements were visualized by plotting the deformation along two lines (line A and B in Figure 3.15b). The results for the displacement along these lines at different depths are presented in Figure 3.15c and 3.15d.

Based on these results, it can be concluded that most of the deformation occurs within 300 µm on each side from the center of the pillar in x-direction, and about 400 µm in

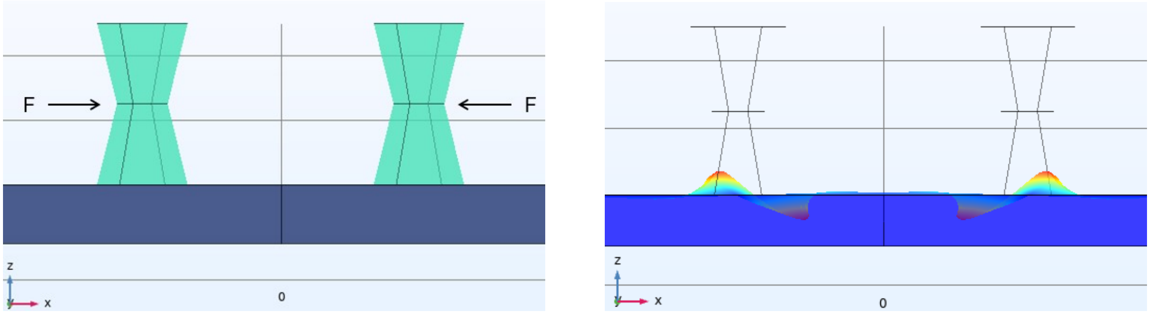

(a) (b)

Figure 3.4: Visual representation of substrate deformation in supported configuration. a) Substrate and pillars before applying force. b) Simulated substrate deformation after applying force.

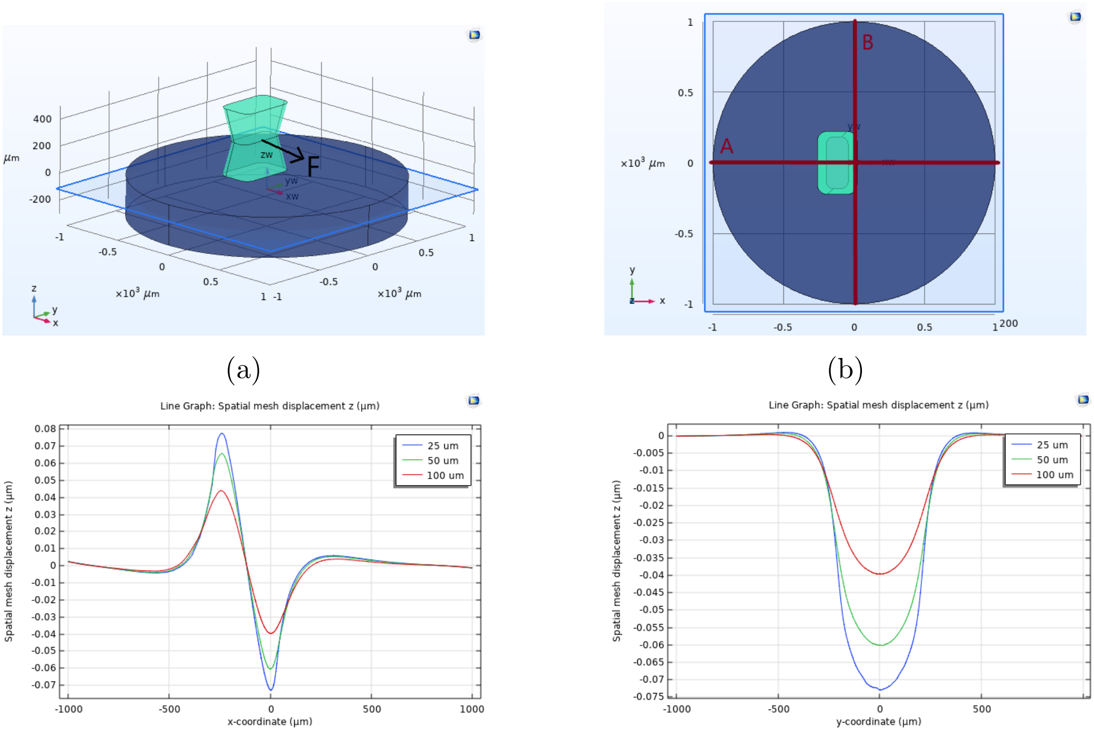

(a) (b)

(c) (d)

Figure 3.5: Analysis for optimal sensor position. a) Simulation set-up: force (50 µN) applied in the center of the pillar and the vertical displacement of the substrate is investigated along a plane at three different depths. b) The displacement is investigated along two different cross-sections of the plane, indicated with line A and line B. c) Results for the deformation of the substrate along line A. d) Results for the deformation of the substrate along line B.

y-direction. This is the area in which the new sensor design should be positioned. The results also show that most of the deformation happens close to the surface, and gradually decreases deeper within the substrate.

In order to find the optimal depth of the sensor, the sensitivity of a single sensor design (sensor A) was evaluated at different depths into the substrate. The results are depicted in Figure 3.6. Sensitivity was determined through time-dependent studies using a sinusoidal force. A sensor was positioned near the base of the pillar, and the maximum change in capacitance was divided by the applied force during the simulation, in accordance with Formula 1.

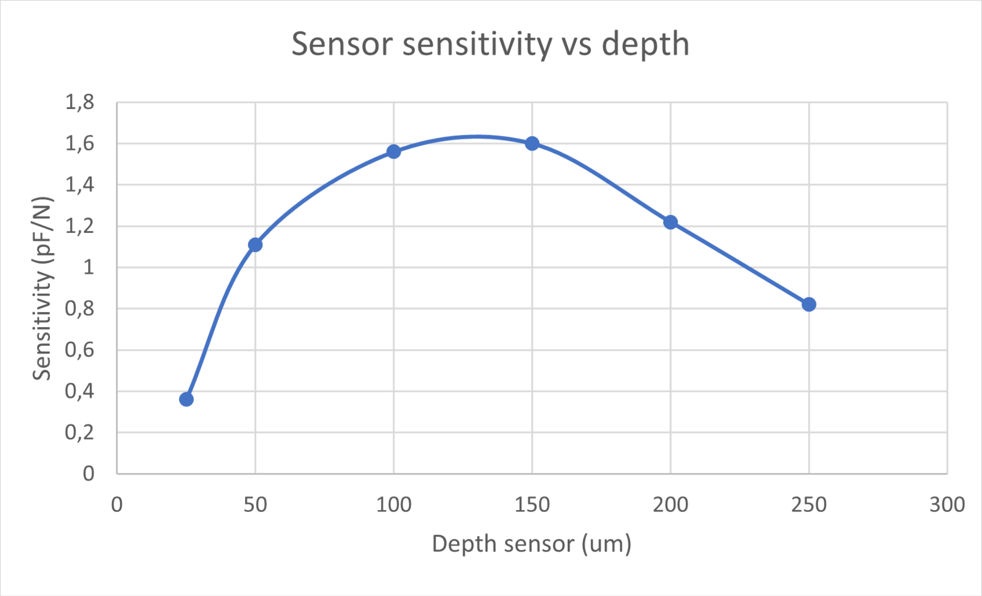

Figure 3.6: Sensitivity of the sensor at different depths.

These results show that the sensor has the highest sensitivity if it is positioned between 100-150 µm depth into the substrate. These results might appear counter-intuitive at first glance, especially considering that Figure 3.5 indicated that the largest vertical deformation occurs closer to the surface. Previous studies involving the straight pillar also pointed towards a higher sensor sensitivity closer to the surface. However, simulations revealed a significant difference in the location of the center of rotation between the two pillar designs, as depicted in Figure 3.7. This shifted center of rotation is attributed to the wider base of the tapered pillar, as simulations with a straight pillar that had the same width showed a similar position of the center of rotation. Due to the shifted center of rotation, there is also greater horizontal deformation closer to the surface.

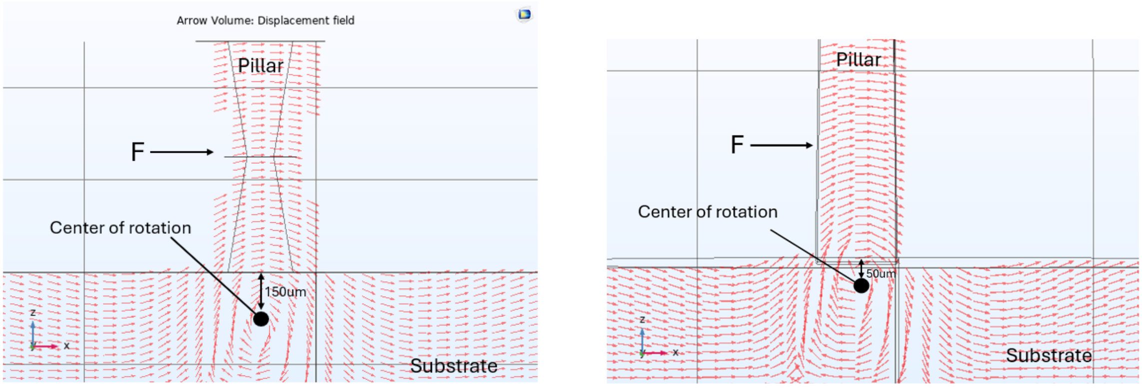

(a) (b)

Figure 3.7: Numerical analysis in Comsol of the substrate deformation for different pillars. a) Vector field of the substrate deformation with tapered pillars. b) Vector field of the substrate deformation with straight pillars.

This change in horizontal deformation becomes evident when observing the sensor's deformation, as shown in Figure 3.10. With the tapered pillar, the sensor's metal lines are compressed together due to the horizontal deformation (figure 3.8a, 3.8b), whereas with the straight pillar, which doesn't induce this horizontal deformation, the sensor lines are pushed apart (figure 3.8c, 3.8d). As found in the previous study, vertical displacement of the sensor changes the capacitance of the sensor by changing the distance between the metal lines. When a sinusoidal force is applied to the center of the pillar, this results in vertical deformation of the substrate, and the resulting change in capacitance can be simulated, as demonstrated in Figure 3.9b. However, horizontal displacement also changes the distance between the capacitor plates, and these two deformations seem to have opposing effects, as illustrated in Figure 3.10b. This could explain why the highest sensitivity is observed slightly deeper within the substrate, where the horizontal deformation is relatively smaller.

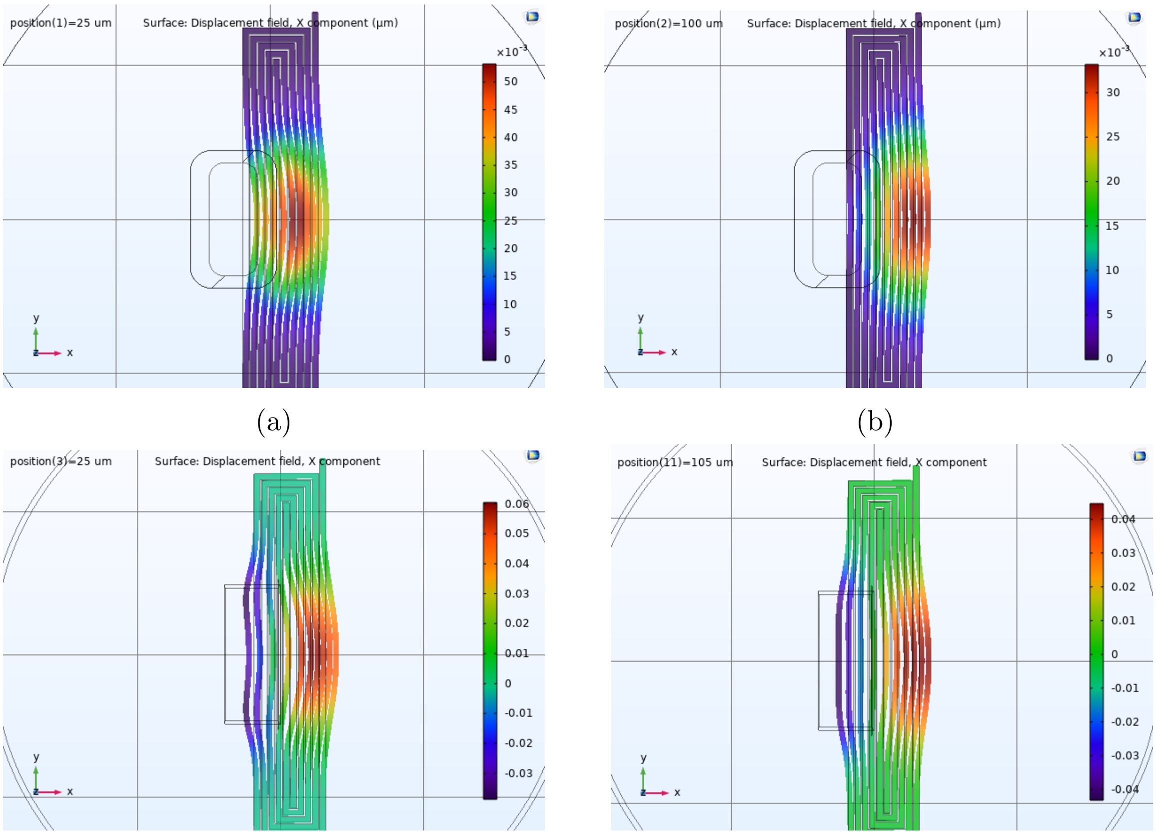

(a) (b)

(c) (d)

Figure 3.8: Analysis of the sensor deformation at 25 μm and 100 μm depth for different pillars. Color scale indicates displacement in x-direction only. All images use an equal scale factor to visualize the deformation. a) Deformation of sensor at 25μm depth with tapered pillar. b) Deformation of sensor at 100μm depth with tapered pillar. c) Deformation of sensor at 25μm depth with straight pillar. d) Deformation of sensor at 100μm depth with straight pillar.

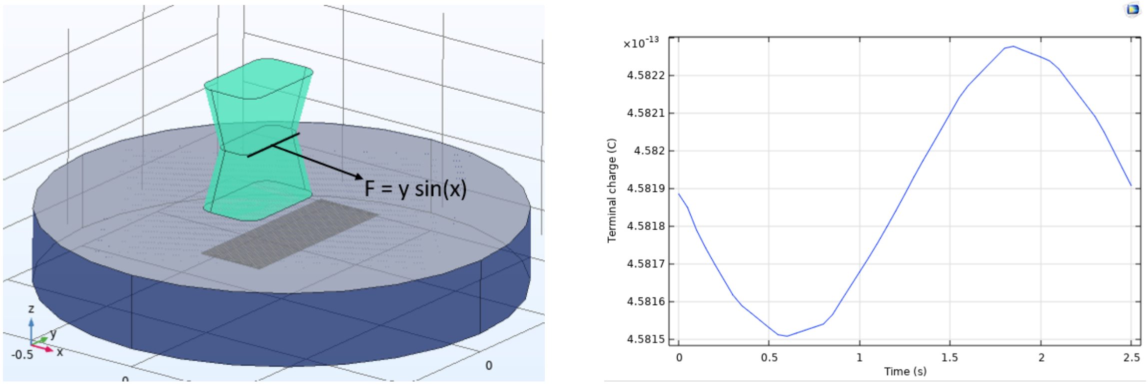

(a) (b)

Figure 3.9: Analysis of capacitance change due to pillar deformation a) Simulation set-up: sinusoidal force applied in the center of the pillar, and sensor positioned near the base of the pillar. b) The capacitance change due to the applied force.

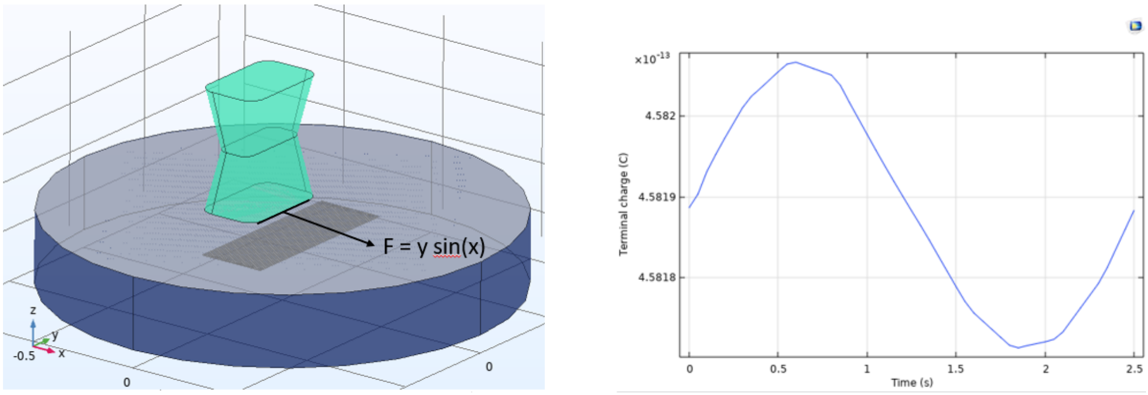

(a) (b)

Figure 3.10: Analysis of capacitance change due to pillar deformation a) Simulation set-up: sinusoidal force applied at the base of the pillar, and sensor positioned near the base of the pillar. b) The capacitance change due to the applied force.

### 3.3.2 Substrate thickness

After determining the optimal sensor position, the effect of changing the substrate thickness was further investigated. It was found that the substrate thickness significantly affects sensor deformation, and therefore sensitivity. The results for this analysis are depicted in Figure 3.11. The sensor position throughout the simulation was kept at 100µm depth, while the substrate thickness was variable (d). It was found that the thicker substrates allow for higher deformation of the sensor, as increasing the substrate thickness makes the substrate softer and easier to deform.

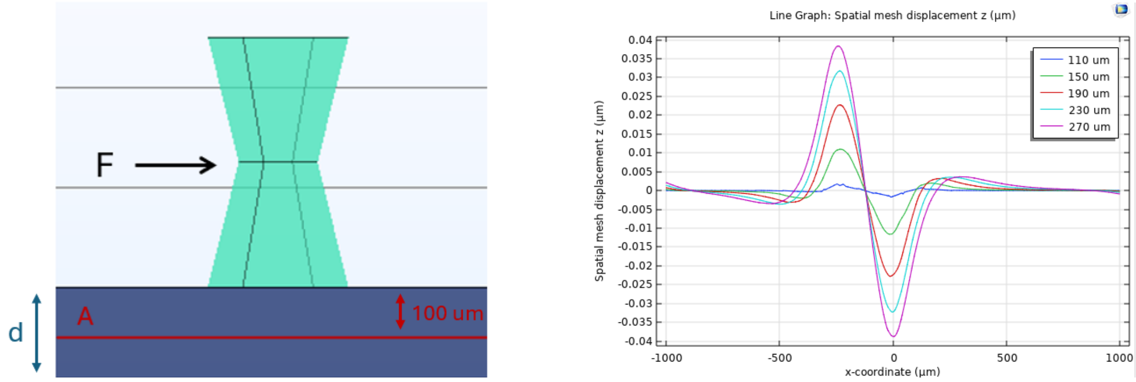

(a) (b)

Figure 3.11: Substrate displacement along line A for different substrate thicknesses (d) in supported configuration. a) Simulation set-up with applied force. b) Results for the displacement of line A for different substrate thicknesses (d).

### 3.3.3 Sensor geometry

In order to find the optimal geometry for the sensor, multiple designs were investigated, and assessed on sensitivity. Figure 3.12 depicts all the different designs that were investigated. Sensors a, b, and c are designs found in literature, that were found to have a high sensitivity for similar applications. Sensors d, e and f are additional suggested designs. All geometries aim to maximize the effective electrode length, as was found to be an important parameter for optimizing sensitivity (section 2). The dimensions for all sensors were kept the same. The sensor length was 800 µm, sensor width 235 µm, line width 15 µm and gap width 5 µm.

Although the difference with the spiral geometry (a) is small, the serpentine geometry (b) was found to be the best design for this specific sensor (Table 3). For additional shape optimization, the sensitivity for the serpentine geometry was investigated for different line widths and gap widths. These results are depicted in Figure 3.13. The figure demonstrates a distinct correlation between the gap and width of the metal lines and the sensor's sensitivity. Minimizing the gap width could thus enhance the sensitivity. The sensitivity is less influenced by the line width, and the ideal line width varies depending on the gap widths.

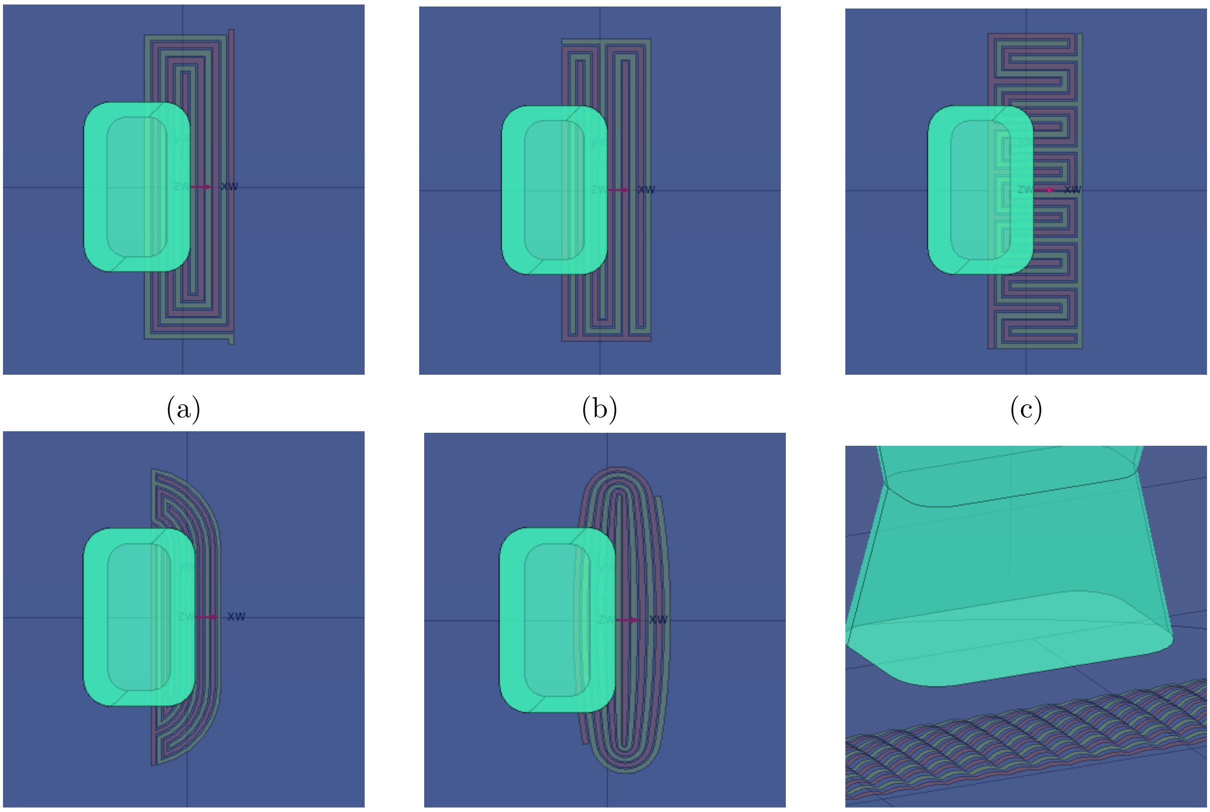

(a) (b) (c)

(d) (e) (f)

Figure 3.12: Different geometries that have been investigated a) Spiral sensor. b) Serpentine sensor. c) Serpentine sensor rotated 90°. d) Serpentine sensor with rounded edges. e) Spiral sensor with rounded edges. f) Serpentine sensor on wavy microstructured PDMS.

| Sensor type | a | b | c | d | e | f |
|---|---|---|---|---|---|---|
| Sensitivity (pF/N) | 1.45 | 1.56 | 0.67 | 1.21 | 1.1 | 0.75 |

Table 3: Comparison of the sensor sensitivity for different geometries.

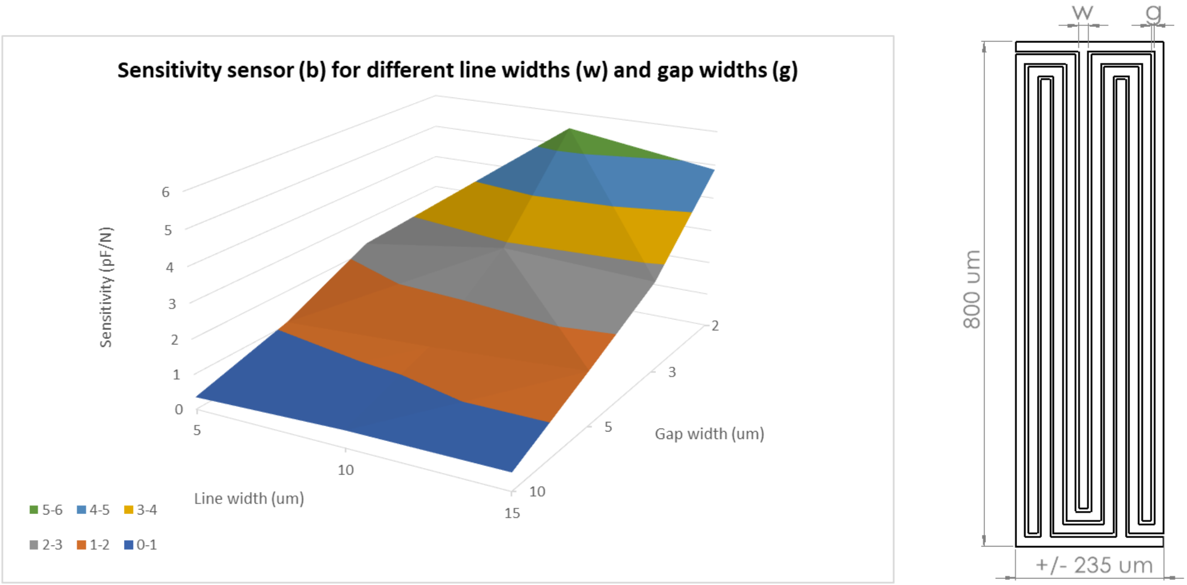

(a) (b)

Figure 3.13: a) Sensitivity of the serpentine sensor with different line and gap widths. The total width of the sensor was kept at approximately 235 μm by increasing or decreasing the number of lines. b) Sensor dimensions.

## 3.4 Suspended substrate

### 3.4.1 Sensor position

The effect of having a suspended substrate was also investigated. When the substrate is suspended, the full substrate is able to move down, with most deformation occurring in between both pillars, as indicated in Figure 3.14b. Since the deformation of the substrate beneath one pillar is now also affected by the force exerted on the other pillar, the computational model was no longer simplified to a single-pillar simulation.

Just as for the supported substrate, the vertical deformation of the substrate was examined along x, y, and z directions. For the supported substrate, the majority of the deformation occurred near the surface. However, in the suspended configuration, the entire substrate can move downward, resulting in a more uniform deformation across different depths, as shown in the Figure 3.15. Compared to the supported configuration, the area in which most of the deformation occurs is slightly larger in y-direction, and extends to the whole area in between both pillars in x-direction.

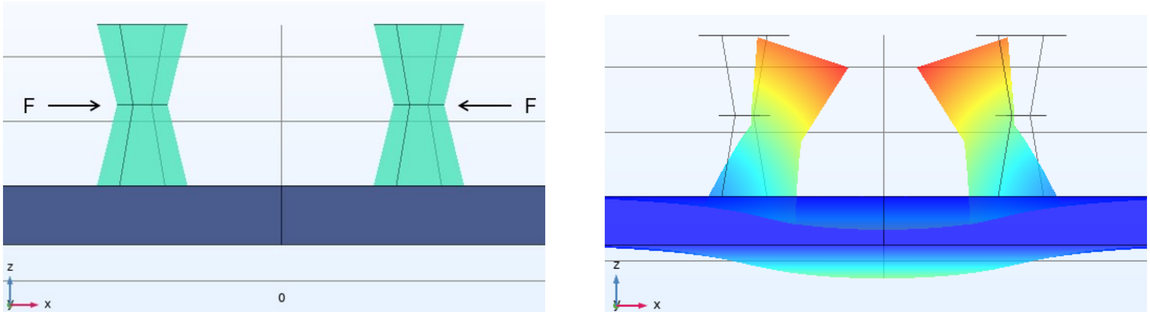

(a) (b)

Figure 3.14: Visual representation of substrate deformation in suspended configuration. a) Substrate and pillars before applying force. b) Simulated substrate deformation after applying force.

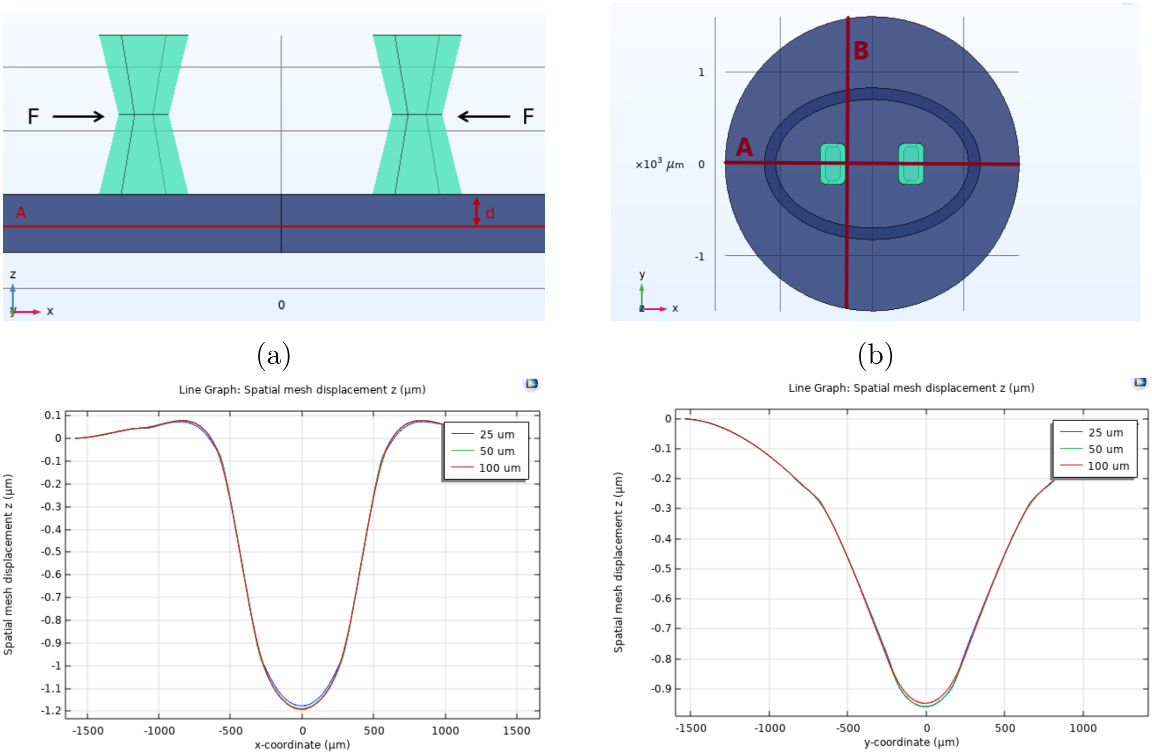

(a) (b)

(c) (d)

Figure 3.15: Analysis for optimal sensor position. a) Simulation set-up: force (50 µN) applied in the center of the pillars and the vertical displacement of the substrate is investigated along three different depths (d). b) The displacement is investigated along two different cross-sections of the plane, indicated with line A and line B. c) Results for the deformation of the substrate along line A. d) Results for the deformation of the substrate along line B.

### 3.4.2 Substrate thickness

While a thick, soft substrate resulted in larger deformations in the case of a supported substrate, the opposite was found to be true for a suspended substrate. The thinner the substrate, the larger the deformations, as it gets easier to bend. Bending is a type of deformation that is restricted for supported substrates, which explains the opposite results for the change in substrate thickness. The simulation results for the deformation for varying suspended substrate thicknesses are shown in Figure 3.16.

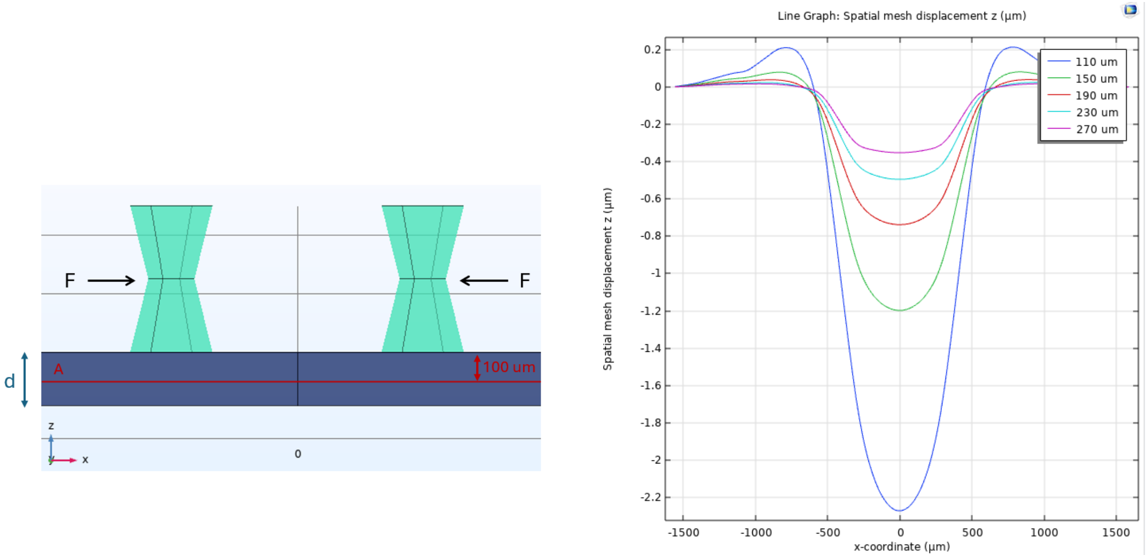

(a) (b)

Figure 3.16: Substrate displacement along line A for different substrate thicknesses (d) in suspended configuration. a) Simulation set-up with applied force. b) Results for the displacement of line A for different substrate thicknesses (d).

### 3.4.3 Sensor geometry

The sensor geometry that exhibited the highest sensitivity on a supported substrate, as illustrated in Figure 3.13b, was also evaluated on a suspended substrate. The chosen line width and gap width for this comparison were 15 µm and 5 µm respectively. The goal was to compare the sensitivity of the sensor in both the supported and suspended configurations. This was done for a range of substrate thicknesses, as a thicker substrate was shown to lead to greater deformations for a supported substrate, while a thinner substrate was shown to lead to greater deformations for a suspended substrate. Substrate thicknesses below 120 µm are likely not feasible with the current fabrication method, which is why this was set as the bottom limit for the comparison. The sensitivity was again determined through time-dependent studies using a sinusoidal force of 50µN. Then, the maximum change in capacitance was divided by the applied force, in accordance with formula 1. The results of this comparison are shown in Figure 3.17. As shown by the results, the choice for a supported or suspended substrate depends on the substrate thickness. The highest sensitivity can be achieved with a suspended substrate, as long as the thickness remains below approximately 160 µm.

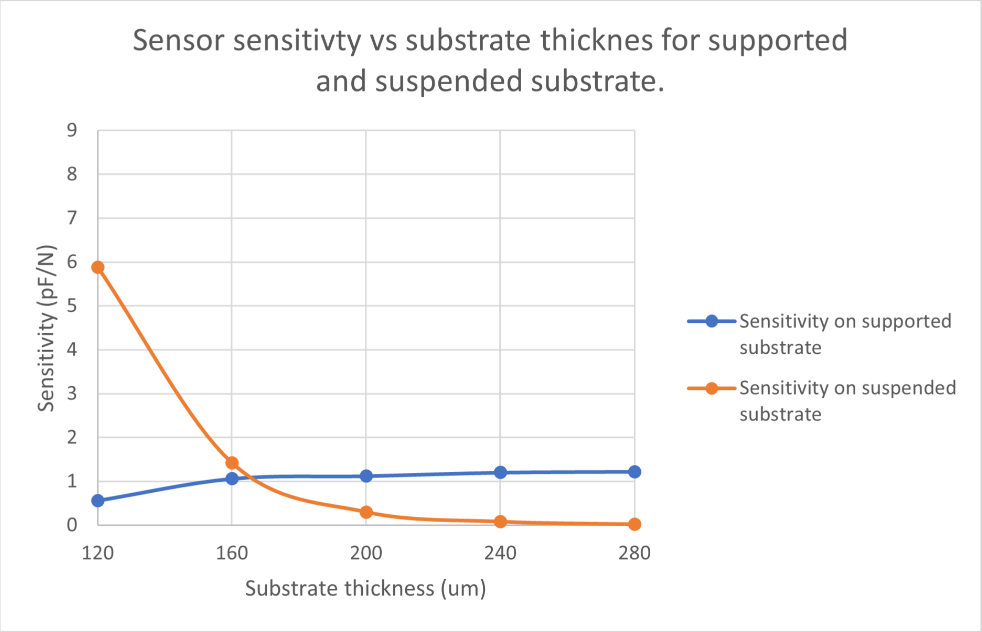

Figure 3.17: Sensitivity of the sensor (fixed at 100 µm depth) for different substrate thicknesses (d).

## 3.5 Conclusion

Numerical simulations were utilized to determine the optimal sensor position, substrate thickness, and sensor geometry. Furthermore, this was done for both a supported substrate, and a suspended substrate.

For a supported substrate, the optimal position of the sensor was identified in a region within 800 µm x 600 µm from the center of the pillar, at around 100 µm depth into the substrate. Given that the optimal depth is around 100 µm into the substrate, the noise due to the parasitic capacitance from the cell culture medium on top of the PDMS is expected to have a minimal effect, since the penetration depth of the electric field from the chosen sensor was shown to be approximately 30 µm (Figure 3.3). For optimal sensitivity, a thicker substrate would be recommended. Through comparative analysis of various sensor geometries, the serpentine design emerged as the most effective. Furthermore, a direct correlation was demonstrated between sensor sensitivity and the dimensions of line and gap widths. Optimal sensitivity was achieved with narrower gap widths, while the line width presented an optimal value that varied in relation to the gap width.

For a suspended substrate, the optimal position of the sensor extends to the whole area in between both pillars. The effect of the depth of the sensor on sensitivity still has to be investigated, although change in depth seems to be limited by the currently used fabrication method. For optimal sensitivity, the substrate should be as thin as possible.

In order to compare the supported and the suspended configuration, the sensitivity of one sensor design was simulated in both configurations. This sensor design included a serpentine geometry with a length of 800 µm, a width of 235 µm, a line width of 15 µm, and a gap width of 5 µm, as illustrated in Figure 3.13b. This design was selected for comparison because it demonstrated a high level of sensitivity while staying within safe limits of fabrication process accuracy. After comparing the sensitivity values of this design for both a supported substrate, and a suspended substrate (in Figure 3.17), it becomes evident that the sensor sensitivity for a suspended substrate is higher, as long as the substrate thickness is below approximately 160 µm.

# 4 Design

## 4.1 Design changes

Based on the literature research (Chapter 2) and the numerical simulations (Chapter 3), the previous design was updated. The redesign is illustrated in Figure 4.4. The redesign was specifically developed to address the main challenges outlined in Section 1.4. In summary, the following challenges were identified:

1. Optimization of sensor sensitivity is beneficial.
2. Challenges were encountered in achieving precise alignment between the pillars and sensors.
3. The interconnects demonstrated fragility during the fabrication process, particularly during the transfer to the printed circuit board (PCB) and during wire bonding.

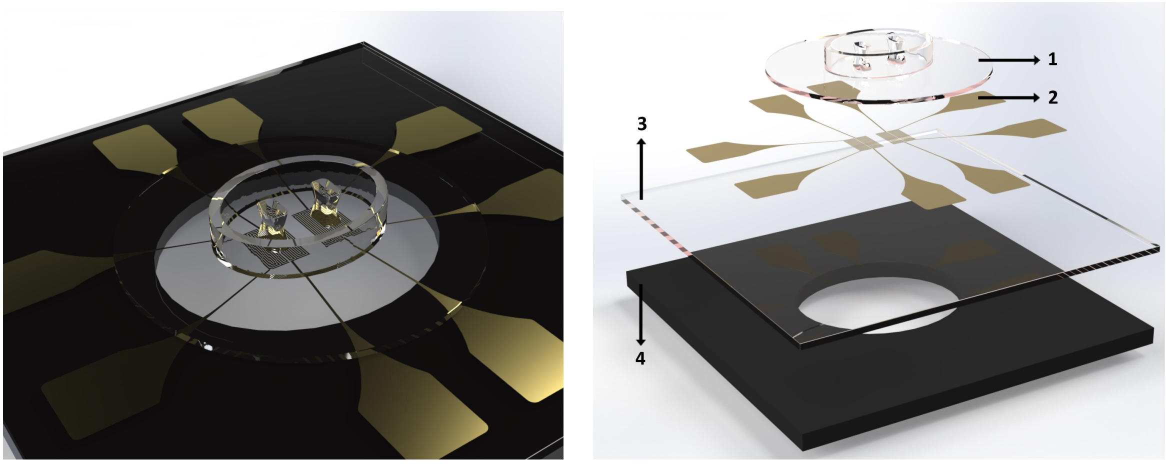

(a) (b)

Figure 4.1: Re-design of the capacitive sensors for the EHT platform. a) Assembled view of design. b) Exploded view of design, indicating each component: 1) PDMS pillars and microwell. 2) Aluminum sensors, interconnects, and bonding pads. 3) PDMS substrate. 4) Silicon base.

*Sensor sensitivity* is optimized by adopting a new sensor geometry. In Chapter 3, which described the numerical simulations and analysis, different geometries were evaluated, and it was shown that the serpentine geometry emerged as the most sensitive. For a comparison with the previous version of the capacitive sensor, two designs were selected for the fabrication: spiral, the previous design, and serpentine, the novel design with increased sensitivity. The precise dimensions are provided in the following subsection.

Further optimization of sensitivity can be achieved by selecting an optimal ratio between the line width and gap width, as was illustrated in Figure 3.13. Ideally, the gap width should be as small as possible for increased sensitivity, though fabrication processes impose limitations. Based on the fabrication experience with the previous sensor design, a gap width of 5 µm was determined to be the smallest achievable dimension. The new design includes two variations in line and gap width for each geometry, as shown in Table 4.

Furthermore, in Section 3.4.3 it was shown that sensor sensitivity would be the highest for a suspended substrate, where the substrate thickness would be as thin as possible. Sensitivity could therefore be optimized by creating a thin suspended membrane. To verify these results, the redesign includes two different substrate thicknesses, also indicated in Table 4.

*Sensor and pillar bonding* was performed manually, and it was therefore difficult to achieve precise and consistent alignment. Small changes in position of the sensor with respect to the pillars affects sensor sensitivity, and make measurements with different platforms incomparable. Therefore, alignment was investigated by using a die bonder. A die bonder can be used to accurately pick up components and place them onto a target location. By using this machine, alignment could be carried out with higher precision.

*Damaged interconnects* were seen during different parts of the process. Firstly, during transfer of the sensors from the wafer to the PCB, and secondly, during wirebonding. In order to address these challenges, the re-design aimed to provide mechanical support to the non-sensing part of the patterned sensor area. This is done by incorporating the silicon base, as indicated with number 2 in Figure 5.4b. The silicon base features a central opening that serves as an optical window, providing a transparent view of the platform. By making the chip that will be transferred to the PCB rigid instead of soft, transfer can be carried out safer, mitigating the risk of deforming the platform and cracking the interconnects. Additionally, the interconnects were re-designed with a tapered transition between the wide bonding pad and the thin interconnect, further reducing stress on the interconnects during wirebonding. Finally, in the new design, each die on the silicon wafer will be separated by dicing lines, allowing the wafer to be manually broken into individual dies. This eliminates the need for mechanical dicing, which could generate strong vibrations that may damage the sensors and the PDMS membrane.

## 4.2 Design specifications

The summary of the updated designs of both serpentine and spiral sensors, with two different metalization ratios are presented in Table 4. Each design was meant to be tested on a 20 µm and 80 µm thick substrate. The subsection then proceeds with a series of drawings depicting the general parts of the design, such as interconnects and bonding pads, that remain the same across all sensor designs. Drawings of the pillars and microwell were not included as the dimensions were left unchanged, and can be found in [3].

| | Geometry | Line / Gap width µm |
|---|---|---|
| Sensor 1 | Spiral | 10/5 |
| Sensor 2 | Spiral | 20/10 |
| Sensor 3 | Serpentine | 10/5 |
| Sensor 4 | Serpentine | 20/10 |

Table 4: Sensor designs

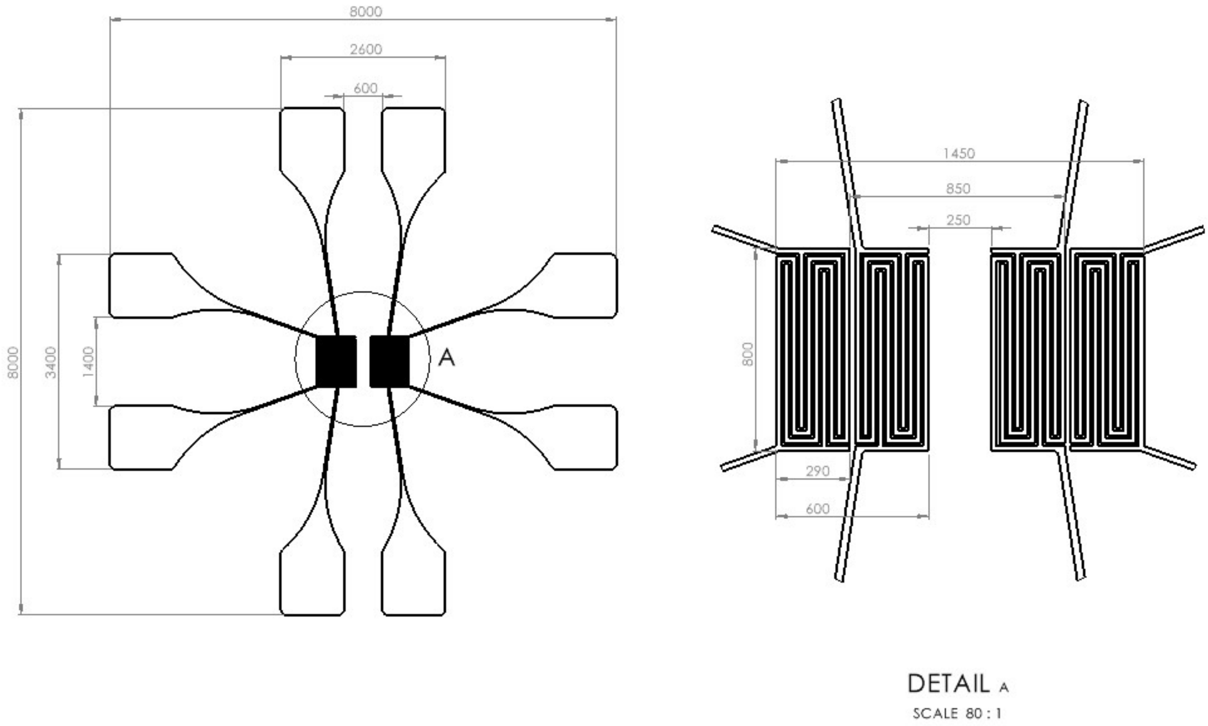

Figure 4.2: Drawing serpentine sensors, interconnects, and bonding pads (component 2 in Figure 5.4b). Units are in micron.

.

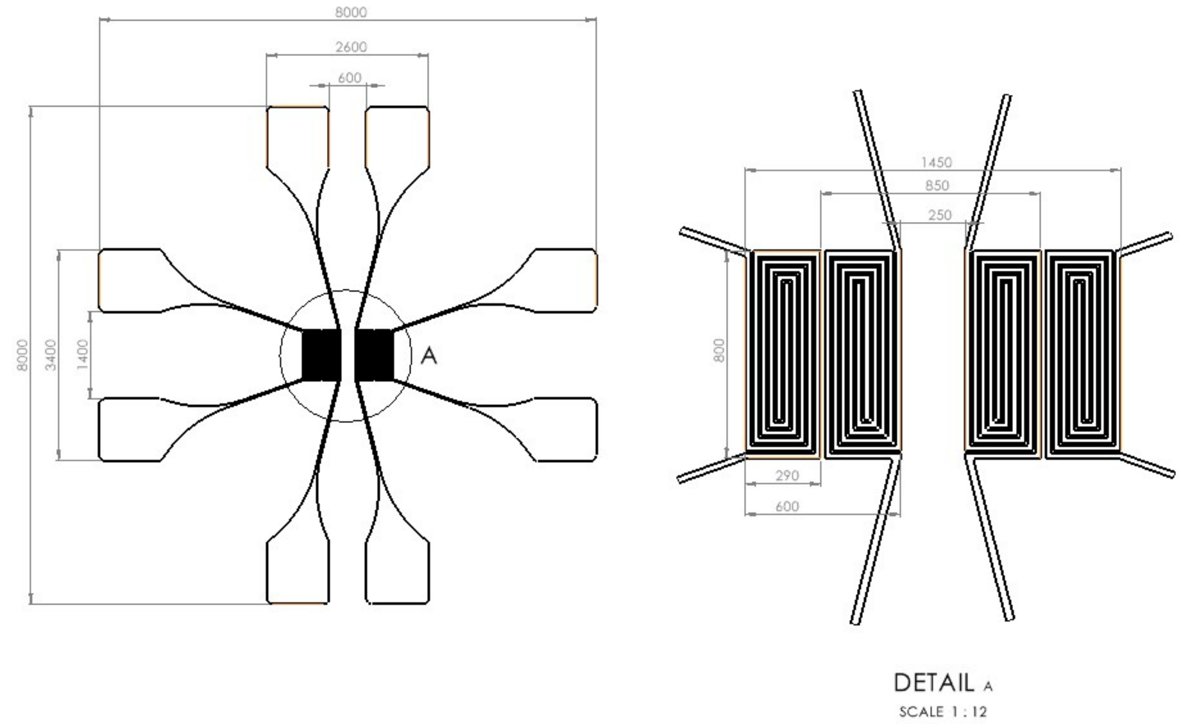

Figure 4.3: Drawing spiral sensors, interconnects, and bonding pads (component 2 in Figure 5.4b). Units are in micron.

.

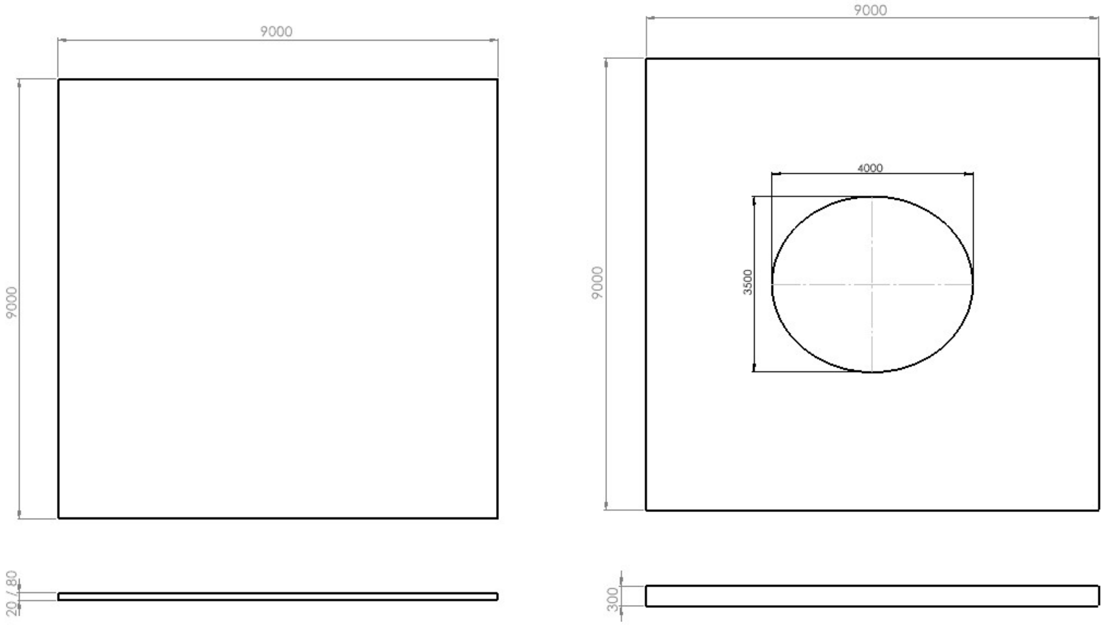

(a) (b)

Figure 4.4: a) Drawing PDMS substrate (component 3 in Figure 5.4b). b) Drawing silicon base (component 4 in Figure 5.4b). Units are in micron.

# 5 Fabrication

## 5.1 Microfabrication techniques

The EHT platform was fabricated using a combination of standard micromachining techniques and polymer processing in a cleanroom environment. Some of the techniques used during fabrication are spin-coating, photolithography, plasma-enhanced chemical vapour deposition (PECVD), reactive ion etching (RIE), deep reactive ion etching (DRIE), and wirebonding. The mentioned techniques are explained below.

### Spin-coating

Spin-coating involves the application of a thin liquid film onto a flat substrate by rotating the substrate at high speeds. The spin-coating process typically begins by placing a small amount of liquid, known as the coating material or photoresist, onto the center of the substrate. The substrate is then rapidly rotated, causing the liquid to spread out due to centrifugal forces. As the rotation continues, the excess liquid is driven off the edges of the substrate, leaving behind a uniform, thin film across its surface. The speed at which the substrate is spun and the duration of spinning are carefully controlled to achieve the desired film thickness. Factors such as the viscosity of the liquid, the concentration of the coating material, and the spinning parameters influence the final film characteristics.

### Photolithography

Photolithography is a technique that involves transferring a pattern from a photomask onto a photosensitive layer, and subsequently on a silicon wafer or other substrate, to create intricate microscopic structures. The process starts with a clean silicon wafer coated with a light-sensitive material called a photoresist. The photoresist is exposed to ultraviolet light through a photomask, which contains the desired pattern. The mask acts as a stencil, allowing light to pass through only specific areas. When the light hits the photoresist, a chemical reaction occurs, altering the resist's properties. There are typically two types of photoresists used: positive and negative. Positive photoresists become soluble in a developing solution where they are exposed to light, while negative photoresists become insoluble in the exposed areas. After exposure, the wafer is developed, removing the soluble areas, leaving behind the desired pattern. The patterned resist acts as a mask for subsequent processes such as etching or deposition.

### Plasma enhanced chemical vapor deposition (PECVD)

PECVD involves the deposition of thin films onto a substrate by introducing a precursor gas into a vacuum chamber. The precursor gas is excited and dissociated into reactive species using a plasma discharge. The plasma is generated by applying a radio frequency or microwave power source to the gas, creating a high-energy environment. The reactive species produced in the plasma react with the substrate surface, resulting in the deposition of a thin film. The film growth occurs through a combination of chemical reactions and physical processes such as condensation and surface diffusion. The properties of the deposited film, such as composition, thickness, and morphology, can be controlled by adjusting various process parameters, including gas composition, pressure, temperature, and power input.

**Reactive ion etching (RIE)**

RIE is a dry etching process that involves the removal of material from a substrate using reactive ions. In RIE, a plasma is generated by applying radio frequency power to a gas mixture in a vacuum chamber. The gas mixture typically consists of a reactive gas and an inert gas. The reactive gas chemically reacts with the material to be etched, while the inert gas helps to maintain a stable plasma and control the ion energy. The reactive ions from the plasma bombard the surface of the substrate, physically sputtering and chemically reacting with the material. The selectivity of the process can be controlled by adjusting the gas mixture and process parameters. This allows precise etching of specific materials while minimizing damage to surrounding areas.

**Deep reactive ion etching (DRIE)**

Unlike traditional RIE, which typically produces etch depths on the order of micrometers, DRIE is capable of etching features that are several tens or even hundreds of micrometers deep. This makes it particularly suitable for creating deep trenches, cavities, and through-holes in substrates. DRIE achieves its high-aspect-ratio capabilities through a combination of etching and passivation steps. The process begins with the formation of a passivation layer on the sidewalls of the etched features. This layer protects the sidewalls from further etching, allowing the etching process to proceed vertically instead of laterally. The passivation layer is periodically removed to expose fresh material for etching, and the cycle is repeated until the desired depth is achieved.

**Wirebonding**

Wirebonding is a common technique used to establish electrical connections between micro-devices and their respective packages, which may be a printed circuit board (PCB), ceramic package, or other material. It involves the process of bonding tiny wires, usually made of gold or aluminum, between the device's contact pads and the corresponding terminals on the package. The wirebonding process typically begins with the placement of the device onto the package. Next, a specialized wirebonding machine is used to form the wire connections. The machine holds a spool of wire and employs a combination of heat, pressure, and ultrasonic energy to create a solid bond between the wire and the contact pads of the device and the package.

## 5.2 Process flow

The microfabrication process is divided in two parts, using two 4-inch silicon wafers. The first wafer is used to fabricate metal sensors on top of a PDMS substrate, while the second wafer is used for fabrication of the molds for the PDMS pillars and microwells. Finally, the two processes are combined by bonding the molded PDMS pillars and microwell on top of the sensors. The process flow of the silicon mold for pillar fabrication is adopted from [3], and will not be further discussed in this chapter.

The fabrication flowchart of the sensors is depicted in Figure 5.1. The fabrication process of the sensors uses 300 µm-thick double-side polished silicon wafers. First, PECVD

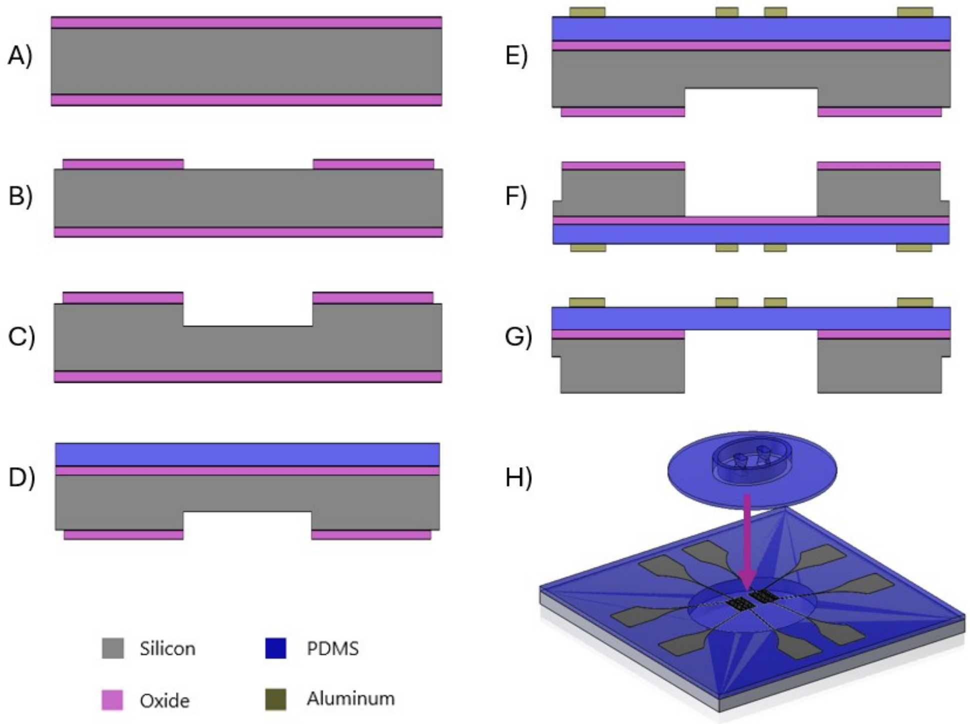

Figure 5.1: Fabrication flowchart cross-sections.

$SiO_2$ was deposited on both sides of the wafer (Figure 5.1A). On the frontside, a 2 μm-thick layer as landing layer for DRIE, and 4 μm on the backside as masking layer for DRIE. The masking layer was patterned using 3 μm-thick negative photoresist and unprotected areas were dry etched in $CHF_3$ and $C_2F_6$ plasma (Figure 5.1B). The etched region includes the optical window and additional dicing lines that were included to manually break the wafer into single dies at the end of the fabrication. Next, a new layer of negative photoresist was deposited and patterned on the backside of the wafer that included only the optical window. This second layer was used as masking layer for DRIE, during which 150 μm-deep cavities were etched for the optical window (Figure 5.1C). Next, a 20 μm thick layer of PDMS (Sylgard 184, curing agent ratio of 10:1) was spin-coated on the frontside of the silicon wafer, after which the PDMS was cured at 90 °C for 60 minutes (Figure 5.1D). Prior to aluminum sputtering, the wafer was exposed to oxygen plasma (75 W for 1 min) to activate the PDMS surface and enhance adhesion between the aluminum and PDMS. Additionally, a leak-up rate test was done to ensure that the gas leakage from the PDMS was within a specified range that is required by the sputtering conditions. The aluminum layer was then sputtered on top of the PDMS (at 25 °C and a power of 1 kW) in 4 steps of 250nm, with 3 minutes of degassing in between each step. In the following steps, the sensors were patterned using a 3 μm-thick negative photoresist as mask and dry etched in Cl and HBr plasma (Figure 5.1E). Four different sensor designs were created in four different wafer quadrants. Spin-coating, baking, and development was performed manually to prevent contamination with PDMS. The wafers were baked at a lower temperature (90 °C) to prevent cracking of the aluminum due to thermal expansion of the PDMS. Prior to DRIE, to complete the etch of the optical window and the dicing lines, the remaining negative photoresist from the previous step, still on top of the sensors, was removed by immersing the wafer in NI555 (18 hours). The wafer was then mounted on a carrier wafer that had sputtered layers of aluminum on both sides for better heat conduction, and thus cooling, during DRIE. Additionally, a thermal oil was used as bonding agent between both wafers. DRIE was performed in steps of 50 cycles, followed by a break of 3 minutes to cooldown, in order to prevent heating of the PDMS (Figure 5.1F). This step-wise etching was done out of precaution; the heating of the PDMS during DRIE was not further investigated. After DRIE, the carrier wafer was carefully removed by dissolving the thermal oil in IPA. Next, the oxide layer was dissolved in BHF (Figure 5.1G). Prior to immersing the wafer in BHF, the sensors were protected with a layer of positive photoresist to prevent the BHF from attacking the sensors, since BHF also attacks aluminum. After the oxide was removed, the wafer was rinsed in water to wash away the residual BHF. Next, the remaining photoresist that was still on top of the sensors was dissolved by immersing the wafer in acetone (5 min) and IPA (5 min). Finally, the wafer was broken in single dies by pressing lightly on the dicing lines that were created by DRIE. The final integration of the pillars and microwell on top of the sensors was done by distributing a very thin layer of uncured PDMS with a cotton swap on the bottom-side of the molded substrate with the pillars. Then, the pillars and sensors were aligned and bonded by using a T-3000-pro die bonder. After bonding, the assembled EHT platform was directly put in the oven for 1 hour at 90 °C to cure the PDMS that was used as bonding agent (Figure 5.1H). Some pictures that were taken after several steps of the fabrication are shown below in Figure 5.2 and 5.3. The more detailed flowchart that was used during fabrication is included at the end of this document.

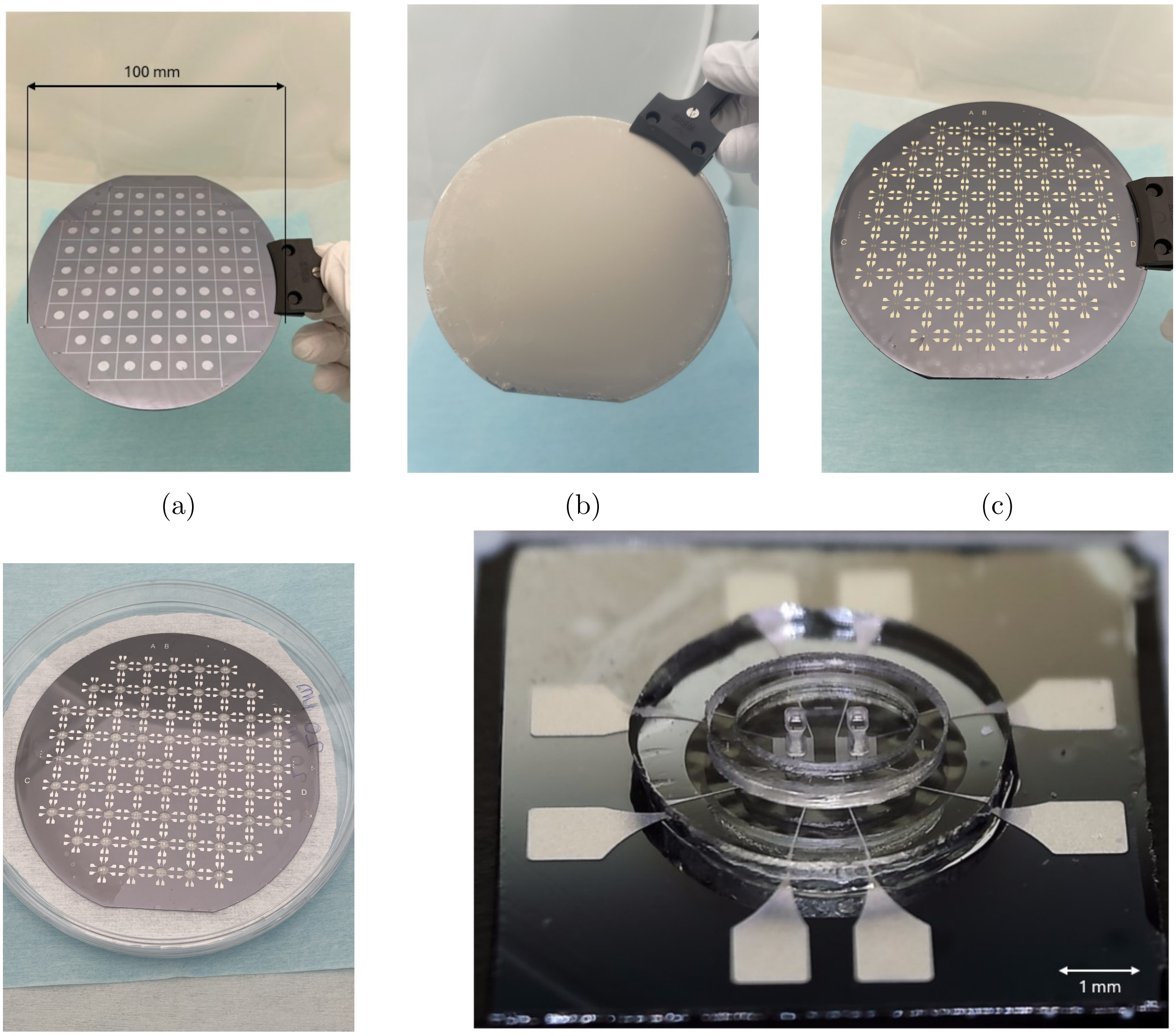

(a) (b) (c)

(d) (e)

Figure 5.2: Pictures from different steps of fabrication. a) Step B in flowchart (Figure 5.1): patterned oxide on the backside of the wafer with dicing lines and optical window. b) Step E in flowchart: sputtered aluminum on PDMS. c) Step E in flowchart: patterned sensors, interconnects and bonding pads. d) Step G in flowchart: etched wafer after DRIE. e) Step H in flowchart: pillars bonded on top of the sensors.

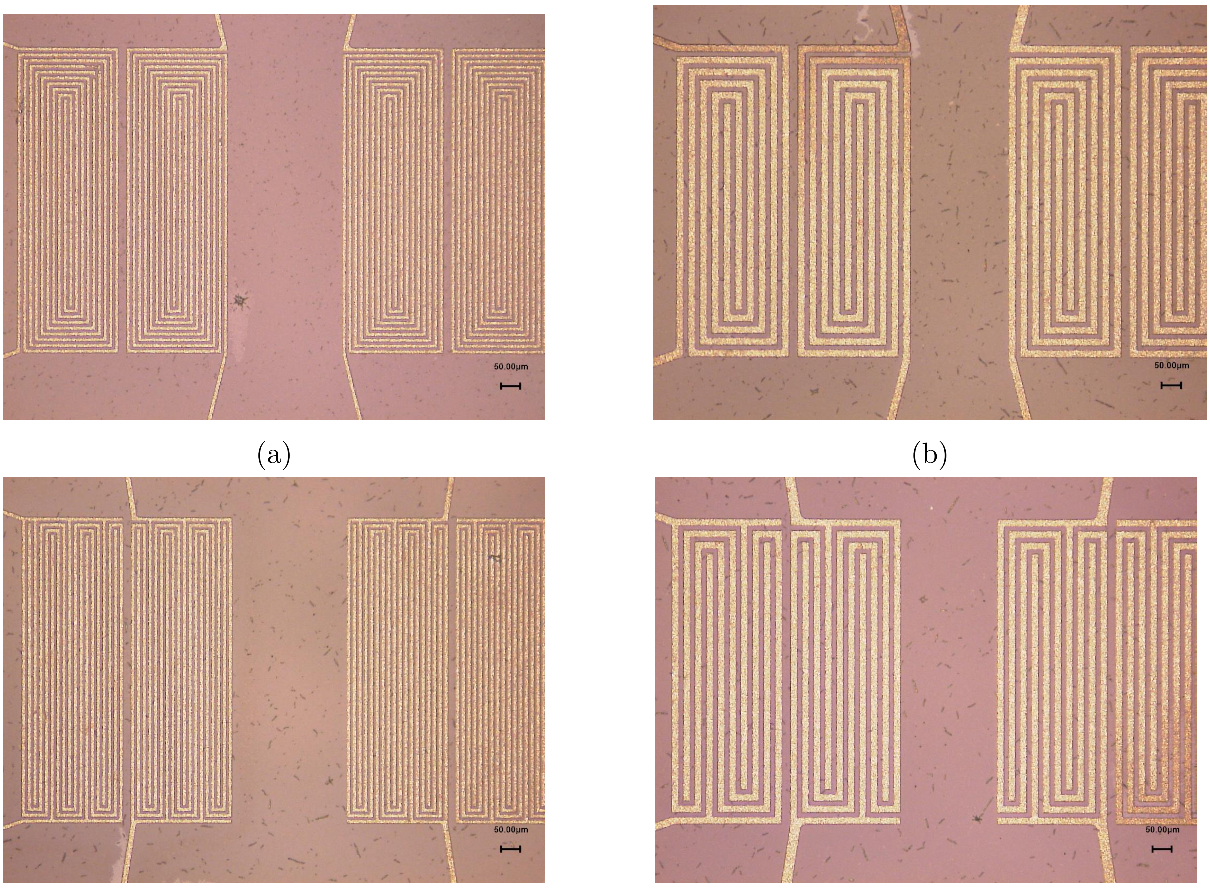

(a) (b) (c) (d)

Figure 5.3: Close-up images of each sensor type. a) Sensor 1 from table 4. b) Sensor 2 from table 4. c) Sensor 3 from table 4. d) Sensor 4 from table 4. Photoresist residues are visible on top of the sensors.

## 5.3 Critical steps

### DRIE

In order to etch the wafer from the backside, the frontside of the wafer, that already includes the sensors at this stage, has to rest on the chuck of the machine. This creates the risk of scratching the sensors during the process. In order to minimize this risk, a carrier wafer was used with a few droplets of thermal oil in between both wafers. This created enough spacing in between both wafers to minimize scratching. Nevertheless, the risk of scratching still exists and handling the wafer must be done very carefully. Furthermore, before performing DRIE, the photoresist that was still remaining on the sensors from the previous step had to be removed. Although the photoresist was initially left as an extra protective layer, it was found that during DRIE, the high temperatures caused the photoresist to burn, making it very difficult to remove later. To reduce heat generated during the process, the carrier wafer was coated with aluminum on both sides, and DRIE was conducted in cycles of 50 loops. Despite these precautions, the photoresist still burned, which is why it needs to be removed.

#### Oxide removal

Once the oxide is removed, the PDMS loses its support and becomes a delicate membrane. At this stage, handling the wafer requires extreme care, as it still needs to be submerged in BHF, acetone, and IPA. Placing the wafer into these chemical baths can exert enough stress on the membranes to cause deformation and cracks in the sensors. To prevent this, it is crucial to position the membranes orthogonally to the surface of the liquid and slowly submerge and remove the wafer from the chemical bath. When this is done carefully, these steps can be performed without damaging the sensors. When the dicing lines are etched too deep however, the wafer becomes very fragile and can break into multiple pieces when handling the wafer during these steps. Therefore, an etch depth of 150 µm is recommended in step C in the flowchart (Figure 5.1).

## 5.4 Other attempts

In addition to the design mentioned above, two other iterations of this design that included a polyimide (PI) support layer underneath the aluminum tracks were also investigated. As discussed in the literature review (Chapter 2), PI can serve as a stress buffer due to its higher stiffness compared to PDMS. However, increased stiffness can negatively impact sensitivity. Therefore, two designs were created to minimize the added stiffness from the PI, while still offering support for the aluminum. In one design, PI was used only beneath the bonding pads and partially along the interconnects, leaving the sensors flexible. In the other design, the PI was patterned using the same mask as the sensors, providing full support to the sensors, while keeping the regions in between the metal lines flexible. Both designs are discussed below.

### 5.4.1 PI support layer underneath the bonding pads

The design where PI is included as additional layer underneath the bonding pads and partially along the interconnects is shown in Figure 5.4. The primary goal of this design was to provide additional support during wirebonding, as this was a failure point in the previous design. The process flow remains mostly the same, except for the additional PI layer between step D and E in the original flowchart (Figure 5.1). The PI was spin-coated on top of the PDMS substrate with 8000 rpm, resulting in a 2 µm layer of PI. Prior to spin-coating, the PDMS was exposed to oxygen plasma (75W for 1 min) to activate the PDMS surface and enhance adhesion between the PDMS and PI. After spin-coating, the PI was soft-baked on a hotplate (100 °C for 2 min), exposed to UV light (160mJ/cm$^2$), and baked again (100 °C for 2 min). The PI was then patterned using HTRD2 developer for 90 seconds, followed by 90 seconds in RER600 to end the development reaction. Finally, the PI was cured inside a conveyor oven using the recipe from Table 5. This final curing step is important to evaporate all solvent residues and determine the final thickness of the PI layer, which reduced to 1 µm.

| T (°C) | 20 | 108 | 150 | 30 |
|---|---|---|---|---|
| t (min) | 40 | 50 | 120 | 60 |

Table 5: Curing recipe for polyimide.

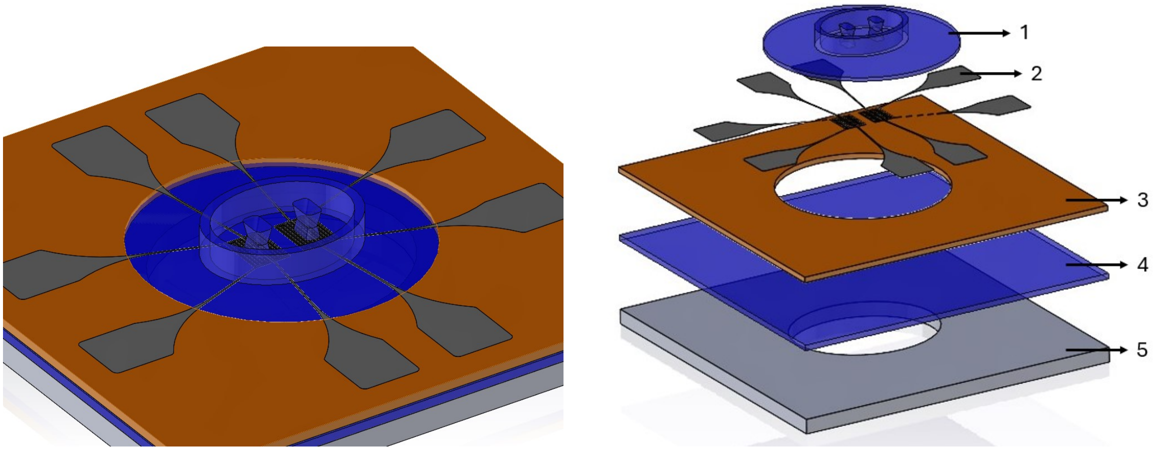

(a) (b)

Figure 5.4: Design iteration 1: a) Assembled view of design. b) Exploded view of design, indicating each component: 1) PDMS pillars and microwell. 2) Aluminum sensors, interconnects, and bonding pads. 3) Polyimide support layer. 4) PDMS substrate. 5) Silicon base.

After the PI was patterned and cured, the process continued following the same steps as the original design (Figure 5.1). However, the results were unsuccessful as the sputtered aluminum showed to crack right at the boundary between the PDMS and PI, as shown in Figure 5.5. This issue likely arises from the increased height of the PI layer, which the aluminum must bridge. To address this, reducing the PI thickness as much as possible is crucial; however, a thickness below 1 µm was not achieved. Alternative solutions could involve increasing the aluminum layer's thickness to more effectively bridge a 1 µm step height or optimizing the sputtering parameters to minimize thermal stress, which ultimately leads to cracking. These alternatives, however, were not further explored. This picture also clearly shows the different results between sputtered aluminum on PDMS and PI. On PDMS, the aluminum shows noticeable wrinkling, caused by the thermal expansion of the PDMS during sputtering and its subsequent shrinkage as it cools down. In contrast, the sputtered aluminum on PI remains smooth and flat, as PI experiences much less thermal expansion.

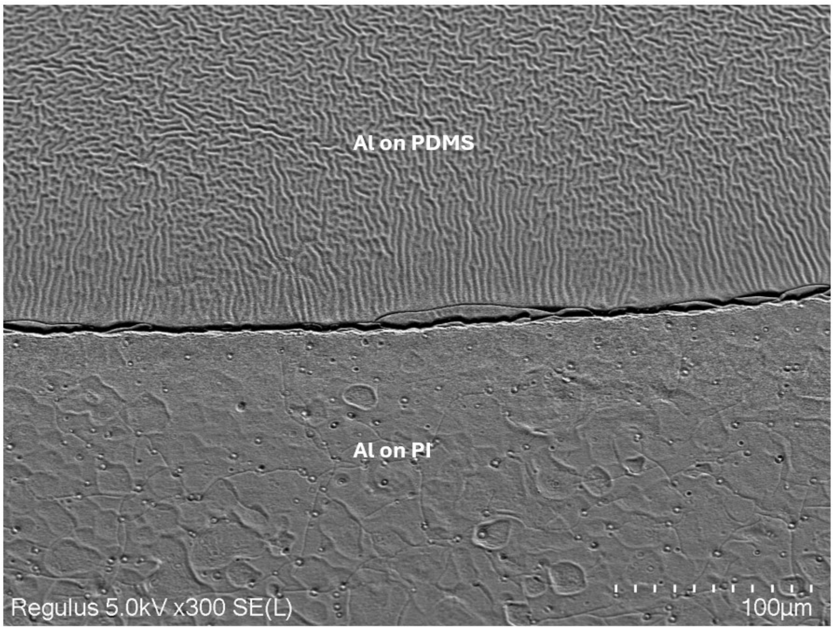

Figure 5.5: SEM image of sputtered aluminum on top of PDMS and PI.

### 5.4.2 PI support layer with the same pattern as the sensors

The design that fully supports the sensors with PI is shown in Figure 5.6. All fabrication steps remained the same as in the first PI design, except for the modified mask used during exposure. With complete PI support, this design likely offers the highest robustness. Fabrication was successful, and close-up images of each sensor are provided in Figure 5.7.

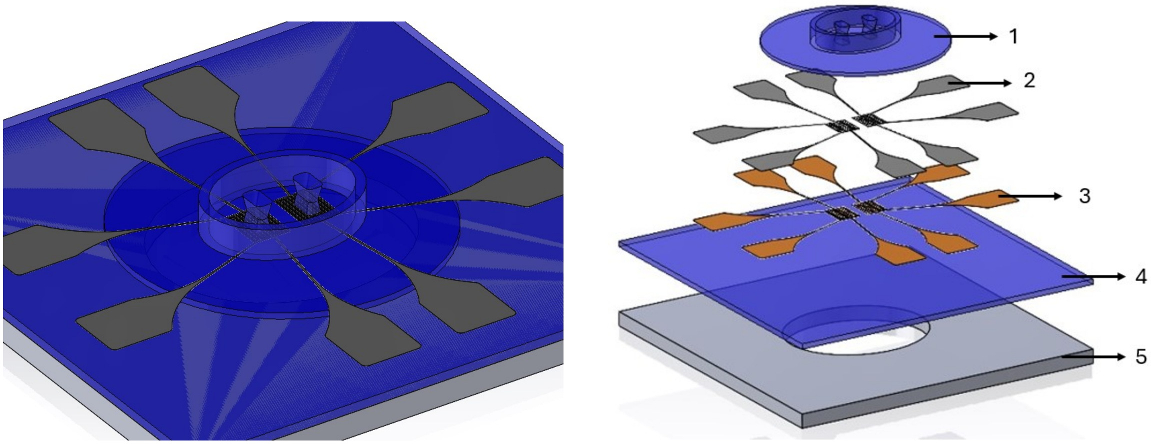

(a) (b)

Figure 5.6: Design iteration 2: a) Assembled view of design. b) Exploded view of design, indicating each component: 1) PDMS pillars and microwell. 2) Aluminum sensors, interconnects, and bonding pads. 3) Polyimide support layer. 4) PDMS substrate. 5) Silicon base.

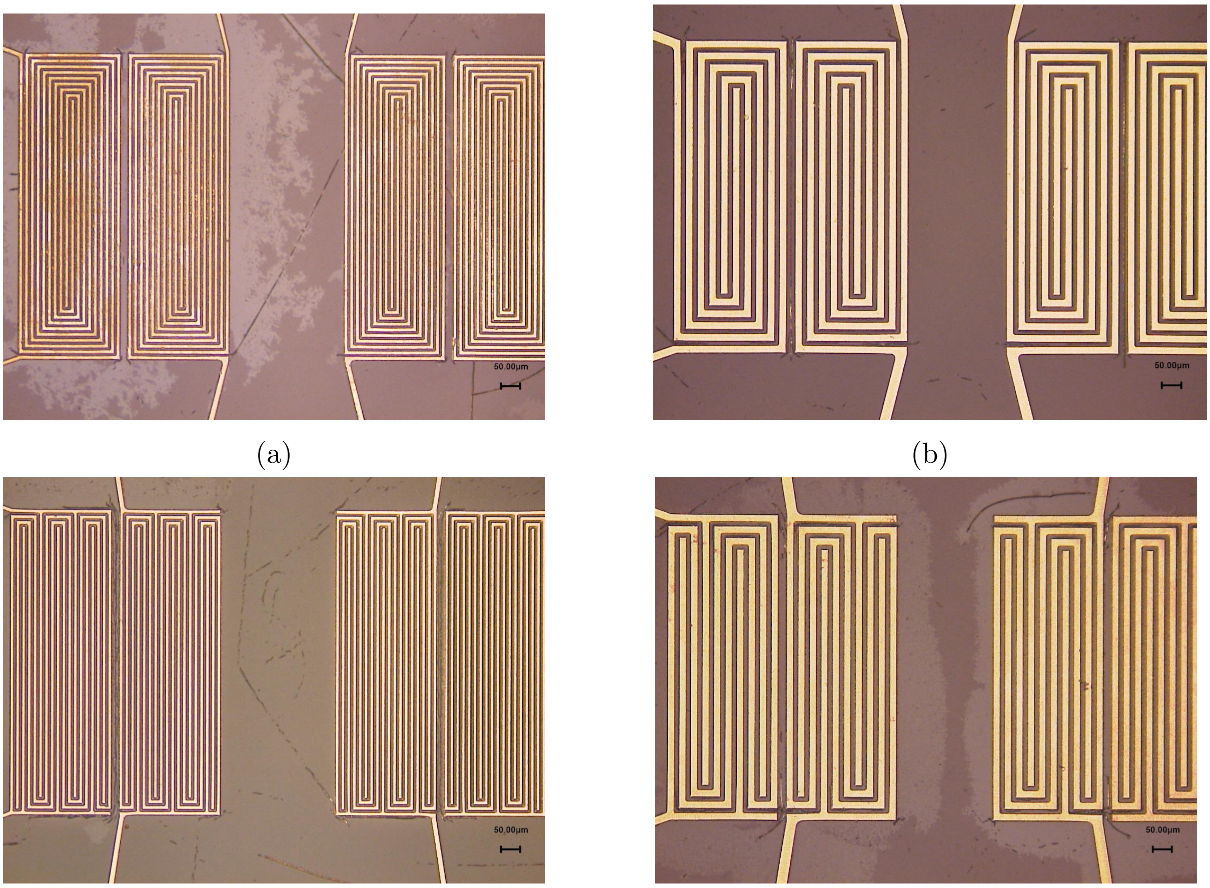

(a) (b) (c) (d)

Figure 5.7: Close-up images of each sensor type on PI. a) Sensor 1 from Table 4. b) Sensor 2 from Table 4. c) Sensor 3 from Table 4. d) Sensor 4 from Table 4.

While the robustness of the design including PI support layer is expected to be higher, sensitivity is expected to be a bit lower due to the higher stiffness of PI. For comparison, the graph in Section 3.17 that compared the sensitivity with the substrate thickness was updated, including the design with PI support layer for the suspended configuration. This is shown in Figure 5.8.

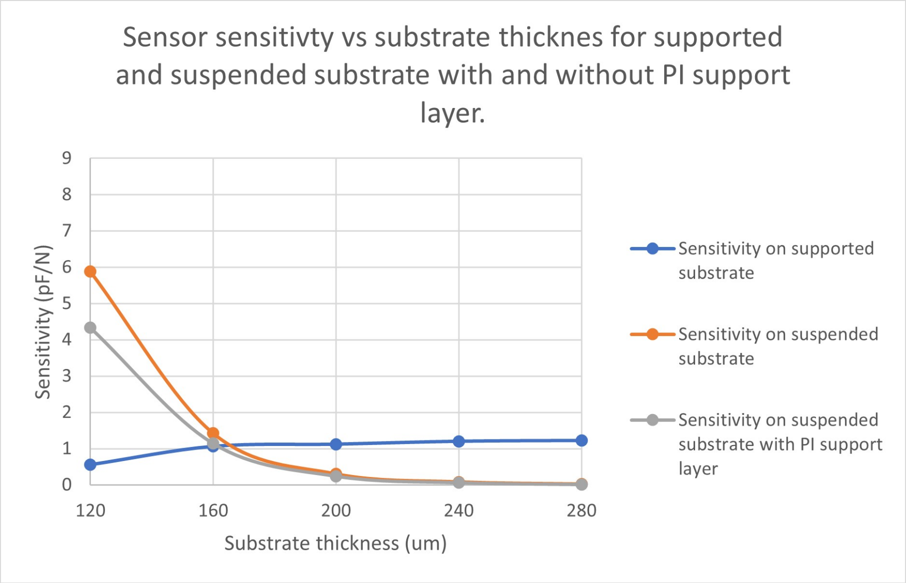

Figure 5.8: Updated graph from Section 3.4.3, including PI support layer.

# 6 Electrical characterization

## 6.1 Assembly of the measurement setup

For electrical characterization of the sensors, the EHT platforms were glued and wirebonded to a custom made PCB, specifically designed to allow connection of the individual sensors to a readout system (AD7745). The PCB design and the used readout system were adopted from [3]. Aluminum wirebonds were made from the contact pads on the EHT platform to the corresponding bonding pads on the PCB, using the parameters listed in Table 6. Wirebonds were then insulated by distributing PDMS (Sylgard 184, curing agent ratio of 10:1) on top of the wirebonds to minimize parasitic capacitance, as shown in Figure 6.1. Distribution of PDMS was done manually by using a syringe that allowed for deposition of small droplets on top of the wirebonds.

| | Ultrasonic power (mW) | Time (ms) | Force (mN) |
|---|---|---|---|
| Bond 1 (EHT platform) | 400 | 750 | 365 |
| Bond 2 (PCB) | 350 | 300 | 350 |

Table 6: Wirebond parameters.

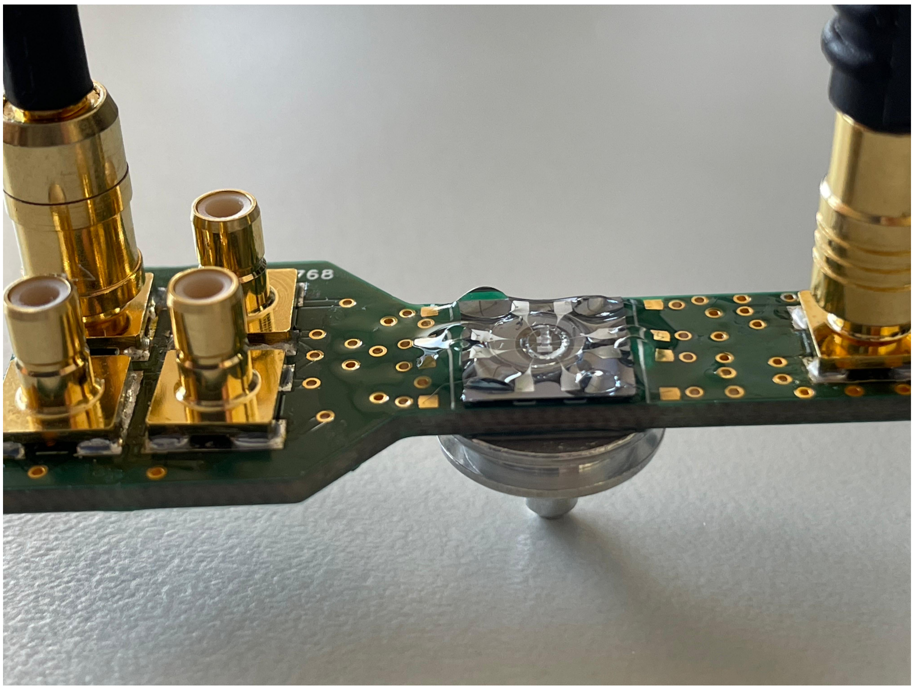

Figure 6.1: EHT platform glued and wirebonded to custom PCB. Wirebonds were insulated with a UV-curable resin.

## 6.2 Static measurements

The electrical characterization of the sensors includes measurements of their output in both static and dynamic conditions. For static assessment, the base capacitance of the fabricated sensors was measured and compared to simulation estimates. Measurements were conducted at wafer scale using an E4980A Keysight LCR meter. This device was connected to a Cascade Microtech Summit 12k electromagnetically shielded probe station equipped with four independent sensing probes. The probes established electrical contact with aluminum bonding pads patterned on the PDMS substrate. Capacitance-voltage (C-V) measurements were carried out with a 1V bias voltage and an excitation signal frequency of 32 kHz, matching the excitation frequency of the AD7746 board, that is later used for dynamic measurements. The static measurements were conducted both before and after assembly (as described in Section 6.1), to evaluate the sensor yield through the assembly process, which was a critical challenge in the previous sensor design, as discussed in Chapter 1.4.

### 6.2.1 Base capacitance before assembly

The measurements of the base capacitance before assembly were executed on wafer-scale. Therefore, the sensors were not yet fully encapsulated with PDMS, and the expected capacitance is smaller than the values obtained from the measurements after assembly. This is due to the lower di-electric permittivity of air compared to PDMS, as explained in Chapter 3.1. Table 7 shows the calculated base capacitance values for the sensors within the air-PDMS domain alongside the measured values. Furthermore, this was also done for the wafer with PI support layer (Table 8). Average base capacitance and yield were calculated out of 16 different measurements for each sensor type.

| | Geometry | Line width / Gap width | Calculated base capacitance | Measured base capacitance | yield |
|---|---|---|---|---|---|
| Sensor 1 | Spiral | 10/5 µm | 290 fF | 359 fF ±29 | 44 % |
| Sensor 2 | Spiral | 20/10 µm | 130 fF | 199 fF ±21 | 50 % |
| Sensor 3 | Serpentine | 10/5 µm | 290 fF | 363 fF ±23 | 38 % |
| Sensor 4 | Serpentine | 20/10 µm | 140 fF | 200 fF ±17 | 56 % |

Table 7: Simulated and measured base capacitance sensors before assembly.

Notably, the measured capacitance values were generally higher than was expected from simulations. Higher capacitance values may be explained by a combination of simulation and measurement inaccuracies, as well as photoresist residues that were still visible

| | Geometry | Line width / Gap width | Calculated base capacitance | Measured base capacitance | yield |
|---|---|---|---|---|---|
| Sensor 1 | Spiral | 10/5 µm | 301 fF | 415 fF ±70 | 44 % |
| Sensor 2 | Spiral | 20/10 µm | 138 fF | x 207 fF ±43 | 81 % |
| Sensor 3 | Serpentine | 10/5 µm | 300 fF | 408 fF ±82 | 81 % |
| Sensor 4 | Serpentine | 20/10 µm | 147 fF | 207 fF ±42 | 68 % |

Table 8: Simulated and measured base capacitance sensors with PI support layer before assembly.

on the sensors, interconnects, and bonding pads, as shown in Figure 6.2.1. The photoresist likely increased the base capacitance due to its higher relative dielectric permittivity (3-4) compared to air (1), and could explain the variation in measured values, since the residues were not equally distributed. Furthermore, the fabricated sensors developed a wrinkled surface (Figure 6.2.1) as a result of the expansion and subsequent shrinkage of PDMS caused by temperature variations during fabrication. This wrinkling increases the surface area of the sensors, thereby increasing their base capacitance.

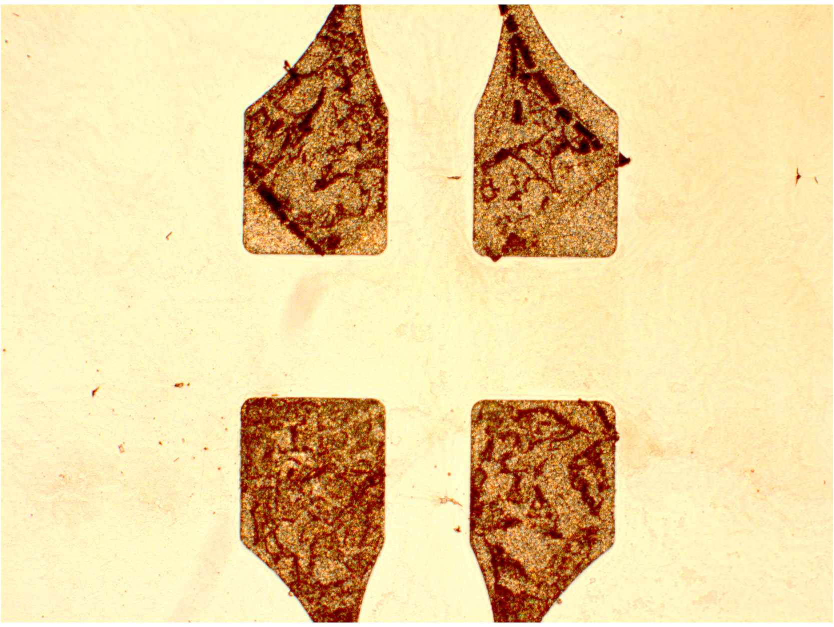

Figure 6.2: Photoresist residues on bonding pads.

The lower yield for the sensors without PI support layer was attributed to cracks that were sometimes visible along the interconnects, as shown in Figure 6.2.1. During the cleaning steps in acetone and IPA after oxide removal, as explained in Section 5.2, the wafer broke in multiple pieces, which likely exerted some stress on the membranes. Higher yield can probably be achieved if this was executed more carefully. After this incident, the etch depth of the dicing lines was reduced in the flowchart to provide the wafer with additional rigidity. The yield for the sensors with PI support layer was higher; however, large differences were observed across different parts of the wafer. Sensor defects in these cases were not attributed to cracks, but likely caused by slight underetching of some parts of the wafer, as shown in Figure 6.2.1, resulting in shorted measurement values.

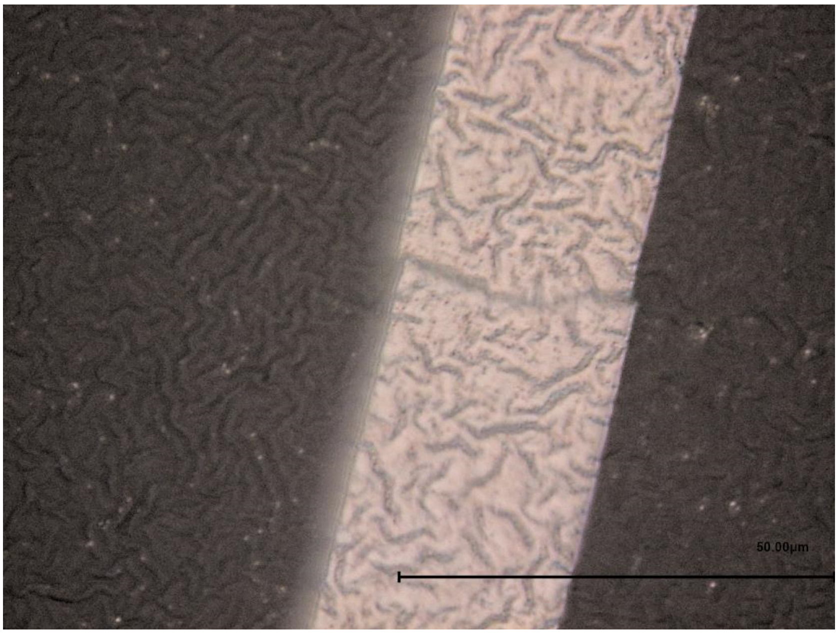

Figure 6.3: Cracked interconnect.

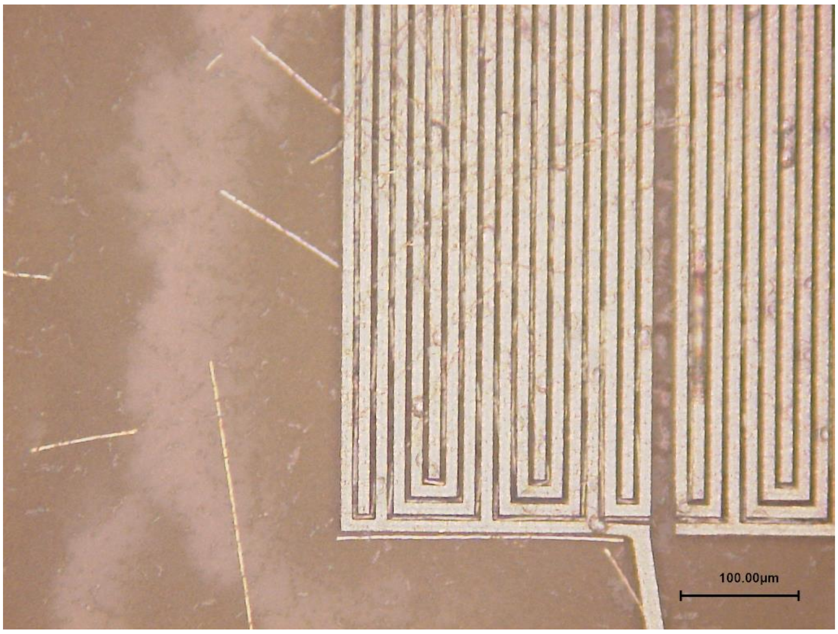

Figure 6.4: Aluminum traces in between the sensors caused by under-etching.

### 6.2.2 Base capacitance after assembly

A total of 4 sensors, one of each type, was taken to further assembly. Pillars were mounted on top of the sensors, and the EHT platforms where then glued and wirebonded to a PCB, as described in Section 6.1. After assembly, the base capacitance of the sensors was again measured to determine how many sensors survived. The measurement results are listed in Table 9.

| | Geometry | Line width / Gap width | Calculated base capacitance | Measured base capacitance | yield |
|---|---|---|---|---|---|
| Sensor 1 | Spiral | 10/5 µm | 532 fF | 996 fF ±8 | 75 % |
| Sensor 2 | Spiral | 20/10 µm | 264 fF | 833 fF ±7 | 100 % |
| Sensor 3 | Serpentine | 10/5 µm | 530 fF | 1003 fF ±7 | 100 % |
| Sensor 4 | Serpentine | 20/10 µm | 260 fF | 804 fF ±5 | 100 % |

Table 9: Simulated and measured base capacitance sensors after assembly

The measured base capacitance was significantly higher than the calculated base capacitance. Partially this can be expected, as the calculations did not account for the additional parasitic capacitance as result from the extended tracks through the PCB, and additional electric field interferences from outside, since these sensors were not measured in a shielded environment. However, the extent of the increase that can be expected remains unclear and requires further investigation, alongside additional measurements for statistical significance.

## 6.3 Dynamic measurements

Dynamic measurements were conducted to investigate the change in capacitance of the sensors upon substrate deformation. The setup for the dynamic measurements is shown in Figure 6.5. Dynamic measurements were conducted using a FemtoTools Nanomechanical Testing System FT-NMT03 (component 1 in Figure 6.5a), which is a nanoindenter that was used to apply a force to the pillars. The resulting changes in capacitance due to the substrate deformation could then be measured, simulating the contraction of engineered heart tissue. The force was applied with a flat, circular silicon probe, 50 µm in diameter, angled at 15° from the horizontal plane. Probe movement was controlled by a micro-positioning stage connected to a computer (component 2 in Figure 6.5a). For sensor readout, the platform was wirebonded to a custom PCB, which was attached to a metal holder on the nanoindenter. To accommodate the nanoindenter probe, the platform's elliptical well was removed. The PCB was connected to a readout system (AD7746) with coaxial cables. The AD7746 was placed within a Faraday cage to reduce signal noise (component 3 in Figure 6.5a). Measurements were taken by pushing with the probe against the pillars, followed by a return to the initial position, replicating a single contraction cycle of engineered heart tissue. Real-time capacitance changes were monitored using a computer with AD7746 evaluation software (component 4 in Figure 6.5a).

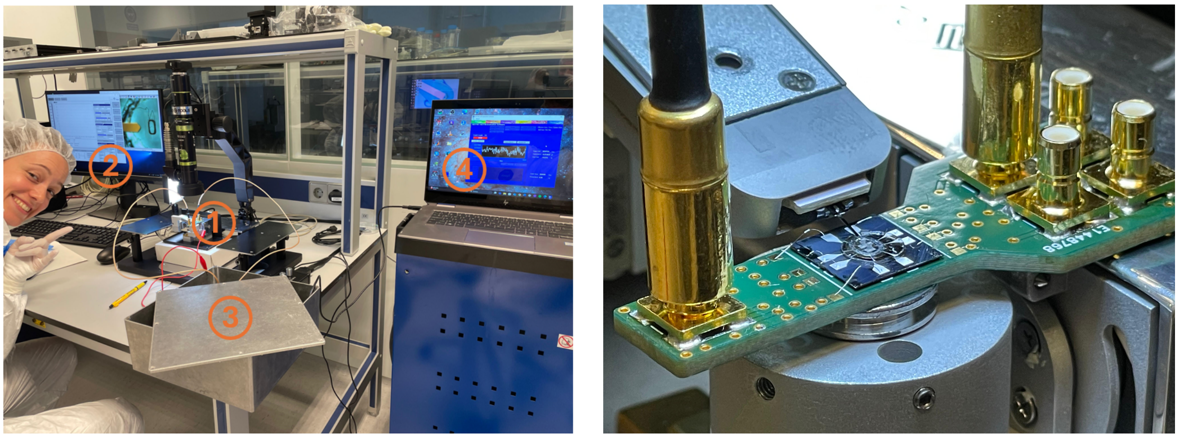

(a) (b)

Figure 6.5: Overview of the measurement setup. a) Complete overview, indicating each component. b) Close-up of component 1.

The sensor type with the highest expected sensitivity (sensor 3 from Table 9) was characterized on both sides of the pillar. During the measurements it was observed that the change in capacitance was highly affected by the movement of the probe itself. The probe is conductive and interferes with the electric field, changing the measured capacitance of the sensors as it moves, even without touching the pillars. Consequently, the total measured capacitance change resulting from the probe pushing against the pillars consits of two components: one due to the deformation of the substrate, and one due to the movement of the probe. Since only the capacitance change caused by substrate deformation is relevant, the component attributed to the movement of the probe needed to be isolated and removed from the total change in capacitance.

This was achieved in three steps:

1. The capacitance change was first measured as the probe pushed a specific distance against the pillar.
2. A second measurement was done where the probe was moved the same distance, but slightly next to the pillar, without touching it. This captured the capacitance change caused only by the movement of the probe.
3. The capacitance change from the second measurement was subtracted from the total capacitance change in the first measurement. This left only the capacitance change caused by substrate deformation (keeping slight inaccuracies from differences in probe positioning in mind).

To ensure that the capacitance change due to the movement of the probe could be accurately isolated, capacitance change was thus measured as function of distance moved by the probe (d), instead of force. The force matching the specific pillar displacement was then later calculated by using the numerical model from Chapter 3. All measurements were performed by pushing the probe a certain distance (d) against the pillar, followed by an immediate retraction of the probe, creating a step function in the change in capacitance over time. This was repeated for three different probe heights (h). Additionally, another set of measurements was performed where the probe height (h) was fixed at 300 µm, while varying the pushing distance (d), mimicing different heart tissue contraction forces. Figure 6.3 illustrates the variables (d) and (h) that were changed during the measurements, and the sensor positions. The measurements results are shown in Figures 6.7, 6.8, 6.9, and 6.10. The figures show a time window of three seconds during which the probe was quickly retracted, and the capacitance was continuously measured. The moment of probe retraction is clearly visible by the sudden change in capacitance, represented as a step function. Since the timing of the probe retraction varies, the step functions appear at different positions along the x-axis.

In order to compare the measured values with the numerical simulations, the capacitance change for different probe heights (h) and probe pushing distances (d) was simulated using the numerical model from Chapter 3 as well. The comparison between the measured values and the simulated values for both sensors are shown in Figure 6.11 and 6.12. By simulating the required pillar displacement, it was found that pushing distances of 50 µm, 100 µm and 150 µm at 300 µm height, require forces of 900 µN, 1800 µN, and 2700 µN respectively. Although these forces are much higher than the expected force that engineered heart tissues can produce (100 µN) [3], these deformations were neccessary in order to gain any notable change in capacitance during the measurements.

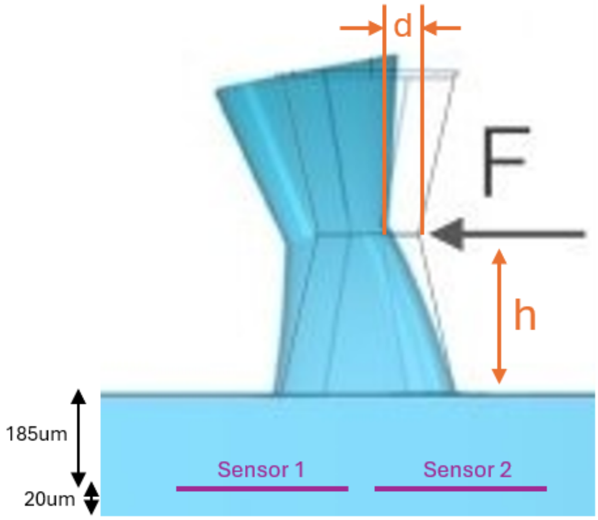

Figure 6.6: Setup dynamic measurements. Showing the sensor positions (sensor 1 & 2), the direction of the force exerted by the probe (F), and the variable variable parameters: pushing distance (d) and probe height (h).

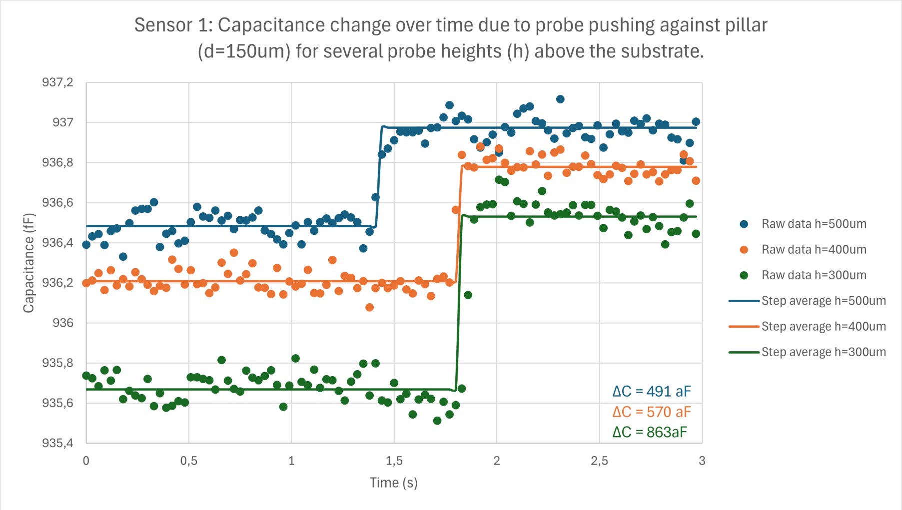
Sensor 1: Capacitance change over time due to probe pushing against pillar (d=150um) for several probe heights (h) above the substrate.

(a)

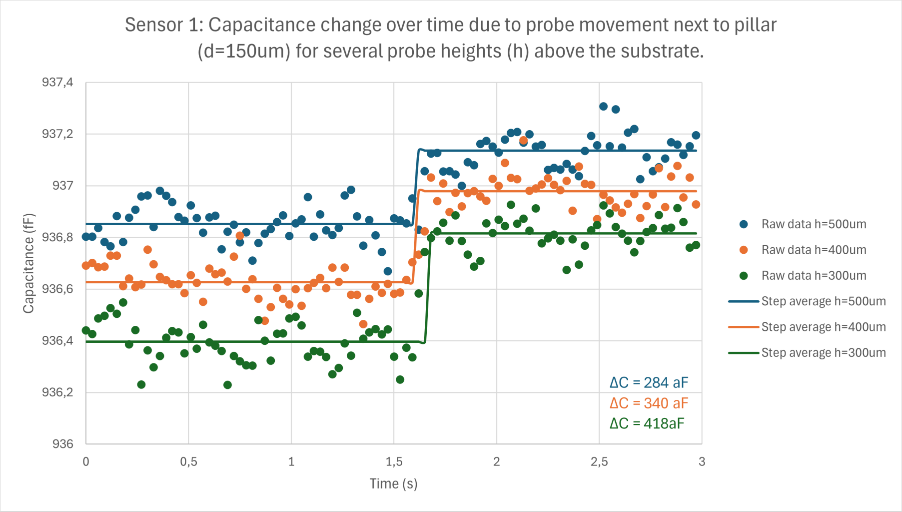
Sensor 1: Capacitance change over time due to probe movement next to pillar (d=150um) for several probe heights (h) above the substrate.

(b)

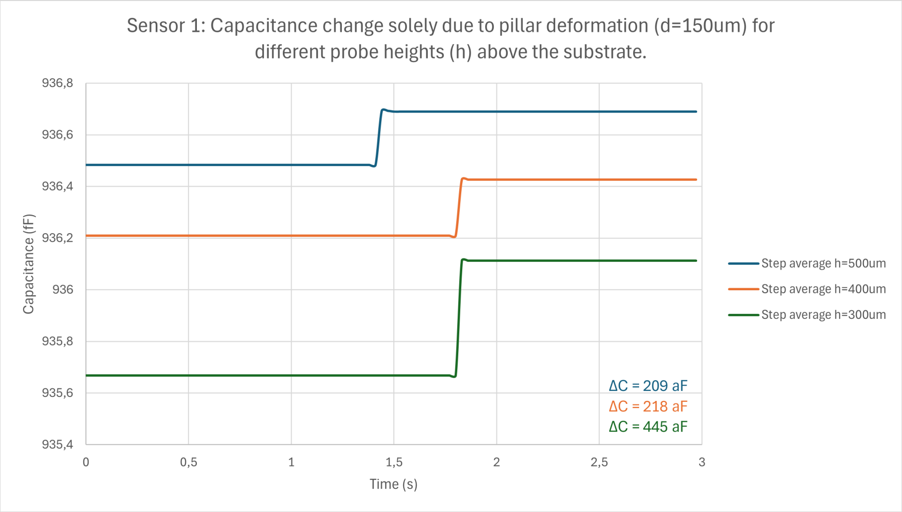
Sensor 1: Capacitance change solely due to pillar deformation (d=150um) for different probe heights (h) above the substrate.

(c)

Figure 6.7: Measurement results sensor 1 for varying probe heights (h) and fixed pushing distance (d=150 µm). a) Total capacitance change. b) Isolated capacitance change from probe movement. c) Isolated capacitance change from substrate deformation.

(a)

(b)

(c)

Figure 6.8: Measurement results sensor 2 for varying probe heights (h) and fixed pushing distance (d=150 µm). a) Total capacitance change. b) Isolated capacitance change from probe movement. c) Isolated capacitance change from substrate deformation.

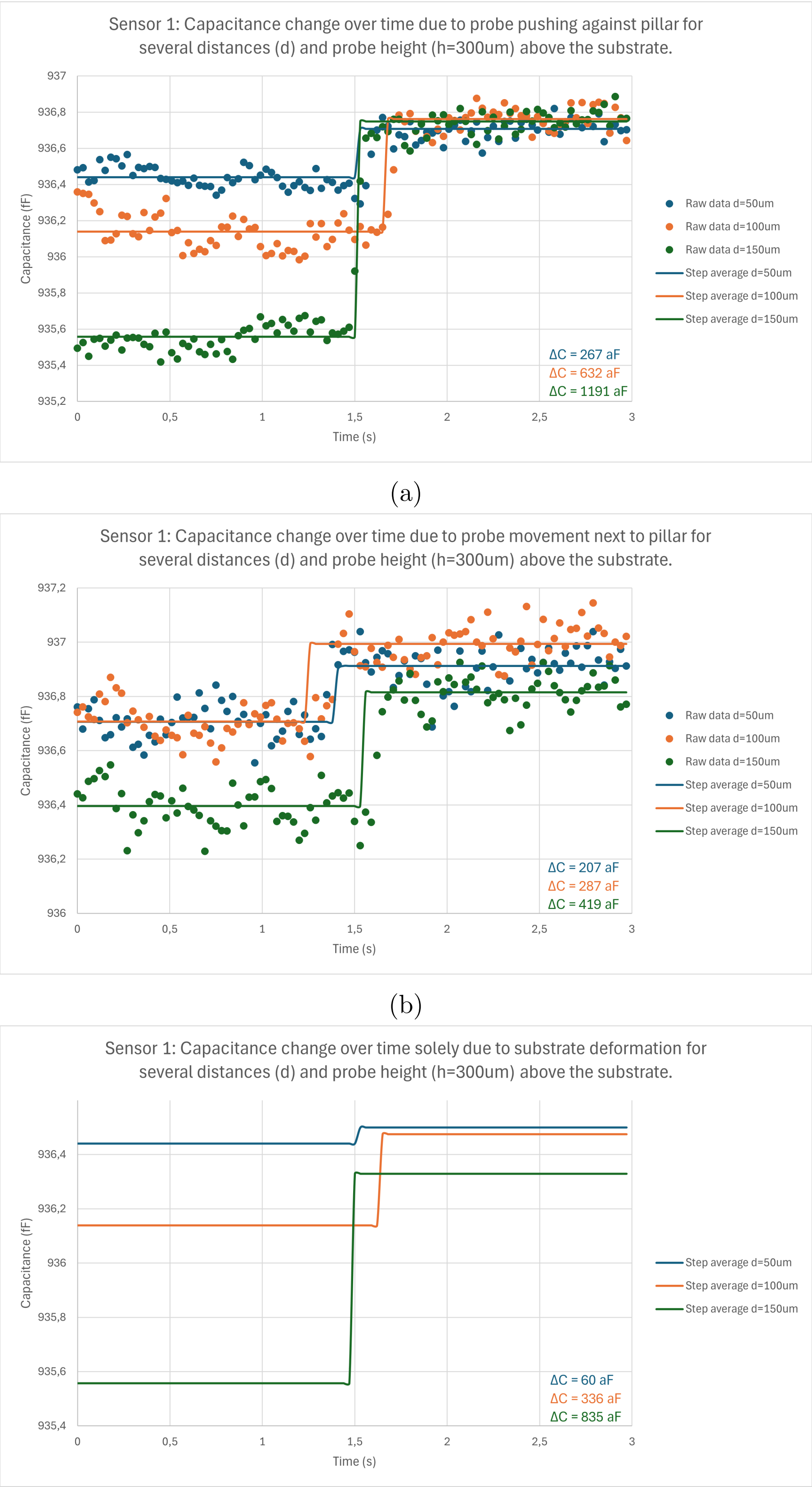

(a)

(b)

(c)

Figure 6.9: Measurement results sensor 1 for varying pushing distance (d) and fixed probe height (h=300 µm). a) Total capacitance change. b) Isolated capacitance change from probe movement. c) Isolated capacitance change from substrate deformation.

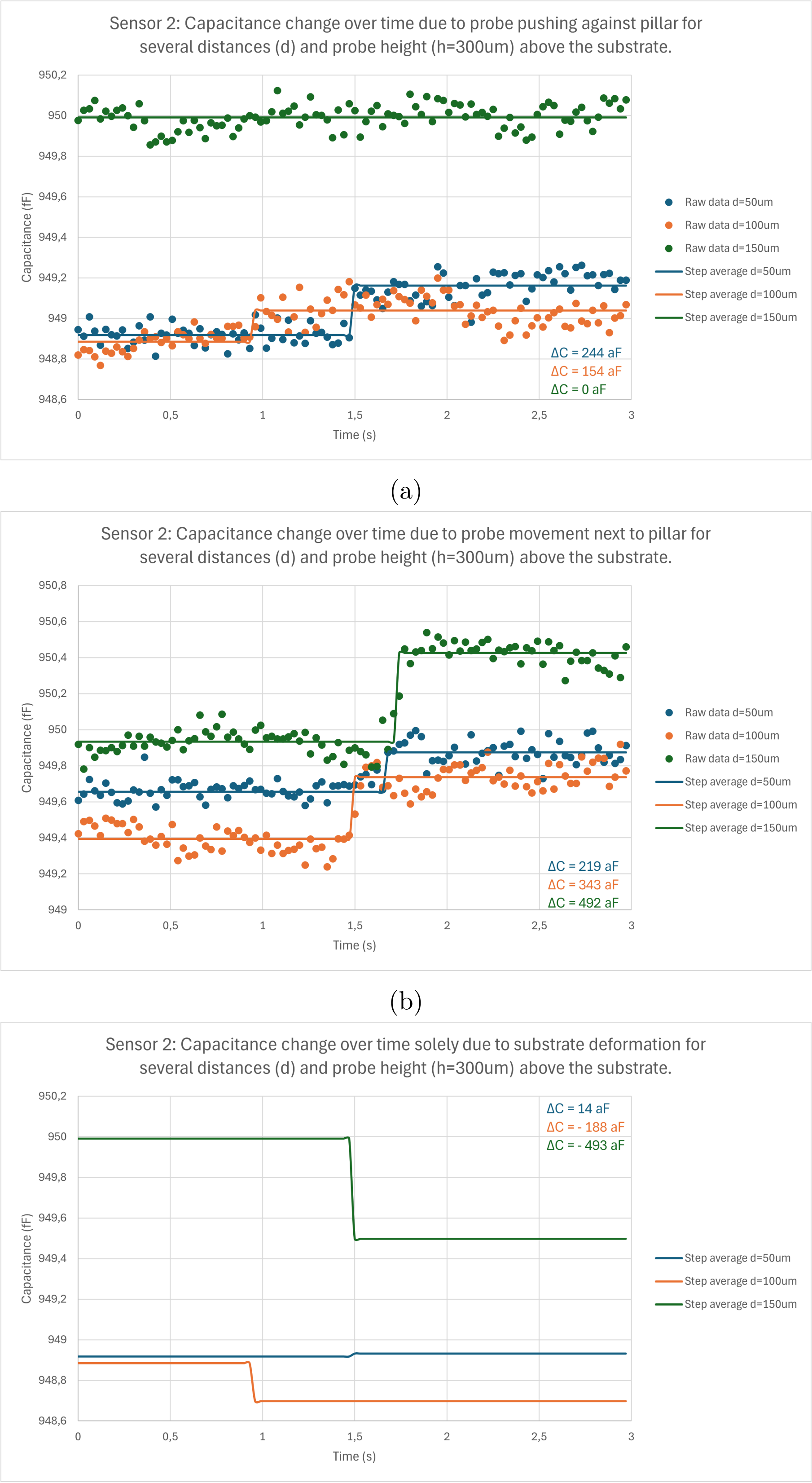

(a)

(b)

(c)

Figure 6.10: Measurement results sensor 2 for varying pushing distance (d) and fixed probe height (h=300 µm). a) Total capacitance change. b) Isolated capacitance change from probe movement. c) Isolated capacitance change from substrate deformation.

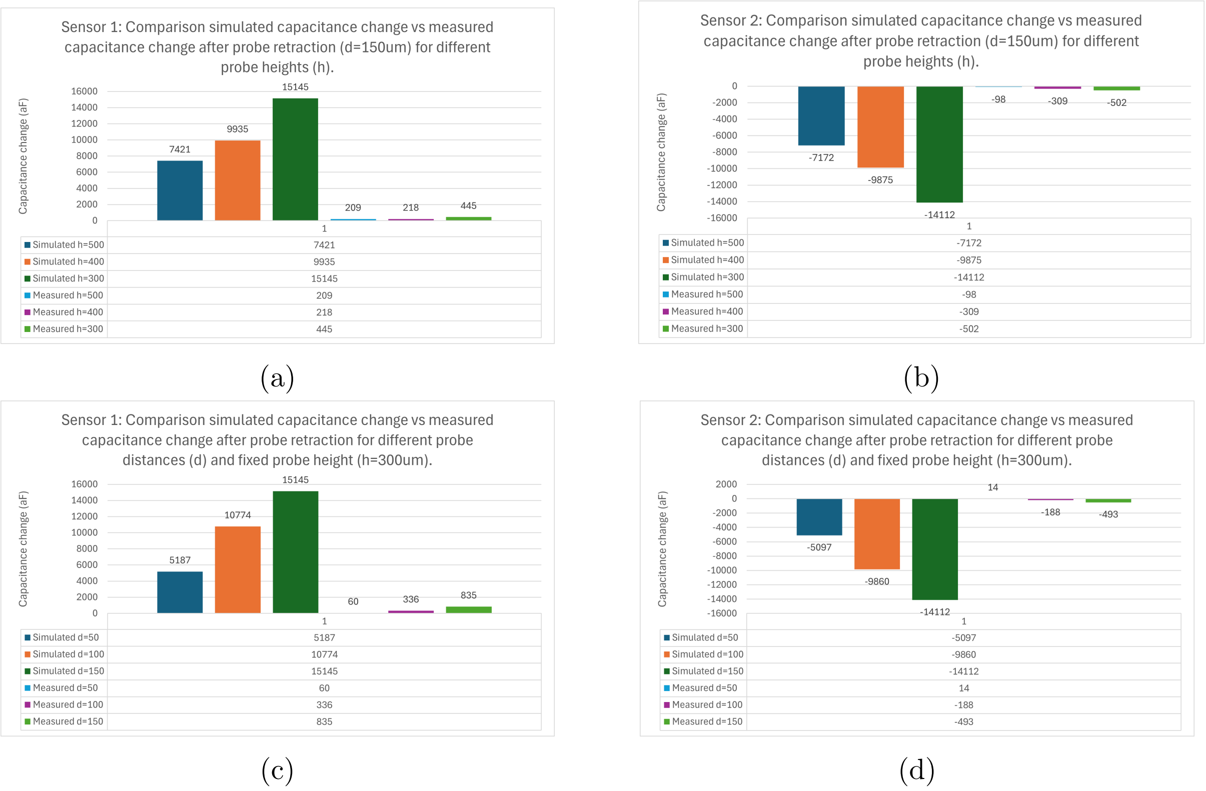

| | 1 |
|---|---|
| Simulated h=500 | 7421 |
| Simulated h=400 | 9935 |
| Simulated h=300 | 15145 |
| Measured h=500 | 209 |
| Measured h=400 | 218 |
| Measured h=300 | 445 |

(a)

| | 1 |
|---|---|
| Simulated h=500 | -7172 |
| Simulated h=400 | -9875 |
| Simulated h=300 | -14112 |
| Measured h=500 | -98 |
| Measured h=400 | -309 |
| Measured h=300 | -502 |

(b)

| | 1 |
|---|---|
| Simulated d=50 | 5187 |
| Simulated d=100 | 10774 |
| Simulated d=150 | 15145 |
| Measured d=50 | 60 |
| Measured d=100 | 336 |
| Measured d=150 | 835 |

(c)

| | 1 |
|---|---|
| Simulated d=50 | -5097 |
| Simulated d=100 | -9860 |
| Simulated d=150 | -14112 |
| Measured d=50 | 14 |
| Measured d=100 | -188 |
| Measured d=150 | -493 |

(d)

Figure 6.11: Comparison simulated capacitance change and measured capacitance change after probe retraction for different probe heights (h) and probe distances (d).

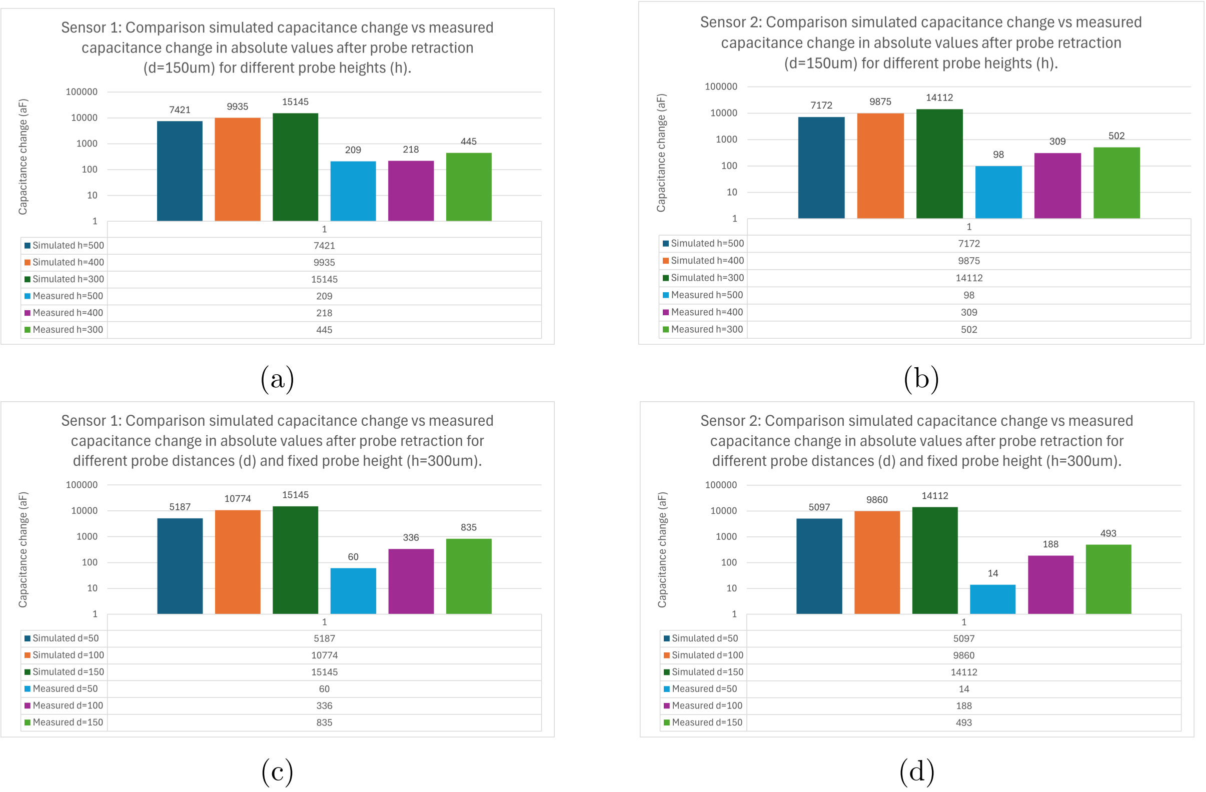

| | 1 |
|---|---|
| Simulated h=500 | 7421 |
| Simulated h=400 | 9935 |
| Simulated h=300 | 15145 |
| Measured h=500 | 209 |
| Measured h=400 | 218 |
| Measured h=300 | 445 |

(a)

| | 1 |
|---|---|
| Simulated h=500 | 7172 |
| Simulated h=400 | 9875 |
| Simulated h=300 | 14112 |
| Measured h=500 | 98 |
| Measured h=400 | 309 |
| Measured h=300 | 502 |

(b)

| | 1 |
|---|---|
| Simulated d=50 | 5187 |
| Simulated d=100 | 10774 |
| Simulated d=150 | 15145 |
| Measured d=50 | 60 |
| Measured d=100 | 336 |
| Measured d=150 | 835 |

(c)

| | 1 |
|---|---|
| Simulated d=50 | 5097 |
| Simulated d=100 | 9860 |
| Simulated d=150 | 14112 |
| Measured d=50 | 14 |
| Measured d=100 | 188 |
| Measured d=150 | 493 |

(d)

Figure 6.12: Data from Figure 6.11 in absolute values and **logarithmic scale** for better visual representation.

The following observations were made after analyzing the results:

1. The magnitude of the capacitance change estimated by simulations is significantly higher compared to the simulations (Figure 6.11).
2. The measured change in capacitance due to the deformation of the substrate increases when the probe is moved the same distance (150 µm) at a lower height (h) (Figure 6.12a and 6.12b). This behavior is in accorance with simulations, and is expected because pushing the same distance lower on the pillar, closer to its base, results in greater deformation compared to pushing near the tip of the pillar. This behavior is consistent with the fact that deforming the pillar near its base requires more force, because the moment arm is shorter.
3. The measured change in capacitance due to the deformation of the substrate increases by greater probe pushing distances (d) (Figure 6.12c and 6.12d). This behavior is in accordance with simulations, and is expected because larger pushing distances result in larger deformation.
4. Sensors on opposite site of the pillar have opposite change in capacitance (Figure 6.7c, 6.8c, 6.9c, and 6.10c). This behavior is also in accordance with simulations (Figure 6.11). However, this behavior is more symmetrical in the simulations compared to the measurements.

Although the magnitude of capacitance observed in simulations differs significantly from the measurements, some characteristics of the sensor's response to varying probe distances (d) and probe heights (h) were successfully captured. This suggests that the measurements can be somewhat trusted. However, the results clearly exhibit inaccuracies. For instance, in Figure 6.11d, the measured value for a probe distance of 50 µm shows a small positive value, whereas a negative value would be expected. Additionally, the measurements were affected by significant noise relative to the signal, which may explain these inaccuracies, as can be seen in the raw data shown in Figures 6.7 through 6.10.

The discrepancy between the magnitude of capacitance in simulations and measurements remains unclear, but several ideas include:

1. While previous work by Dostanic [3] demonstrated that simulations accurately predicted pillar displacement under an applied force and base capacitance in agreement with measurements (Table 7), inaccuracies might arise when combining displacement and capacitance change in the simulations. These simulations integrate three different modules in COMSOL: solid mechanics, shell, and electrostatics, as illustrated in Figure 3.2. Potential mistakes in the set-up between these modules could lead to errors and require further investigation.
2. The platform may experience pre-strain due to the weight of the pillars and the microwell, which was not accounted for in the simulations. This pre-strain could result in less deformation of the substrate in reality than predicted by the simulations.
3. During platform assembly, the connection between the top and bottom halves of the substrate might not have been properly established. Trapped air bubbles between the two layers could hinder force transmission through the substrate, reducing deformation compared to simulation predictions.

Repeated measurements including different sensor types could also provide more insights in the validity of simulations and measurements. These measurements would ideally be done in a setup where noise is further reduced, which could be achieved by using connectors and cables that are better in minimizing noise compared to the used coaxial cables.

# 7 Conclusion & Perspectives

In this thesis, a novel re-design of co-planar capacitive displacement sensors was developed, fabricated, and characterized to measure tissue contraction force in an EHT platform. The main design challenges included optimizing sensor sensitivity, and enhancing platform rigidity to prevent sensor cracking during the assembly steps of the EHT platform. To optimize sensitivity, Comsol Multiphysics simulations were used to determine the ideal sensor geometry, positioning, and substrate dimensions. Results indicated that a serpentine geometry with optimized line and gap widths on a minimally thick, suspended membrane would yield the highest sensitivity. Considering fabrication constraints, multiple designs were developed with varying line and gap widths. A new flowchart was developed for fabrication of four different sensor designs. Fabrication was done using wafer-level microfabrication and polymer processing techniques in a cleanroom environment. By incorporating a rigid silicon base in the EHT platform, substrate deformation during assembly was significantly reduced, minimizing the risk of sensor cracking. Additional PI support layers were also included, and their impact on improving the sensor yield was investigated. Finally, the sensors were electrically characterized in static and dynamic conditions. Static measurements were included investigate sensor yield. Dynamic measurements were then performed to mimic contraction of engineered heart tissue, investigating the possibility of using these sensors for assessment of tissue contraction force.

All sensor designs were successfully fabricated, however, several fabrication challenges such as breakage of the wafer during final cleaning steps after oxide removal, and slight underetching, which left aluminum residues in between the sensors' metal lines, negatively affected the yield. The yield of the sensors could likely be optimized with refined handling protocols after oxide removal, and an optimized etching process. Another recurring difficulty was photoresist residues on top of the sensors, as these were difficult to remove. Longer immersion in NI555 (a chemical for negative photoresist removal), and ensuring that no photoresist is left on top of the sensors before DRIE, may improve results, as discussed in Chapter 5.3. Additionally, elevated temperature (around 50 °C), and ultrasound during NI555 immersion could help in photoresist removal, although there is an expected risk of sensor delamination from ultrasound, depending on parameters such as ultrasonic power and frequency.

The sensors that survived were characterized by measuring their base capacitance before and after assembly. Characterization of the base capacitance before assembly showed values in agreement with simulations, although the base capacitance was slightly higher than anticipated. This increase could be explained by photoresist residues on top of the sensors, and an increased surface area of the sensors due to wrinkles that were formed during fabrication. After assembly, a further increase in base capacitance was measured, leading to capacitance values that were between two and three times higher than anticipated. Further investigation is required to determine whether this increase is due to parasitic capacitance from environmental factors (such as the PCB materials, nearby electronics, or human proximity), or due to measurement or calculation errors.

Dynamic measurements were conducted to evaluate capacitance changes resulting from substrate deformation using a nanoindenter. The investigation focused on the most sensitive sensor type, examining its response to varying indentation distances and heights. While the sensor's response to changing these parameters aligned with simulation results, there was a significant discrepancy in the magnitude of the capacitance changes. The capacitance changes predicted by simulations were much higher than those observed experimentally. Further investigation is needed to determine whether this discrepancy stems from inaccuracies in simulations, measurements, or fabrication processes, as discussed in Section 6.3.

In the current condition, the minimum force required to induce a measurable capacitance change was 900 µN at a height of 300 µm, approximately the position where heart tissue would interact with the pillar. This force exceeds the contraction force of heart tissues (around 100 µN), making the platform unsuitable for this application in its current form.

Future work could aim to further investigate the discrepancy between simulated and measured capacitance changes observed in the dynamic measurements. This could begin by conducting additional experiments with various sensor types to improve statistical significance. If the discrepancy persists, simplified models could be used for further analysis. For example, measurements could be performed using the platform without the pillars to evaluate whether the numerical model accurately predicts capacitance changes in this simplified setup. This approach could help identify whether the issue lies with the numerical model itself or with the pillar assembly process, as discussed in Section 6.3.

Future work could also focus on improving the sensor sensitivity by further reducing the substrate thickness below the pillars, as reducing this thickness exponentially increases sensor sensitivity according to simulations (3.17). The substrate thickness during the measurements was around 205 µm. Achieving thinner substrates is challenging because the substrate requires a minimum thickness to be successfully peeled from the mold used for fabricating the pillars without tearing. However, alternative fabrication methods, such as 3D printing, might provide a solution to achieve thinner substrates. Additionally, narrower gap width between the metal lines could also significantly increase sensitvity according to simulations (Figure 3.13). However, this will also introduce challenges with fabrication.

Finally, the signal noise during the dynamic measurements was around 100 aF (Figures 6.7 - 6.10), which is too high for the signal strength being measured. Noise reduction may be achieved by measuring in a shielded environment. Additionally, optimizing measurements by using shorter cables and high-quality connectors designed to minimize noise can further enhance performance. By reducing noise, it would become possible to detect smaller capacitance changes, thereby lowering the minimum force currently required for measurable results, and thus improving the detection limit of the sensors.

With these adaptations, it might become feasible to measure capacitance changes caused by the contraction of engineered heart tissue. Repeated experiments under the suggested improved conditions could offer further insights into the sensors' feasibility for real-time tissue contraction force monitoring, potentially advancing applications in EHT research.

# References

[1] W. H. O. Who, "The top 10 causes of death," *World Health Organization: WHO*, Dec. 2020.

[2] D. Sun, W. Gao, H. Hu, and S. Zhou, "Why 90% of clinical drug development fails and how to improve it?," *Acta Pharmaceutica Sinica. B*, vol. 12, p. 3049, July 2022.

[3] M. Dostanic, "Miniature sensorized platform for engineered heart tissues, PhD thesis TU Delft," 2023. [Online; accessed 25. Sep. 2023].

[4] "Mortality and Cause of Death, 1900 v. 2010 | Carolina Demography," July 2019. [Online; accessed 14. Jun. 2023].

[5] K. Taylor and L. R. Alvarez, "An Estimate of the Number of Animals Used for Scientific Purposes Worldwide in 2015," *Altern. Lab. Anim.*, vol. 47, pp. 196–213, Nov. 2019.

[6] "Research and Development in the Pharmaceutical Industry," Aug. 2021. [Online; accessed 12. Jun. 2023].

[7] "Tell the USDA: Do Your Job to Protect Animals in Labs! | PETA," May 2018. [Online; accessed 26. Sep. 2024].

[8] Q. Wu, J. Liu, X. Wang, L. Feng, J. Wu, X. Zhu, W. Wen, and X. Gong, "Organ-on-a-chip: recent breakthroughs and future prospects," *Biomed. Eng. Online*, vol. 19, pp. 1–19, Dec. 2020.

[9] C. M. Leung, P. de Haan, K. Ronaldson-Bouchard, G.-A. Kim, J. Ko, H. S. Rho, Z. Chen, P. Habibovic, N. L. Jeon, S. Takayama, M. L. Shuler, G. Vunjak-Novakovic, O. Frey, E. Verpoorte, and Y.-C. Toh, "A guide to the organ-on-a-chip," *Nat. Rev. Methods Primers*, vol. 2, pp. 1–29, May 2022.

[10] C. Cofiño-Fabres, T. Boonen, J. M. Rivera-Arbeláez, M. Rijpkema, L. Blauw, P. C. N. Rensen, V. Schwach, M. C. Ribeiro, and R. Passier, "Micro-Engineered Heart Tissues On-Chip with Heterotypic Cell Composition Display Self-Organization and Improved Cardiac Function," *Adv. Healthcare Mater.*, vol. 13, p. 2303664, July 2024.

[11] Q. Yang, Z. Xiao, X. Lv, T. Zhang, and H. Liu, "Fabrication and Biomedical Applications of Heart-on-a-chip," *International Journal of Bioprinting*, vol. 7, no. 3, 2021.

[12] W. E. Knight, Y. Cao, Y.-H. Lin, C. Chi, B. Bai, G. C. Sparagna, Y. Zhao, Y. Du, P. Londono, J. A. Reisz, B. C. Brown, M. R. G. Taylor, A. V. Ambardekar, J. C. Cleveland, Jr., T. A. McKinsey, M. Y. Jeong, L. A. Walker, K. C. Woulfe, A. D'Alessandro, K. C. Chatfield, H. Xu, M. R. Bristow, P. M. Buttrick, and K. Song, "Maturation of Pluripotent Stem Cell-Derived Cardiomyocytes Enables Modeling of Human Hypertrophic Cardiomyopathy," *Stem Cell Rep.*, vol. 16, p. 519, Feb. 2021.

[13] T. Kamakura, T. Makiyama, K. Sasaki, Y. Yoshida, Y. Wuriyanghai, J. Chen, T. Hattori, S. Ohno, T. Kita, M. Horie, S. Yamanaka, and T. Kimura, "Ultrastructural Maturation of Human-Induced Pluripotent Stem Cell-Derived Cardiomyocytes in a Long-Term Culture," *Circ. J.*, vol. 77, no. 5, pp. 1307–1314, 2013.

[14] E. Giacomelli, V. Meraviglia, G. Campostrini, A. Cochrane, X. Cao, R. W. J. van Helden, A. K. Garcia, M. Mircea, S. Kostidis, R. P. Davis, B. J. van Meer, C. R. Jost, A. J. Koster, H. Mei, D. G. Míguez, A. A. Mulder, M. Ledesma-Terrón, G. Pompilio, L. Sala, D. C. F. Salvatori, R. C. Slieker, E. Sommariva, A. A. F. de Vries, M. Giera, S. Semrau, L. G. J. Tertoolen, V. V. Orlova, M. Bellin, and C. L. Mummery, "Human-iPSC-Derived Cardiac Stromal Cells Enhance Maturation in 3D Cardiac Microtissues and Reveal Non-cardiomyocyte Contributions to Heart Disease," *Cell Stem Cell*, vol. 26, pp. 862–879.e11, June 2020.

[15] D. Carson, M. Hnilova, X. Yang, C. L. Nemeth, J. H. Tsui, A. S. T. Smith, A. Jiao, M. Regnier, C. E. Murry, C. Tamerler, and D.-H. Kim, "Nanotopography-Induced Structural Anisotropy and Sarcomere Development in Human Cardiomyocytes Derived from Induced Pluripotent Stem Cells," *ACS Appl. Mater. Interfaces*, vol. 8, pp. 21923–21932, Aug. 2016.

[16] K. Ronaldson-Bouchard, S. P. Ma, K. Yeager, T. Chen, L. Song, D. Sirabella, K. Morikawa, D. Teles, M. Yazawa, and G. Vunjak-Novakovic, "Advanced maturation of human cardiac tissue grown from pluripotent stem cells," *Nature*, vol. 556, pp. 239–243, Apr. 2018.

[17] S. Saheera and P. Krishnamurthy, "Cardiovascular Changes Associated with Hypertensive Heart Disease and Aging," *Cell Transplant.*, vol. 29, Jan. 2020.

[18] K. M. Beussman, M. L. Rodriguez, A. Leonard, N. Taparia, C. R. Thompson, and N. J. Sniadecki, "Micropost arrays for measuring stem cell-derived cardiomyocyte contractility," *Methods*, vol. 94, pp. 43–50, Feb. 2016.

[19] M. Sakamiya, Y. Fang, X. Mo, J. Shen, and T. Zhang, "A heart-on-a-chip platform for online monitoring of contractile behavior via digital image processing and piezoelectric sensing technique," *Med. Eng. Phys.*, vol. 75, pp. 36–44, Jan. 2020.

[20] K. S. Bielawski, A. Leonard, S. Bhandari, C. E. Murry, and N. J. Sniadecki, "Real-Time Force and Frequency Analysis of Engineered Human Heart Tissue Derived from Induced Pluripotent Stem Cells Using Magnetic Sensing," *Tissue Eng. Part C Methods*, vol. 22, pp. 932–940, Oct. 2016.

[21] D.-S. Kim, Y. W. Choi, A. Shanmugasundaram, Y.-J. Jeong, J. Park, N.-E. Oyunbaatar, E.-S. Kim, M. Choi, and D.-W. Lee, "Highly durable crack sensor integrated with silicone rubber cantilever for measuring cardiac contractility," *Nat. Commun.*, vol. 11, 2020.

[22] A. M. G. Martins, M. D. Wilkins, F. S. Ligler, M. A. Daniele, and D. O. Freytes, "Microphysiological System for High Throughput Computer Vision Measurement of Microtissue Contraction," *ACS Sens.*, vol. 6, p. 985, Mar. 2021.

[23] Y. Zhao, N. Rafatian, N. T. Feric, B. J. Cox, R. Aschar-Sobbi, E. Y. Wang, P. Aggarwal, B. Zhang, G. Conant, K. Ronaldson-Bouchard, A. Pahnke, S. Protze, J. H. Lee, L. D. Huyer, D. Jekic, A. Wickeler, H. E. Naguib, G. M. Keller, G. Vunjak-Novakovic, U. Broeckel, P. H. Backx, and M. Radisic, "A Platform for Generation of Chamber-Specific Cardiac Tissues and Disease Modeling," *Cell*, vol. 176, pp. 913–92718, Feb. 2019.

[24] Y. S. Zhang, J. Aleman, A. Arneri, S. Bersini, F. Piraino, S. R. Shin, M. R. Dokmeci, and A. Khademhosseini, "From Cardiac Tissue Engineering to Heart-on-a-Chip: Beating Challenges," *Biomedical materials (Bristol, England)*, vol. 10, no. 3, p. 034006, 2015.

[25] S. Cho, D. E. Discher, K. W. Leong, G. Vunjak-Novakovic, and J. C. Wu, "Challenges and opportunities for the next generation of cardiovascular tissue engineering," *Nat. Methods*, vol. 19, pp. 1064–1071, Sept. 2022.

[26] K. Andrysiak, J. Stepniewski, and J. Dulak, "Human-induced pluripotent stem cell-derived cardiomyocytes, 3D cardiac structures, and heart-on-a-chip as tools for drug research," *Pflügers Arch.*, vol. 473, no. 7, p. 1061, 2021.

[27] R. J. Mills, D. M. Titmarsh, X. Koenig, B. L. Parker, J. G. Ryall, G. A. Quaife-Ryan, H. K. Voges, M. P. Hodson, C. Ferguson, L. Drowley, A. T. Plowright, E. J. Needham, Q.-D. Wang, P. Gregorevic, M. Xin, W. G. Thomas, R. G. Parton, L. K. Nielsen, B. S. Launikonis, D. E. James, D. A. Elliott, E. R. Porrello, and J. E. Hudson, "Functional screening in human cardiac organoids reveals a metabolic mechanism for cardiomyocyte cell cycle arrest," *Proc. Natl. Acad. Sci. U.S.A.*, vol. 114, pp. 8372–8381, Oct. 2017.

[28] "F. Pfaiffer, "Towards a read-out for capacitive displacement sensor in an engineered heart tissue device, master thesis TU Delft' | TU Delft Repository," Nov. 2024. [Online; accessed 21. Nov. 2024].

[29] M. Shojaei Baghini, "Design and Development of Integrated Displacement Sensors for Engineered Heart Tissue Platforms, Master thesis TU Delft," 2020. [Online; accessed 25. Sep. 2023].

[30] M. Mwelango, T. Zhu, K. Wen, Z. Zhang, X. Yuan, W. Li, and X. Yin, "Coplanar capacitive sensors and their applications in non-destructive evaluation: a review," *Nondestructive Testing and Evaluation*, pp. 1–45, Apr. 2023.

[31] R. Qin, M. Hu, X. Li, T. Liang, H. Tan, J. Liu, and G. Shan, "A new strategy for the fabrication of a flexible and highly sensitive capacitive pressure sensor," *Microsyst. Nanoeng.*, vol. 7, pp. 1–12, Nov. 2021.

[32] F. Abdollahi-Mamoudan, S. Savard, T. Filleter, C. Ibarra-Castanedo, and X. P. V. Maldague, "Numerical Simulation and Experimental Study of Capacitive Imaging Technique as a Nondestructive Testing Method," *Appl. Sci.*, vol. 11, p. 3804, Apr. 2021.

[33] S. R. A. Ruth, V. R. Feig, H. Tran, and Z. Bao, “Microengineering Pressure Sensor Active Layers for Improved Performance,” *Adv. Funct. Mater.*, vol. 30, p. 2003491, Sept. 2020.

[34] I. D. Johnston, D. K. McCluskey, C. K. L. Tan, and M. C. Tracey, “Mechanical characterization of bulk Sylgard 184 for microfluidics and microengineering,” *J. Micromech. Microeng.*, vol. 24, p. 035017, Feb. 2014.

[35] R. N. Palchesko, L. Zhang, Y. Sun, and A. W. Feinberg, “Development of Polydimethylsiloxane Substrates with Tunable Elastic Modulus to Study Cell Mechanobiology in Muscle and Nerve,” *PLoS One*, vol. 7, p. e51499, Dec. 2012.

[36] E. Apaydin, “Microfabrication Techniques for Printing on PDMS Elastomers for Antenna and Biomedical Applications,” 2009. [Online; accessed 15. Aug. 2023].

[37] B. Marchiori, “Stretchable electronics towards the fabrication of organic sensors for artificial skin,” *ResearchGate*, Nov. 2018.

[38] H.-B. Lee, C.-W. Bae, L. T. Duy, I.-Y. Sohn, D.-I. Kim, Y.-J. Song, Y.-J. Kim, and N.-E. Lee, “Mogul-Patterned Elastomeric Substrate for Stretchable Electronics,” *Adv. Mater.*, vol. 28, pp. 3069–3077, Apr. 2016.

[39] E.-H. Ko, H.-J. Kim, S.-M. Lee, T.-W. Kim, and H.-K. Kim, “Stretchable Ag electrodes with mechanically tunable optical transmittance on wavy-patterned PDMS substrates,” *Sci. Rep.*, vol. 7, pp. 1–12, Apr. 2017.

[40] D. S. Gray, J. Tien, and C. S. Chen, “High-Conductivity Elastomeric Electronics,” *Adv. Mater.*, vol. 16, pp. 393–397, Mar. 2004.

[41] S. Béfahy, S. Yunus, V. Burguet, J.-S. Heine, and P. Bertrand, “Metallization Process for Polydimethylsiloxane (PDMS) Rubber,” *MRS Proceedings*, vol. 1009, Jan. 2007.

[42] R. Seghir and S. Arscott, “Controlled mud-crack patterning and self-organized cracking of polydimethylsiloxane elastomer surfaces,” *Sci. Rep.*, vol. 5, p. 14787, Oct. 2015.

[43] A. Ryspayeva, T. D. A. Jones, M. N. Esfahani, M. P. Shuttleworth, R. A. Harris, R. W. Kay, M. P. Y. Desmulliez, and J. Marques-Hueso, “A rapid technique for the direct metallization of PDMS substrates for flexible and stretchable electronics applications,” *Microelectron. Eng.*, vol. 209, pp. 35–40, Mar. 2019.

[44] A. Khosla and C. Patel, “Microfabrication and characterization of UV micropatternable, electrically conducting polyaniline photoresist blends for MEMS applications,” *Microsyst. Technol.*, vol. 22, pp. 371–378, Feb. 2016.

[45] O.-H. Huttunen, T. Happonen, J. Hiitola-Keinänen, P. Korhonen, J. Ollila, and J. Hiltunen, “Roll-To-Roll Screen-Printed Silver Conductors on a Polydimethyl Siloxane Substrate for Stretchable Electronics,” *Ind. Eng. Chem. Res.*, vol. 58, pp. 19909–19916, Oct. 2019.

[46] J. Jiang, B. Bao, M. Li, J. Sun, C. Zhang, Y. Li, F. Li, X. Yao, and Y. Song, "Fabrication of Transparent Multilayer Circuits by Inkjet Printing," *Adv. Mater.*, vol. 28, pp. 1420–1426, Feb. 2016.

[47] Z. Pu, J. Ma, W. Li, X. Lai, X. Su, H. Yu, and D. Li, "A flexible precise volume sensor based on metal-on-polyimide electrodes sandwiched by PDMS channel for microfluidic systems," *Microfluid. Nanofluid.*, vol. 23, pp. 1–11, Dec. 2019.

[48] A. Jahanshahi, M. Gonzalez, J. van den Brand, F. Bossuyt, T. Vervust, R. Verplancke, J. Vanfleteren, and J. De Baets, "Stretchable Circuits with Horseshoe Shaped Conductors Embedded in Elastic Polymers," *Jpn. J. Appl. Phys.*, vol. 52, p. 05DA18, May 2013.

[49] N. Chou, J. Jeong, and S. Kim, "Crack-free and reliable lithographical patterning methods on PDMS substrate," *J. Micromech. Microeng.*, vol. 23, p. 5035, Dec. 2013.

[50] Y.-J. Fu, H.-z. Qui, K.-S. Liao, S. J. Lue, C.-C. Hu, K.-R. Lee, and J.-Y. Lai, "Effect of UV-Ozone Treatment on Poly(dimethylsiloxane) Membranes: Surface Characterization and Gas Separation Performance," *Langmuir*, vol. 26, pp. 4392–4399, Mar. 2010.

[51] R. N. Simons, "Coplanar Waveguide with FiniteWidth Ground Planes," in *Coplanar Waveguide Circuits, Components, and Systems*, pp. 112–126, Wiley-IEEE Press, 2001.

[52] X. Hu and W. Yang, "Planar capacitive sensors – designs and applications," *Sensor Review*, vol. 30, pp. 24–39, Jan. 2010.

# Integration of displacement sensor on PDMS platform for culturing EHTs

## Flowchart

### Version 2
### 2th May 2024

| Batch information | | | |
|---|---|---|---|
| **Name of owner:** | **Thomas Bouman** | **Mask set:** | |
| **Name of mentor:** | **Milica Dostanic** | **Mask box:** | |
| **Run number:** | | **Die size:** | **9x9 mm** |
| **Wafer amount:** | **6** | **Start date:** | |
| **Subject to PCC:** | | **PCC approved:** | |

**EKL(Else Kooi Laboratory)**
**DELFT UNIVERSITY OF TECHNOLOGY**
Address Feldmannweg 17, 2628 CT Delft, The
P.O. Box 5053, 2600 GB Delft, The Netherlands
Phone : +31 - (0)15 - 2783868
Fax : +31 - (0)15 - 2622163
Website http://ekl.tudelft.nl/EKL/Home.php

# Fabrication of displacement sensors

| | # | FABRICATION STEP | PROCESS DESCRIPTION | NOTES |
|---|---|---|---|---|
| *Alignment marks* | 1 | Coating 1.4 um of photoresist | Recipe: "**Co - 3012 - zero layer**"<br>▪ HMDS @ 130º<br>▪ spin coating of Shipley SPR3012 positive resist<br>▪ a soft bake at 95 °C for 90 seconds<br>▪ an automatic edge bead removal with a solvent | Use no EBR for all coatings, because the EBR is not working |
| | 2 | Alignment and Exposure | Use ASML PAS5500/80 automatic wafer stepper.<br>▪ Mask **COMURK**, job "**ZEFWAM**" for alignment marks for contact aligner and stepper.<br>▪ Exposure energy is **150mJ** | The mask has two images. Don't forget to set correct energy for both of them |
| | 3 | Development | Recipe "**Dev-SP**"<br>▪ a post-exposure bake at 115 °C for 90 seconds<br>▪ developing with Shipley MF322 with a single puddle process<br>▪ a hard bake at 100 °C for 90 seconds | |
| | 4 | Inspection | Visually inspect the wafers through a microscope, and check the line width and overlay | |
| | 5 | Etching | Use Rapier for etching alignment marks<br>▪ Recipe: "EKL_URK_20"<br>▪ Etch time : 30s<br>▪ Temperature: | Clean after etching the last wafer |
| | 6 | Photoresist removal | Use Tepla<br>**Program 1** : 1000 w power and automatic endpoint detection + 2 min. overetching | |
| *Front & Back side PECVD SiO2 deposition* | 7 | Cleaning | Use cleaning line in CR100<br>▪ 10 min in $HNO_3$ 99% (Si)<br>▪ 5 min rinsing or until the resistivity is 5 M$\Omega$.<br>▪ 10 min in $HNO_3$ 69,5% (Si) @ 110°C<br>▪ 5 min rinsing or until the resistivity is 5 M$\Omega$.<br>▪ Dry for 6 min in "rinser/dryer" | For less than 5 wafers use single wafer dryer |
| | 8 | PECVD oxide deposition: *2um front side* | Use Novellus Concept One PECVD reactor.<br>▪ Program recipe: xxx_siostd<br>▪ Time: variable<br>▪ Temperature: 400 °C | Stopping layer for silicon etching |

| | | | | |
|---|---|---|---|---|
| | 9 | PECVD oxide deposition:<br>*6um back side* | Use Novellus Concept One PECVD reactor.<br>▪ Program recipe: xxx_siostd<br>▪ Time: variable<br>▪ Temperature: 400 °C | Hard mask for DRIE silicon etching |
| | 10 | Measurement | Use Woolam ellipsometer to measure oxide thickness. | |
| *Define hard mask for back etching* | 11 | Cleaning | Use cleaning line in CR100<br>▪ 10 min in $HNO_3$ 99% (Si)<br>▪ 5 min rinsing or until the resistivity is 5 MΩ.<br>▪ 10 min in $HNO_3$ 69,5% (Si) @ 110°C<br>▪ 5 min rinsing or until the resistivity is 5 MΩ.<br>▪ Dry for 6 min in “rinser/dryer” | |
| | 12 | Coating 3.1um of photoresist. | Recipe: "**Co - Nlof - 3.5um**"<br>▪ HMDS @ 130º<br>▪ spin coating of negative positive resist<br>▪ soft bake 60s at 110 degrees. | |
| | 13 | Exposure | Use Contact Aligner<br>▪ Mask: “Back etch hole + dice lines”<br>▪ Contact: hard contact<br>▪ Exposure dose: 80mJ/cm^2 | |
| | 14 | Development | Recipe “**Only x-link bake**”<br>▪ Cross-link bake<br>Followed by:<br>Recipe “**Dev-lift off**”<br>▪ developing with a double puddle process<br>▪ hard bake at 100 °C for 90 seconds | |
| | 15 | Etching oxide back side | Use Drytek<br>▪ Recipe: stdoxide<br>▪ RF power: 300 W<br>▪ Etch time: 14 min | |
| | 16 | Photoresist removal | Use Tepla<br>**Program 1** : 1000 w power and automatic endpoint detection + 2 min. overetching | |
| | 17 | Cleaning | Use cleaning line in CR100<br>▪ 10 min in $HNO_3$ 99% (Si)<br>▪ 5 min rinsing or until the resistivity is 5 MΩ.<br>▪ 10 min in $HNO_3$ 69,5% (Si) @ 110°C<br>▪ 5 min rinsing or until the resistivity is 5 MΩ.<br>▪ Dry for 6 min in “rinser/dryer” | |

| | | | | |
|---|---|---|---|---|
| | 18 | Coating of 5 um photoresist. | Recipe: "**Co - Nlof - 5um**"<br>▪ HMDS @ 130º<br>▪ spin coating of negative positive resist<br>▪ soft bake 60s at 110 degrees. | |
| | 19 | Exposure | Use Contact Aligner<br>▪ Mask: “Back etch hole”<br>▪ Contact: hard contact<br>▪ Exposure dose: 180mJ/cm2 | |
| | 20 | Development | Recipe “**Only x-link bake**”<br>▪ Cross-link bake<br>Followed by:<br>Recipe “**Dev-lift off**”<br>▪ developing with a double puddle process<br>hard bake at 100 °C for 90 seconds | |
| | 21 | DRIE of 150um cavities | Use Rapier:<br>▪ Recipe: EKL_Smooth_20C<br>▪ Cycles: to be determined | |
| | 22 | Photoresist removal | Use Tepla<br>**Program 1** : 1000 w power and automatic endpoint detection + 2 min. overetching | |
| *PDMS deposition* | 22 | Cleaning | Use cleaning line in CR100<br>▪ 10 min in $HNO_3$ 99% (Si)<br>▪ 5 min rinsing or until the resistivity is 5 M$\Omega$.<br>▪ 10 min in $HNO_3$ 69,5% (Si) @ 110°C<br>▪ 5 min rinsing or until the resistivity is 5 M$\Omega$.<br>▪ Dry for 6 min in “rinser/dryer” | |
| | 23 | Coating 3um of photoresist back-side wafer | Use manual spinner.<br>▪ Recipe: 3.1um EC3027<br>▪ Speed:<br>Followed by a post exposure bake (5 min @ 90 ºC) | To prevent adhesion on the backside during spin-coating |
| | 24 | PDMS mixing | Use Thinky Speedmixer<br>▪ Mix PDMS (10g) and curing agent (1g) in 10:1 ratio<br>▪ Program 01<br>▪ Time: 2 min total | Repeat two times because sometimes it is not mixed enough (especially for the small amounts). Wait a few min. for the machine to cool down. Clean the holder and weight afterwards with IPA |
| | 25 | PDMS spin-coating, 20um | Use manual spinner.<br>▪ Recipe: pdms_20um<br>▪ Speed: 4000 rpm<br>▪ Time: 40s<br>▪ Edge Bead Removal | Clean the backside after spin-coating by using the cotton sticks. Clean the PDMS from the edges of a wafer, making them clean for handling. Also, because of Al deposition later, PDMS has to be removed also from the alignment masks. Use Kapton tape to protect |

<table>
<tr><td rowspan="2"></td><td></td><td></td><td></td><td>the parts that should remain clean.</td></tr>
<tr><td>26</td><td>Baking</td><td>Use Memert oven<br>▪ Bake @90 °C for 1h</td><td>It is important to bake it well. When PDMS is too soft, wrinkles and cracks are formed after polyamide layer deposition</td></tr>
<tr><td rowspan="8"><em>First PI layer</em></td><td>27</td><td>O2 treatment</td><td>Use the ATTO plasma  tool in Polymer lab<br>▪ Program 5<br>▪ Power 75W (36%)<br>▪ Time: 40s</td><td>To activate the surface of PDMS and improve adhesion to polyamide</td></tr>
<tr><td>28</td><td>Coating 1um of polyamide LTC 9305</td><td>Use manual spinner.<br>▪ Recipe:<br>▪ Speed: 7000 rpms<br>▪ Time: 60s</td><td>Polyamide is negative. Always take fresh polymer and leave it in room temperature for minimum 2h before using. Clean the backside thoroughly with acetone.</td></tr>
<tr><td>29</td><td>Soft Bake</td><td>Use the hot plate.<br>Bake @ 100 ºC for 2min</td><td>Always put the carrier wafer bellow the process wafer.</td></tr>
<tr><td>30</td><td>Exposure</td><td>Use Contact Aligner<br>▪ Mask: “Bottom polyimide”<br>▪ Contact: soft contact<br>▪ Exposure dose: 200mJ/cm2<br>(time: 8s )</td><td></td></tr>
<tr><td>31</td><td>Post-exposure bake</td><td>Use the hot plate.<br>Bake @ 100 ºC for 4min</td><td>Always put the carrier wafer bellow the process wafer.</td></tr>
<tr><td>32</td><td>Developing</td><td>Manual development<br>▪ Step 1: developer HTRD2 for 1min 30s<br>▪ Step2: stopper RER for 1min 30s<br>▪ Dry with nitrogen gun<br>▪ Hard bake @ 100 ºC for 1min 30s</td><td>Rinse wafer with IPA afterwards. Dispose developer and stopper, after a few recycling, into a canister for halogen free organic chemicals.</td></tr>
<tr><td>33</td><td>Curing in Koyo</td><td>Use program 17.
<table>
<tr><td>T [ºC ]</td><td>20/</td><td>108/</td><td>150_</td><td>\30</td></tr>
<tr><td>t [min]</td><td>40</td><td>50</td><td>120</td><td>60</td></tr>
</table></td><td>Even if it is partially cured after hard baking, final cure will evaporate all solvent residues and determine final thickness of the layer.<br>Don’t forget to open N2 valves.</td></tr>
<tr><td>34</td><td>Inspection of PI thickness</td><td>Use Dektak</td><td></td></tr>
<tr><td><em>Al deposi</em></td><td>34</td><td>O2 treatment</td><td>Use the ATTO plasma tool in Polymer lab<br>▪ Program 5<br>▪ Time: 25s<br>▪ Power: 62W (30%)</td><td>Low power plasma treatment to activate the surface of PDMS and improve adhesion to metal</td></tr>
</table>

<table>
<tr><td></td><td>35</td><td>LUR test</td><td>Use Trikon Sigma 204.<br>▪ Transport and HSE in manual mode<br>▪ Place the wafer in HSE @ room temperature<br>▪ Close all valves (4)<br>▪ Read the pressure after 10 min<br>▪ LUR < $2.6^{-6}$</td><td>Make sure that HSE is at room temperature (< 30 ºC) before starting. If it doesn’t work the first time, bake wafer longer or leave it in the loaded cassette in vacuum, in Sigma, for some time and try again. Use the carrier for contaminated wafers. Always return transport and HSE in idle.</td></tr>
<tr><td></td><td>36</td><td>Metal sputtering</td><td>Use Trikon Sigma 204.<br>▪ Target: Al(99%)Si(1%) or pure Al<br>▪ Recipe: AlSi1um_Stack_25<br>(4x250nm AlSi + 3 x degassing)<br>▪ Temperature: 25 ºC<br>▪ Power: 1kW<br>▪ Time: total duration ______</td><td></td></tr>
<tr><td>*Sensors patterning*</td><td>37</td><td>Coating 3um of negative photoresist</td><td>Use manual spinner.<br>▪ Recipe: 3.1um EC3027<br>▪ Speed:<br>▪ Time:</td><td></td></tr>
<tr><td></td><td>38</td><td>Soft bake</td><td>Use the hot plate.<br>Bake @ 90 ºC for 1min 30s</td><td>Always put the carrier wafer bellow the process wafer.</td></tr>
<tr><td></td><td>39</td><td>Exposure</td><td>Use Contact Aligner<br>▪ Mask: “Sensors V2”<br>▪ Contact: hard contact<br>▪ Exposure dose: 150 mJ/cm2</td><td>It is important to optimize lithography here since the metal line is very thin (5um)</td></tr>
<tr><td></td><td>40</td><td>Post-exposure bake</td><td>Use the hot plate.<br>Bake @ 90 ºC for 5min</td><td>Always put the carrier wafer bellow the process wafer. Longer bake because of the wet etching afterwards.</td></tr>
<tr><td></td><td>41</td><td>Developing</td><td>Manual development<br>▪ Use MIF322 developer<br>▪ Time: approx. 1min<br>▪ Rinse in DI water 5 min<br>▪ Dry on a single wafer dryer<br>▪ Hard bake @ 90 ºC for 1min 30s</td><td>Dispose developer into a canister for halogen free organic chemicals. Check after the development (and before baking) the structures under the microscope to see if additional development is needed.</td></tr>
<tr><td></td><td>42</td><td>Inspection</td><td>Check under the microscope the patterns on Al after the development</td><td>To check for the photoresist residues use fluorescent microscope in litho-room</td></tr>
<tr><td></td><td>43</td><td>Etching Al</td><td>Use Omega, plasma etcher.<br>▪ Recipe: al2mu_50<br>▪ Gasses: Chlorine, HBr<br>▪ Temperature: 25 ºC<br><table>
<tr><td>etch</td><td>rising edge</td><td>Bulk</td><td>o/e</td><td>o/e</td></tr>
<tr><td>RF [W ]</td><td>50</td><td>35</td><td>35</td><td>35</td></tr>
<tr><td>t [s]</td><td>0:15</td><td>2:00</td><td>2^30%</td><td>2^15%</td></tr>
</table></td><td>Recipe etches 1um of Al with end point detection.</td></tr>
</table>

| | | | | |
|---|---|---|---|---|
| | 44 | Photoresist removal | Use NI555 for ~18h to remove photoresist | Removing PR might be challenging after plasma bombardment |
| | 45 | Inspection | Check the structures under the microscope and measure Al thickness with Dektak | |
| *Backside etch* | 46 | Carefully position process wafer on carrier wafer by using thermal oil as adhesive | | To protect the frontside during DRIE in the following step, and since PDMS is not allowed on the chuck of the Rapier. |
| | 47 | DRIE through the wafer. | Use Rapier<br>▪ Recipe: EKL_Smooth_20C<br>▪ Cycles: 50 cycles at a time, repeat until wafer is fully etched. | Etching profile depends on the temperature and wafer's thermal conductivity, pressure of the system, He back pressure. Always check first etch rate. |
| | 48 | Coating x um of positive photoresist | Manually distribute photoresist on the fragile membrane. | Photoresist is needed to protect the sensors against BHF in the following step. Spin-coating was not used in order to prevent damaging the sensors. |
| | 49 | Oxide removal | Use BHF to remove the remaining oxide<br>▪ Immerse wafers in BHF bath in a Teflon holder<br>▪ Time: 10 min<br>▪ Rinse for 10 min in water bath | Make your own BHF bath |
| | 50 | Photoresist removal | Use Acetone to remove photoresist<br>▪ Immerse wafers in acetone bath<br>▪ Rinse for 10min in water bath | Make your own acetone bath |
| | | | | |
| | | Manual cutting | | |
| | | Wire-bonding | | |